

Measuring system qualification for LHC arc quadrupole magnets

Dissertation zur Erlangung des akademischen Titels
Doktor der technischen Wissenschaften

Durchgeführt am europäischen Kernforschungszentrum
CERN
und am

Institut für Experimentalphysik
Technische Universität Graz

von

Pierre Schnizer

Vorgelegt der Technischen-Naturwissenschaftlichen
Fakultät der Technischen Universität Graz

22. Oktober 2002



Abstract

Currently the LHC Project at CERN has reached the construction phase. The superconducting magnets of this new accelerator work at superfluid helium temperature. The “arc quadrupoles” (360 pieces), which focus the beam have to be measured at a temperature of 1.9 Kelvin with outstanding precision: The measurement aims to reach a reproducibility of $1.5 \cdot 10^{-4}$ for the field integral, 2 ppm for the harmonic content of the main field and 0.15 mm for the position of the axis. A specially developed scanner allows the simultaneous measurement of the field axis and quality. This thesis demonstrates that the system as it stands fulfils the high requirements with respect to the magnetic measurement and the magnetic axis and thus provides the desired unique versatile equipment. The assessment was performed based on experimental results, direct calibration and using a new simulation tool. The main defects treated are mechanical torsion and vibration of moving parts, electrical noise and power supply ripple.

Zusammenfassung

Das LHC (Large Hadron Collider) Projekt am CERN befindet sich in der Konstruktionsphase. Die supraleitenden Magnete des Beschleunigers arbeiten bei der Temperatur von superflüssigen Helium. Die „Arc Quadrupole“ (360 Stück), die den Strahl fokussieren, müssen mit einer außerordentlichen Genauigkeit bei Betriebstemperatur gemessen werden: das Integral des Feldes mit einer Reproduzierbarkeit von $1.5 \cdot 10^{-4}$, die Multipole mit 2 ppm und die Achse mit 0.15 mm . Ein dazu speziell entwickelter Scanner erlaubt die gleichzeitige Messung der Feldqualität und der Achse. In dieser Arbeit wird gezeigt, daß dieses Meßsystem den hohen Qualitätsansprüchen genügt. Die Bewertung erfolgte unter der Verwendung von experimentellen Daten, direkter Kalibrierung und mittels eines neuen Simulationswerkzeuges. Als Fehlerquellen wurden die mechanische Verwindung und die Vibration der bewegenden Teile, elektrisches Rauschen und das Brummen der Stromversorgung untersucht.

Acknowledgements

I would like to thank Dr. Luca Bottura and Dozent Nikolay Smirnov (both at CERN) for suggesting this topic and for guidance and fruitful discussions.

To Professor Theo Neger, Institut für Experimentalphysik, Technische Universität Graz, sincere thanks for his encouragement and advice.

This work would not have been possible without the help of the many members of the MTA group, LHC Division CERN.

Last, but not least, thanks to Professor Heinrich Sormann Institut für Theoretische Physik, Technische Universität Graz, for taking part in the development of the simulation tool and helpful advice.

Contents

1	Introduction	6
1.1	General Overview	6
1.1.1	CERN	7
1.1.2	Accelerator principles	8
1.1.3	The quadrupole's duty	9
1.1.4	The Arc SSS	12
1.2	Magnetic Field Measurement Methods	14
1.2.1	Rotating Coils	14
1.2.2	Stretched wire	15
1.2.3	Nuclear Magnetic Resonance Devices	17
1.2.4	Hall probes	17
1.2.5	Comparison of these methods	17
1.2.6	The measurement method for the Arc SSS	18
1.2.7	Scope of the thesis	18
2	Rotating coils	20
2.1	Magnetic field and flux definitions	20
2.1.1	Multipole expansion of the field	20
2.1.2	Transformation of harmonic coefficients	21
2.2	Formalism for a coil rotating in a two dimensional field	22
2.2.1	Complex Potential	22
2.2.2	Magnetic flux through a surface	22
2.2.3	Magnetic Flux picked up by a rotating coil	24
2.2.4	Voltage induced in a rotating pick up coil	25
2.3	Typical rotating coil layouts	27
2.3.1	Radial Coils	27

2.3.2	Tangential Coils	28
2.3.3	Comparison of the two coil types	28
2.4	Compensated systems	29
2.5	Mechanical Imperfections	32
2.5.1	Transversal displacements in a pure quadrupole field	34
2.5.2	Torsional vibrations	35
2.6	Spurious harmonics generated in compensated systems	37
3	Description of the measurement system	40
3.1	Mechanical setup of the measurement system	41
3.2	Coils used	44
3.3	Electrical setup of the measurement system	48
3.4	Optical setup of the system	49
3.5	The power supply	52
3.6	Measurement procedure	52
3.7	Analysis Procedure	53
3.7.1	From the electronic output to the Flux	53
3.7.2	Calculating the multipoles	54
3.8	Axis Measurement	55
3.8.1	Calculating the rst - values	57
4	Qualification of the field measurement	58
4.1	Truffaldino, the simulation tool	59
4.1.1	Physical Models	59
4.1.2	Implementation	63
4.2	Electrical effects	64
4.2.1	Preamplifier offset	64
4.2.2	Low frequency ripples	65
4.2.3	Medium frequency electrical noise	70
4.2.4	Difference between current ripple and voltage noise	71
4.3	Mechanical effects	73
4.3.1	The shaker test	73
4.3.2	Shaker induced transversal vibrations of the coil	77
4.3.3	Transversal vibrations of the coil	80
4.3.4	Torsional shaft vibrations induced by the shaker	81

4.3.5	Torsional shaft vibrations at measurement conditions	83
4.4	Motor speed vibrations	85
5	Qualification of the axis measurement	89
5.1	Discussion of the accuracy target	89
5.2	System Parts	90
5.2.1	Axis Searching Coil	92
5.2.2	Glass Window Influences	92
5.2.3	Telescope calibration	95
5.2.4	Checking the straightness of the telescope axis	97
5.2.5	Reference quadrupoles	99
5.3	Total System Random Error	100
5.4	Necessary Environmental Constraints for the measurement area . . .	101
5.5	Comparison to a stretched wire measurement	102
6	Conclusions	106
6.1	Measurement Requirements	106
6.2	Assessment procedure	107
6.2.1	Field quality measurement	107
6.2.2	Axis measurement	107
A	Derivation of formulas	115
A.1	Effect of mechanical coil imperfections on the measurement	115
A.1.1	Lateral displacements in a quadrupole field.	116
A.1.2	Lateral Displacements in a pure n-pole field	117
A.1.3	Torsional vibrations	117
A.1.4	Summary	119
B	Truffaldino - A tool for simulating rotating coil systems	120
B.1	Motivation - Targets	120
B.2	Implementation details	121
B.2.1	Computational aspects	123
B.3	The user's interface	124
B.3.1	The total code of the example	131
B.4	A glimpse under the hood	135
B.4.1	The sector and coil classes	136

B.5	Calculating the sensitivity	137
B.6	Calculating the differential	137
C	Axis calculation procedures	139
C.1	A procedure to calculate the <i>rst</i> values.	139
D	Symbols and Abbreviations	142
D.1	Used Symbols	142
D.2	Abbreviations	143

Chapter 1

Introduction

1.1 General Overview

Nuclear and particle physics have at least two goals [1]: (1) studying the ultimate constituents of matter and their modes of interaction, and (2) understanding the universe's origin and its early evolution. The research is carried out by breaking into parts what-are-known-to-be non-elementary particles (such as electrons, protons, or possibly muons) at energy levels which only existed right after the big-bang.

The tools required for such physics are: (1) sources, from which the particles of interest are extracted and captured, (2) accelerators, which guide the particles in preparation for their smashing, and (3) detectors, which surround the interaction points and which are designed to observe and identify the interaction products [2].

Deeper insight needs higher energies which allows to study smaller structures and generates heavier particles. These particles then are an interesting subject of research as theories predict their properties (e.g. mass, charge, life time). The measurement of these parameters tests the theory and allows the comparison of different theories. The model adopted nowadays to describe the particles is called the standard model predicting many properties of most particles very precisely. Different physical theories were unified in the past, e.g. the weak force and the electromagnetic force with the discovery of the W^+ , W^- , Z^0 particles. Some theories [3] predict the existence of interconnecting particles at higher energy. Only very powerful accelerators allow to reach these desired energies. Testing theories like the "Supersymmetry" demand proton beam energies in the TeV range.

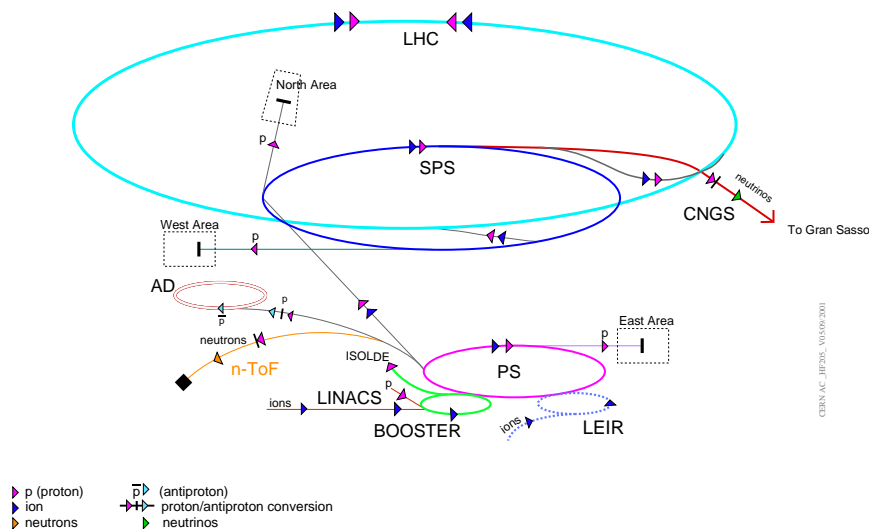


Figure 1.1: The accelerator chain of CERN. Currently the LHC is under construction. Previous accelerators of CERN serve as injector to the LHC machine (SPS and PS). Further experiment area for non LHC physics is shown, like the neutrino beam to Gran Sasso (CNGS), the Antiproton Deaccelerator (AD), the first stage on the way to antihydrogen.

1.1.1 CERN

Located at Geneva in Switzerland, the European Organisation for Nuclear Research was founded in 1953 following a recommendation of the UNESCO Meeting in Florence 1950. The motivation for this project was the in depth view into matter. Starting from the early stage of the Proton Synchrotron (PS) Complex, subsequent projects enhanced the scientific complex with more machines. In Figure 1.1 these accelerators are sketched. The SPS (Super Proton Synchrotron) machine provided the energy to discover the weak force particles W^+ , W^- , Z^0 earning Carlo Rubbia and Simon Van de Meer the Nobel prize 1984 [4, 5] for their discovery. On the way to higher energies LEP (Large Electron Positron collider) was built, providing high precision values for the aforementioned particles already during start up. On the quest for higher energy currently the LHC (Large Hadron Collider) is constructed. Using two proton beams, it will provide a top energy of 2.7 TeV (Tera electron Volts) to the high energy physics community guided by so called “twin aperture magnets”; a novel design where both beams are guided by two magnets assembled in one cold mass. This machine is currently in the construction phase and to be commissioned in 2006 with the first physics runs foreseen in 2007.

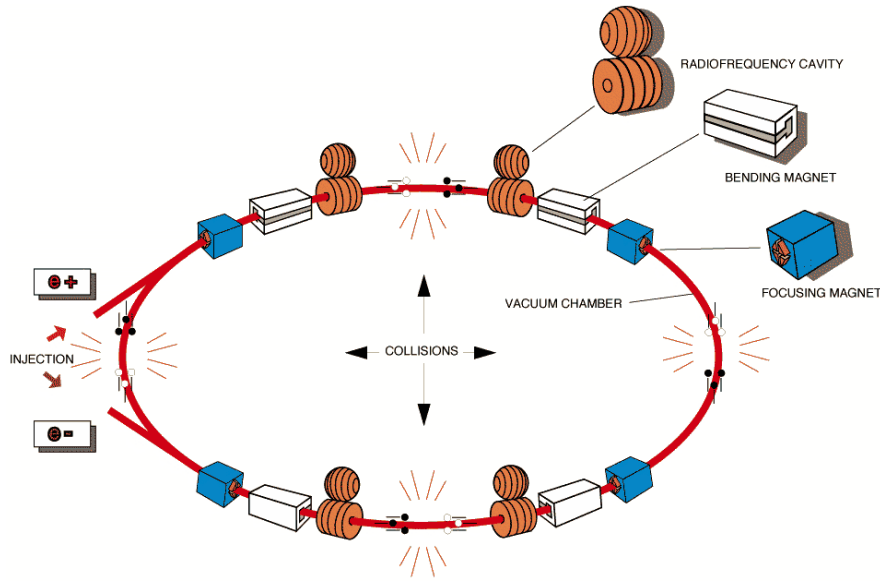


Figure 1.2: The basic components of a collider. The bending magnets bend the particles to the orbit, the focusing elements focus particle heading off the orbit back on the orbit, and the radiofrequency cavities accelerate the beam.

1.1.2 Accelerator principles

The accelerators used at CERN are mainly circular machines. Forces have to be provided to accelerate the particles, and other forces to keep them on their circular path (see Figure 1.2). In modern particle accelerators only charged particles or ions are used. Electrical fields are used to accelerate the particle using the force \vec{F}_C exerted by an electrical field, \vec{E} on a charged particle q , given by Coulomb's law:

$$\vec{F}_C = q\vec{E}. \quad (1.1)$$

This field is provided by radio frequency stations (RF).

To guide the particles magnetic elements are used. A particle with velocity \vec{v} moving in a magnetic field \vec{B} is subjected to the Lorentz Force \vec{F}_L

$$\vec{F}_L = q\vec{v} \times \vec{B}. \quad (1.2)$$

Dipols or fields, homogeneous in space, are used to bend the particles. These particles, however, are also deviated from the ideal orbit due to distorting forces and different start velocities. Therefore they have to be reinforced to the ideal orbit. The quadrupoles are the main element for this task.

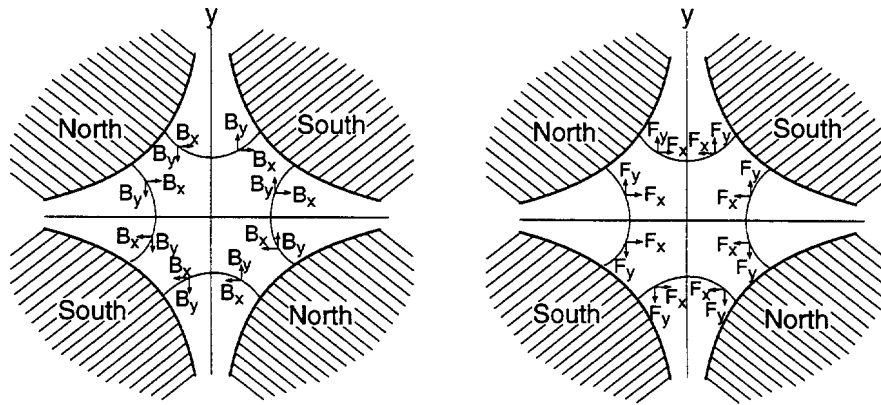


Figure 1.3: The quadrupole's field. A quadrupole has 4 pole shoes. On the left the field is shown. It is zero in the centre and raises linearly with the radius. B_x and B_y show the direction of the respective field components. A positive charge approaching the reader is bent by the Lorentz force F_x and F_y as indicated on the right. This quadrupole focuses the beam in the horizontal plane and defocuses the beam in the vertical plane.

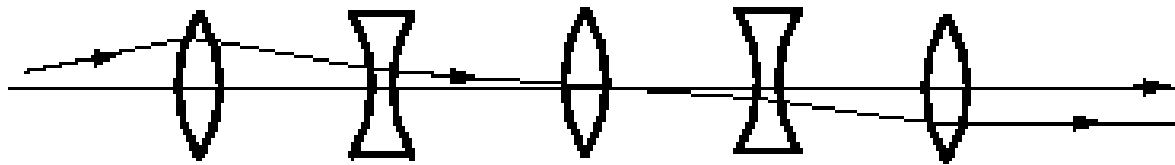


Figure 1.4: Particle trajectory through quadrupoles. Quadrupoles provide a focusing effect in one plane, a defocusing effect, however, in the other plane. Using quadrupoles with alternating gradients a total focusing effect in both planes is achieved. In the above graphic this is illustrated for one plane using the equivalent optical lenses.

1.1.3 The quadrupole's duty

To guide off path particles back to the ideal orbit, fields are needed, which give the particles a kick back depending on their offset from the orbit. To focus the particles back on the track strong focusing using quadrupoles is applied at all accelerators at CERN as it allows stronger gradients and thus better focusing [6]. The quadrupoles, however, only focus in one plane, and defocus in the other (see Figure 1.3). Similarly as in light optics a combination of focusing and defocusing elements yields a net focusing element (See Figure 1.4 and 1.5). Due to the position dependence of the field the quadrupole focusing – defocusing depends on the magnet's offset from the beam. A misaligned quadrupole introduces a faked dipole (See Figure 1.6). Therefore these magnets have to be aligned to the beam orbit. In Figure 1.7 the effect of a misaligned quadrupole is shown. During each turn the particle is kicked off from the ideal orbit.

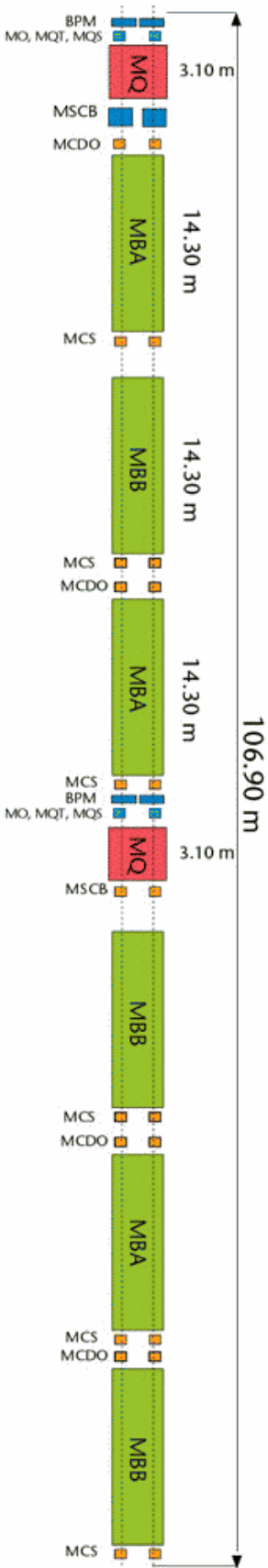


Figure 1.5: Layout of the LHC Cell. The magnets of the LHC accelerator are assembled in periodic cells along the ring. Each cell starts with a quadrupole (labelled MQ) followed by three dipoles (labelled MBA or MBB). Then a second quadrupole with an alternate gradient is followed again by three dipoles. Beside the main magnets a lot of correctors are needed (MO, an octupole, MQT, MQS correcting quadrupoles MSCB, a combined dipole sextupole corrector, MCS a sextupole corrector and MCDO a combined decapole octupole corrector; BPM are beam position monitors).

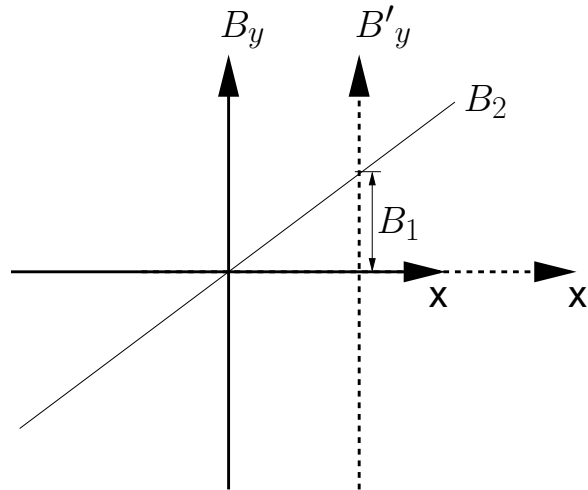


Figure 1.6: Dipole introduced by a shifted quadrupole. The quadrupole's field B_2 rises linearly from the centre (shown in the coordinate system x, B_y). Shifting the quadrupole's centre the field has an offset in the new coordinate system (shown in the coordinate system x', B'_y). The offset on the B'_y -axis corresponds to a fake dipole marked as B_1 .

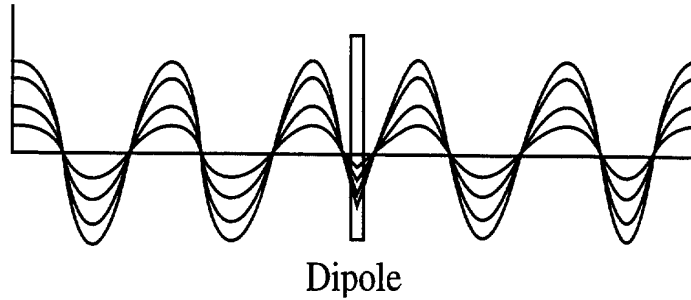


Figure 1.7: Closed orbit distortion induced by a misaligned quadrupole. Shifting a quadrupole yields a dipole and a quadrupole in the original system. During each revolution the beam is kicked into one direction. During several revolutions it moves outside the allowed area.

For the LHC the maximum tolerable error was calculated to: $\Delta x, \Delta y < 0.37mm$ [7, 8]. The strength of the main field of the magnet corresponds to the focal strength of a conventional lens. An error of the lens strength results in a defocusing. Higher order multipoles cause similar effects as lens errors of a conventional optical lens. Therefore the following table was set as a target for the magnetic measurement of the quadrupole as a combination of beam based requirements and technically achievable precision [9]:

Table 1.1: Requirements to the measurement system. The axis centre and the field angle measurements accuracy have to be reached. The harmonic strength is feasible. The field strength is a goal. Releasing this request by a factor of 5 will still allow the operation of the machine.

Property	Requirement	unit
Field Strength	$1.5 \cdot 10^{-4}$	1
Field Angle	0.5	<i>mrاد</i>
Axis Centre	0.1	<i>mm</i>
Harmonics Strength	0.02	<i>units</i>

One will notice that the axis centre is specified to 0.1 *mm* and significantly differs from the 0.37 *mm* above. In the 0.37 *mm* requirement the measurement and installation precision has to be taken into account. (The magnets have to be measured and aligned according to the measurement.) So the total part of an acceptable error limit of 0.37 *mm* was split into the aforementioned requested measurement precision and the installation precision.

1.1.4 The Arc SSS

The quadrupole is called MQ in LHC terms. This quadrupole is mounted inside a cryostat together with smaller corrector magnets (see also Figure 1.8) called Short Straight Section (SSS). Further, the beam position monitor which allows the measurement of the beam with respect to the quadrupole is installed here. All the main magnets of the LHC are based on superconducting NbTi cables and are operated at a temperature of 1.9 Kelvin. The front of the MQ is shown in Figure 1.9. The beam pipe is the innermost pipe. The cables are clearly visible, clamped by the stainless steel collars. The yoke, which reacts a part of the forces acting on the cables due to the magnetic field, can be seen at the rear. In Figure 1.10 a cross section through the SSS is shown. The cryostat forms the outermost enclosing, in which all the cables as well as the cooling pipes are stored. More than one cryogenic layer is found. The first thermal barrier is formed by a vacuum vessel followed by two super insulation layers. The first layer is kept at an intermediate temperature, around 50 Kelvin, to cut radiation loss from the 300 Kelvin cryostat to the 1.9 Kelvin cold mass. The second layer shields the components operated at liquid helium temperature.

The corrector magnets mounted in the SSS can be of different type. In Figure 1.8 an octupole and a combined sextupole dipole corrector are shown. Instead of the

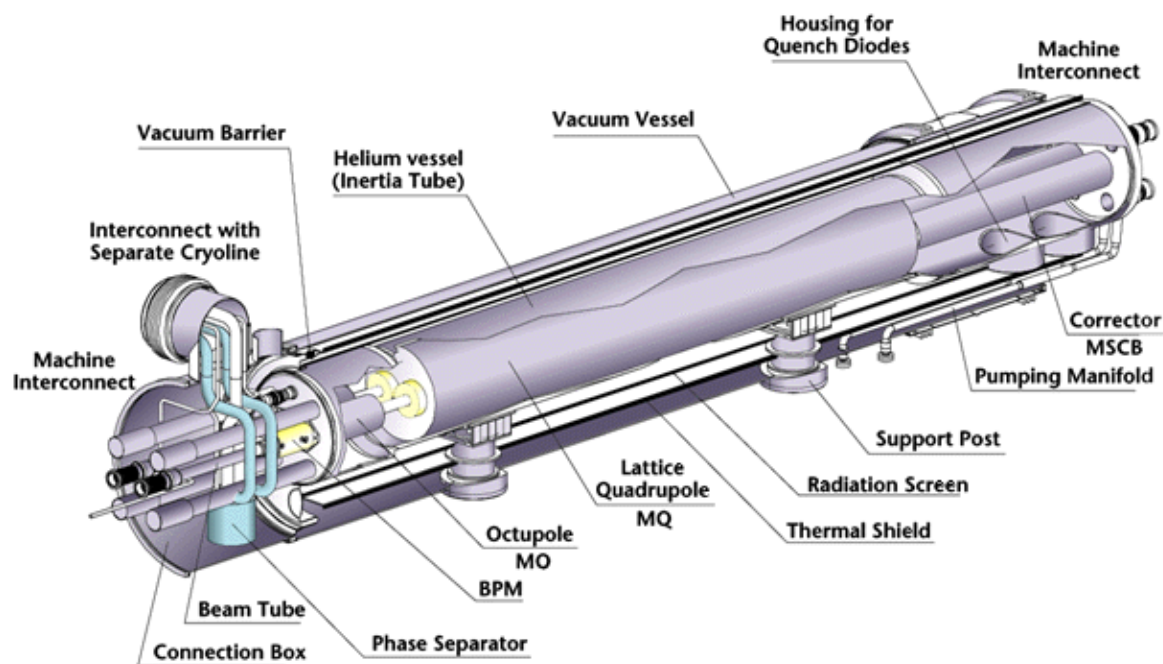


Figure 1.8: Components of the Short Straight Section. BPM is the beam position monitor.

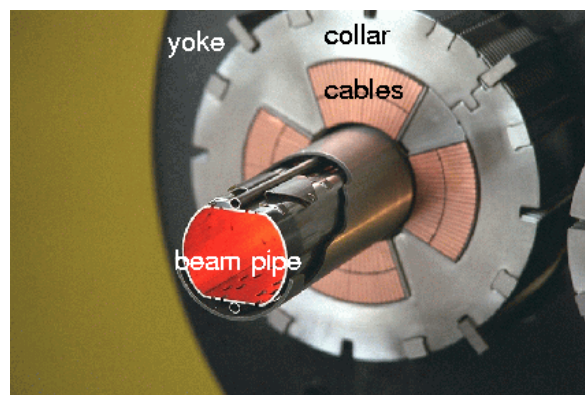


Figure 1.9: View of the Main Quadrupole with installed beam pipe. The four coils of the quadrupole are nicely visible. Each coil is made up by wound cables. The coils are enclosed by a stainless steel collar. The yoke encloses the collar in a well defined geometric position and provides a return path for the magnetic flux, thus shielding the exterior of the magnet.

octupole, however, different quadrupole correctors can be mounted [10]. Further special equipment needed for the operation of the LHC machine is stored inside the SSS like the vacuum separation system and cryogenic supply feed lines.

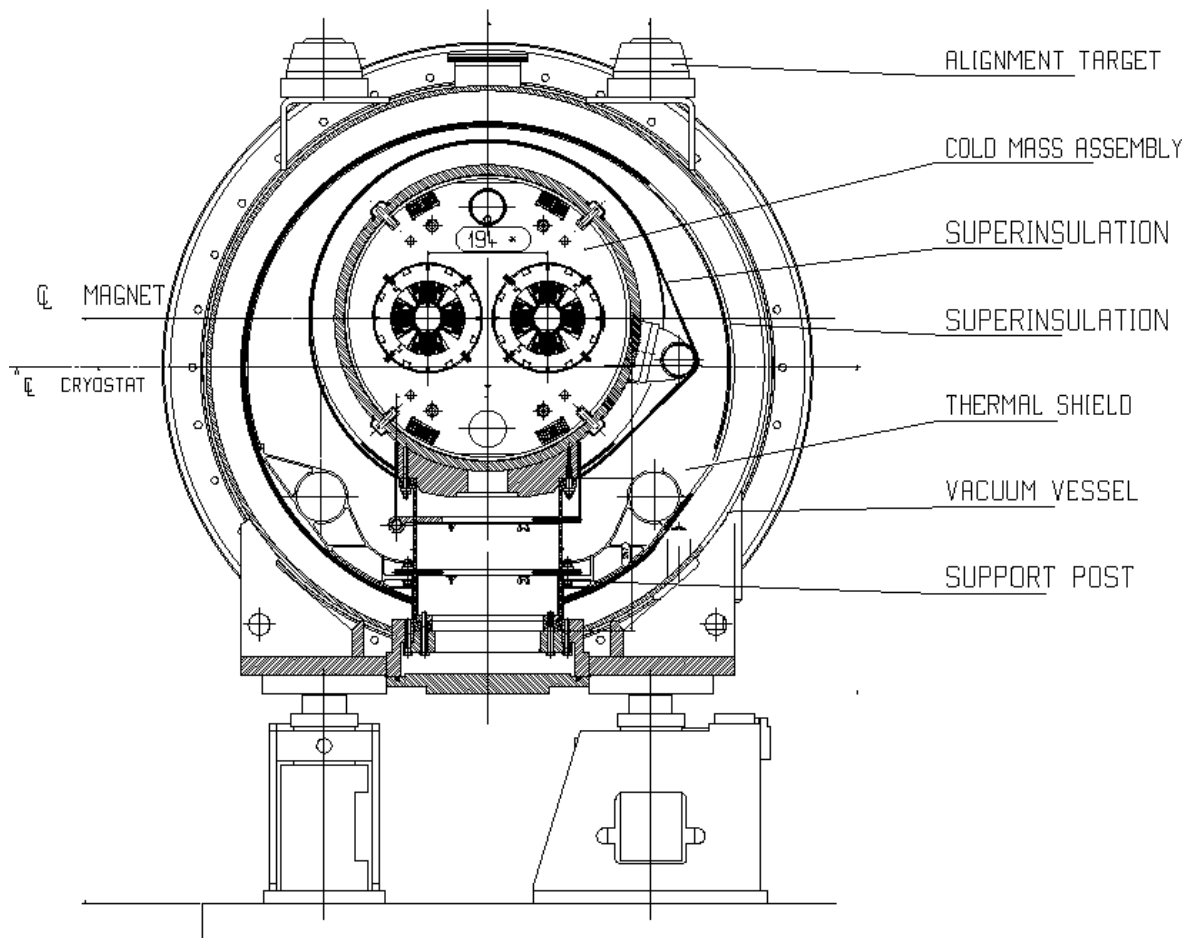


Figure 1.10: Cross section of the SSS. In the middle the quadrupoles are visible inside the collars. The collars are kept by an iron yoke. All these parts are inside the cold mass. The quadrupoles for the two beams are nicely visible.

1.2 Magnetic Field Measurement Methods

The magnetic measurement methods used for HEP particle accelerators are based either on the induction method, the Hall effect or the nuclear magnetic resonance.

1.2.1 Rotating Coils

A wire loop rotating around an axis forms a rotating coil. In Figure 1.11 a sketch of such a coil is given. The wire loop integrates the field over its area. Due to advances in electronics this method may obtain an accuracy of better than 10^{-4} . Using an array of coils the sensitivity can be further increased. These coils have a length of typically 0.5 m . Their tallest radius is typically in the order of a few millimetres and preferably allows to cover the area of interest during the rotation. As they turn

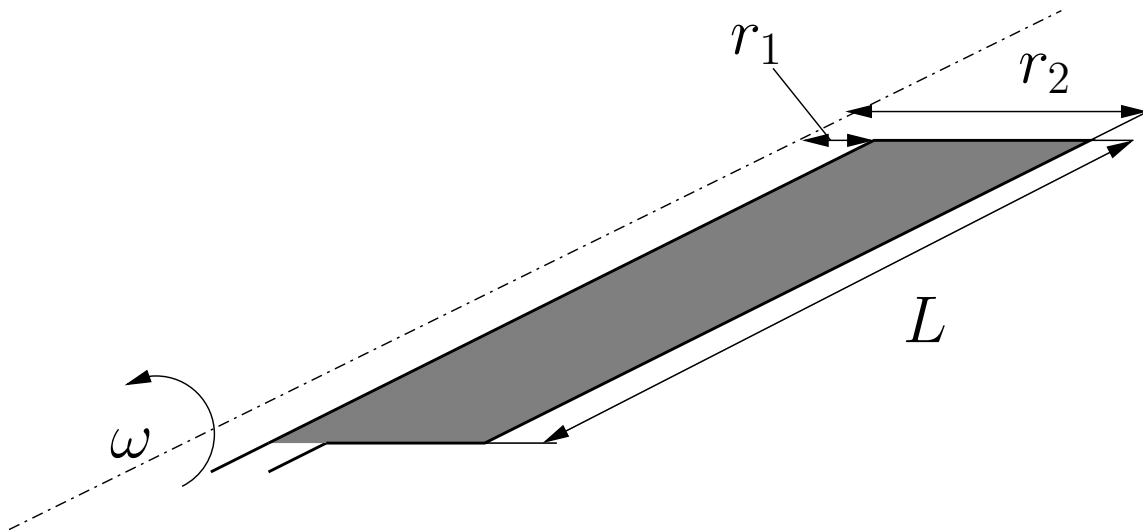


Figure 1.11: Sketch of a rotating coil. Rotating coils measure the magnetic field based on the induction law. When a coil is rotated a voltage is induced into the wire loop, which is proportional to the field passing the coils surface (indicated by the gray rectangle). Beside the field the induced voltage depends on the rotation speed ω the length L , the outer radius r_2 and the inner radius r_1 .

inside high magnetic fields the wire support must be made of a non conducting, non magnetic material. Because magnets nowadays have a length of a few meters, the coil is either successively placed along the magnet and the field is measured at each step or a set of coils is put longitudinally together and turned together (such a device is described in [11]). Both methods yield the integral of the field over each measured length. Compared to the following methods the rotating coil allows a fast measurement of the integral of the field, the higher order multipoles and the direction of the field. Moreover the data is split in a few integrals which allows to separately measure the field in the magnet ends and the deviation of the field along the magnetic axis.

During the HERA measurement campaign at DESY this method was used to measure the higher order multipoles of the field in cold condition [12]. For the SSC (Super Conducting Super Collider) measurement a “mole” was foreseen, containing a rotating coil to measure the field quality [13].

1.2.2 Stretched wire

The stretched wire technique is also based on the induction method. Here a wire is stretched through the aperture of the magnet [14, 15] (see also Figure 1.12). A

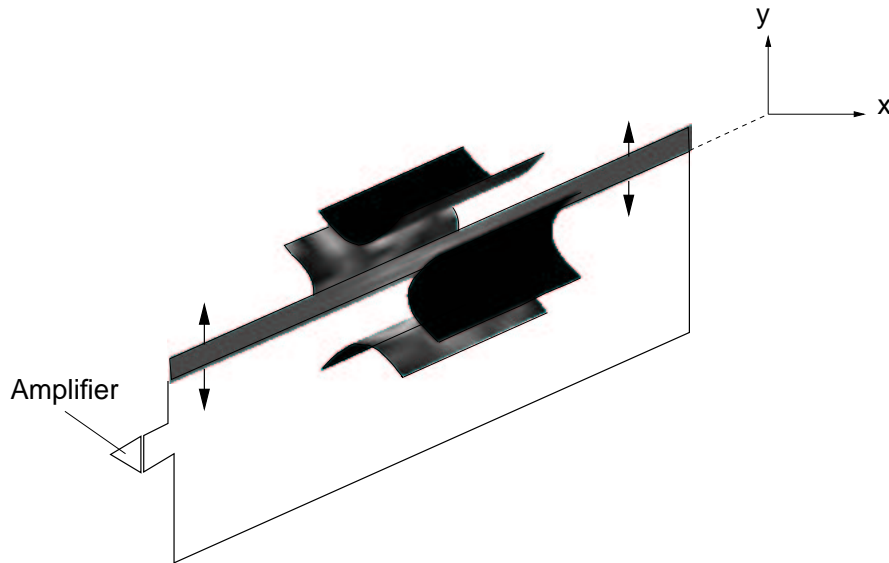


Figure 1.12: Sketch of the stretched wire method. A wire is stretched through a magnet. The wire is connected to an amplifier at one end and to a return wire on the second end. This wire closes the input loop to the amplifier. When the wire is moved (indicated by the arrows) a voltage is induced. This voltage is used to measure the field.

second wire, usually placed outside of the magnet, closes the loop and the two ends are connected to an amplifier. When the wire inside the magnet is moved a voltage is induced in the loop. This voltage is measured. With the knowledge of the movement the axis and the integral field strength of the magnet are calculated. The wire must be very thin (in the order of 0.1 mm) which renders its handling difficult. Further on the wire must be free of dirt, as dirt often has magnetic properties, and thus the magnetic field acting on the dirt will deviate the wire from its ideal position generating a fake result [16]. With this device a measurement precision of the axis of $20\text{ }\mu\text{m}$ for a 15 m long magnet is possible in the coordinate frame of the stretched wire (The transfer of this frame to the magnet fiducials will most likely add a bigger error.). The angle can be measured with a precision of 0.1 mrad and the field integral with a precision of $2 \cdot 10^{-4}$ [17].

For the Arc SSS measurement the stretched wire is used as a cross reference device. During the HERA measurement campaign the magnetic axis of the quadrupoles was measured using this method [12]. For the UNK magnets (a superconducting collider which was to be built in Protvino, Russia) it was foreseen to measure the axis and the field strength of the quadrupoles using stretched wires [18].

1.2.3 Nuclear Magnetic Resonance Devices

This method was first used to measure the nuclear magnetic momentum in molecular beams [19, 20]. A few years later the phenomenon was observed in solids by two independent teams [21, 22, 23].

This method, in practice, measures the nuclear resonance of hydrogen in a sample of water. It allows to measure the absolute value of the field with a precision of better than 1 *ppm* and is nowadays accepted as a primary reference. It is, however, not suitable for inhomogeneous fields. During the HERA measurement campaign a combination of hall probes and a nuclear magnetic resonance devices was used to measure the field integral of the dipoles. Such a device is also often used to measure the field quality of spectrometer magnets.

1.2.4 Hall probes

Hall probes use the Hall effect [24] to measure magnetic fields. When a current is flowing in a solid penetrated by a magnetic field this field generates a voltage perpendicular to the current and the field itself. Only for semiconductors this voltage is large enough to be practical. The probes used today have a dimension of 0.1 *mm* and allow a measurement of the field up to a precision of 10^{-3} - 10^{-4} . As they directly measure the field they can rest in a fixed position. Due to their size they measure the field locally and permit the measurement in inhomogeneous fields. However the generated voltage also depends on the temperature of the probe, therefore it's temperature must be precisely controlled to achieve an acceptable precision.

1.2.5 Comparison of these methods

The rotating coil method allows to measure all properties of the magnetic field integrated over the coil length. The stretched wire method allows to measure the angle and the strength of the field. This method typically needs a second method to measure the field multipoles. Hall plates measure the field on the spot. Their disadvantage is the temperature dependence of the probe and the fact that the field integral measurement needs many steps due to the small size of the probe. Nuclear magnetic resonance devices measure the absolute value of the field in homogeneous fields and thus do not apply to quadrupoles.

1.2.6 The measurement method for the Arc SSS

Due to the great number of Arc SSS (360) [10, 25] an efficient measurement system is essential to perform the measurement in a environment with strong time constraints. The rotating coil method was chosen from the standard magnetic measurement methods discussed above as it provides the following advantages:

- measurement of all field parameters: field strength, field direction, field harmonics and field axis.
- integration over the coil length: the rotating coil senses the integral of the magnetic flux it passes. As the size of the coil can be chosen the data is split in a few integrals which allows to separately measure the field in the magnet ends and the deviation of the field along the magnetic axis.

Therefore the decision was taken to base the total Arc SSS measurement on the rotating coil method. The system setup is discussed in detail in Chapter 3.

1.2.7 Scope of the thesis

This thesis qualifies a novel measurement system which is able to measure

1. the integrated strength of the main field,
2. the angle,
3. the axis,
4. and the harmonics of the field.

It is the most flexible and universal system foreseen for the measurement of the Arc SSS's. In this thesis it will be shown, that this systems fulfils the requirements given in Table 1.1. The topic is split in two parts:

- *the field quality measurement*: focusing on the measurement of the field strength, and the direction. In here the electrical and mechanical equipment necessary for the measurement is discussed. All parameters are measured by a rotating coil probe. A computer program was developed allowing to simulate the whole measurement system. Using an oscilloscope the influence of the magnet flux ripple was studied and the effect on the measurement was shown using

the aforementioned tool. The performance of the mechanical equipment was studied by shaking the coil in a well defined manner. Measuring the movement of the coil the simulation could calculate the spurious harmonics induced by this movement. Using adapted compensation schemes the spurious harmonics were measured and found to be consistent with the calculation. With this confidence the spurious harmonics generated by lateral vibrations of the coil were measured. Following the same philosophy the torsional vibrations of the mechanical connections between coil and motor were estimated.

- *the axis measurement:* The axis measurement is based on rotating coils as well. As this measurement needs quite a few types of optical equipment this measurement is treated separately from the other field parameters. The quality of all components is discussed. To assess the measurement quality of the telescope tracker, which establishes the reference line inside the magnet bore, a calibration bench was set up, as this part forms the most critical part in the axis measurement chain. Comparing the axis measurement of the main system to a single stretched wire measurement, the total quality of the system was shown.

The whole system was found to provide the necessary quality according to the request (see also Table 1.1).

Chapter 2

Rotating coils

The magnetic field of modern accelerator magnets, whose length is hundreds of times larger than their diameter, is simplified to a two dimensional approximation for beam calculations. Their measurement must therefore provide the field strength, field direction and field quality along the axis. For this purpose the rotating coil method is suitable as the coil measures the integral of the field over its length with high accuracy. In this chapter the formulae describing the magnetic field and the voltage induced into the measuring coils will be derived. The effect of mechanical imperfections of the coil rotation on the field measurement will be detailed. All expressions given here follow [26] and [27].

2.1 Magnetic field and flux definitions

2.1.1 Multipole expansion of the field

The magnetic field for accelerator magnets is described by the field multipole expansion in a complex plane normal to the magnet axis using the multipole expansion [28] of the complex variable $\mathbf{z} = x + iy$ (complex variables are denoted here and below in boldface)

$$\mathbf{B}(\mathbf{z}) = B_y + iB_x = \sum_{n=1}^{\infty} [B_n + iA_n] \left(\frac{\mathbf{z}}{R_{Ref}} \right)^{(n-1)}, \quad (2.1)$$

where $B_n + iA_n = C_n$ are the complex multipole coefficients called harmonics. The B_n are the “normal” coefficients and A_n the “skew” ones. They express the field strength of the n^{th} multipole at the reference radius R_{Ref} . As the European conven-

tion is used here, C_1 is the dipole strength. Uppercase notation defines the coefficients in non normalised terms, i.e. they are given in units of Tesla at the reference radius. Lowercase coefficients describe relative harmonics. They are normalised by the strength of the main field and are calculated using

$$c_n = 10^4 \frac{C_n}{C_m} = b_n + ia_n, \quad (2.2)$$

with C_m the strength of the main multipole. The factor of 10^4 is used because the higher order harmonics are usually 10^{-4} smaller than the main harmonic in accelerator magnets. Thus practical numbers for these coefficients are obtained. The dimension of the c_n 's is called *unit*.

2.1.2 Transformation of harmonic coefficients

In the following the formulae for the two basic transformations - translation of the reference frame by a vector $\mathbf{D}_z = D_x + iD_y$, and rotation of the frame around its centre by an angle α - of the coordinate system are outlined (see also Figure 2.1). They are derived by coordinate transformation of Equation (2.1).

Translation

A translation of the reference frame by \mathbf{D}_z transforms the harmonic coefficients C_k (in the original frame) into the new C'_n as described by

$$C'_n = \sum_{k=n}^{\infty} \binom{k-1}{k-n} C_k \left(\frac{\mathbf{D}_z}{R_{Ref}} \right)^{k-n}. \quad (2.3)$$

Rotation

A rotation of the reference frame around the angle α transforms the original multipoles C_n into the new multipoles C'_n as given by

$$C'_n = C_n e^{in\alpha}. \quad (2.4)$$

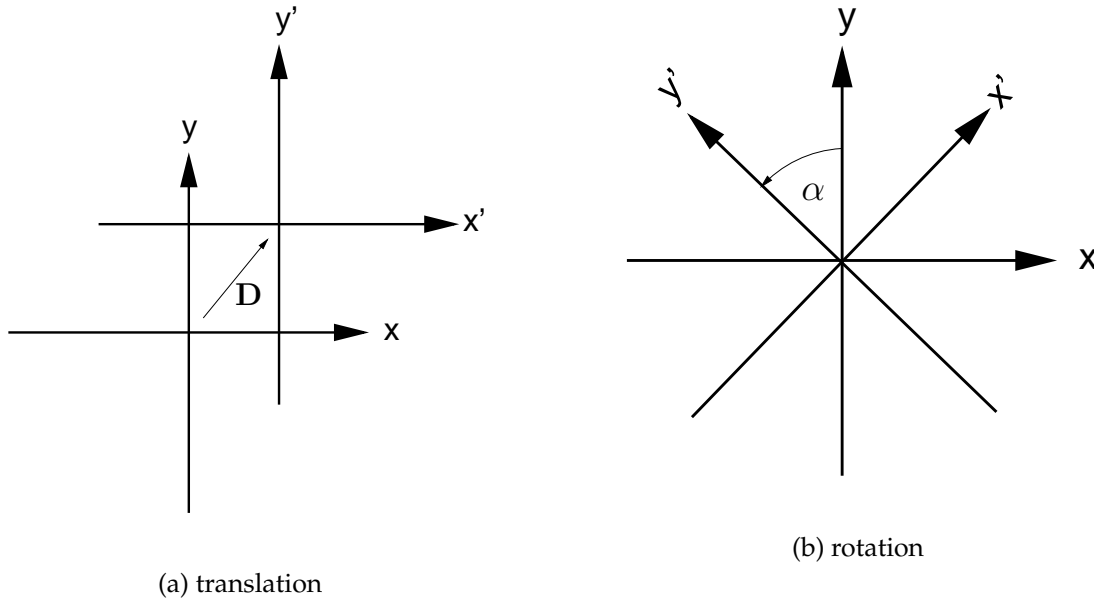


Figure 2.1: Simple Transformations of the reference frame. On the left a complex vector D describes the translation of the coordinate system x, y to the coordinate system x', y' . On the right a angle α describes the rotation of the coordinate system x, y around its origin to the coordinate system x', y' .

2.2 Formalism for a coil rotating in a two dimensional field

2.2.1 Complex Potential

Regular analytic functions of complex variable are integrable and their primitives are themselves regular and analytic. A complex potential $F(z)$ can be defined by

$$B(z) = -\frac{dF(z)}{dz} . \quad (2.5)$$

Apart from the sign the complex function F is a primitive of B . Hence it is regular and analytic. It can be expanded into a power series

$$F(z) = -\sum_{n=1}^{\infty} \frac{1}{n} C_n \frac{z^n}{R_{Ref}^{n-1}} + const. \quad (2.6)$$

2.2.2 Magnetic flux through a surface

Now a cylindric surface Σ parallel to the axis of the magnet z_m and uniform in the axial direction is considered. Γ designates the arc at the intersection between Σ and

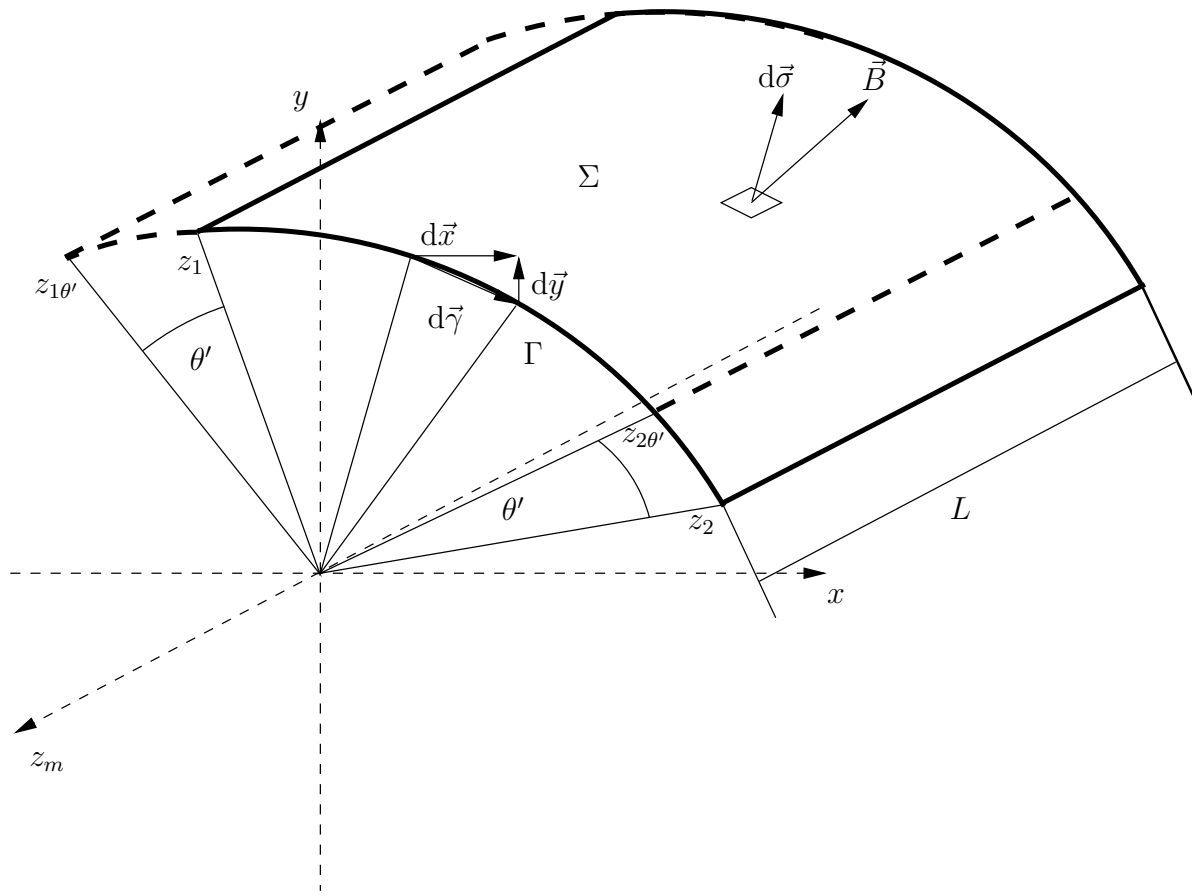


Figure 2.2: Magnetic flux through a cylindrical surface. A cylindrical surface parallel to the axis z_m indicated by the solid line is turned by an angle θ' to reassemble the dashed surface. L is the length of the surface, z_2, z_1 the original positions of the ends and $z_{2\theta'}, z_{1\theta'}$ these positions after the surface has been rotated. Γ represents the intersection arc of the surface Σ and the xy plane. $d\vec{\sigma}$ represents the surface element vector and \vec{B} the direction of the magnetic field.

the xy plane. z_1 and z_2 determine the positions of the ends in the complex plane (See Figure 2.2).

The magnetic flux Φ through this surface is described by

$$\Phi = \iint_{\Sigma} \vec{B} d\vec{\sigma}, \quad (2.7)$$

with $d\vec{\sigma}$ the surface element vector.

Since the surface is parallel to the axis of the magnet, and since \vec{B} and Σ are uniform along the magnet's axis, we can write

$$\Phi = L \int_{\Gamma} \vec{B}(\vec{z}_m \times d\vec{\gamma}), \quad (2.8)$$

with L the length of the surface along the z_m -axis and $d\vec{\gamma}$ the arc element vector. Now the coordinates of $d\vec{\gamma}$ are set to $(dx, dy, 0)$. The coordinates of $(\vec{z}_m \times d\vec{\gamma})$ are $(-dy, dx, 0)$. Using the two dimensional expression of (2.1) the flux is given by

$$\Phi = L \int_{\Gamma} (B_y dx - B_x dy). \quad (2.9)$$

The above equation can be transformed to

$$\Phi = L Re \left[\int_{\Gamma} (B_y + i B_x) (dx + i dy) \right]. \quad (2.10)$$

In complex notation it is expressed by

$$\Phi = L Re \left[\int_{z_1}^{z_2} \mathbf{B}(\mathbf{z}) d\mathbf{z} \right]. \quad (2.11)$$

Introducing the definition of the complex potential of (2.5) the flux is described as

$$\Phi = -L Re [\mathbf{F}(\mathbf{z}_2) - \mathbf{F}(\mathbf{z}_1)]. \quad (2.12)$$

The magnetic flux through the surface Σ is directly proportional to the real part of the difference between the complex potential values at the two ends of the arc Γ . As expected from Cauchy's theorem on the integral of analytical functions in complex variables the result of the integral does not depend on the path chosen between \mathbf{z}_1 and \mathbf{z}_2 . In the above equation \mathbf{F} is replaced by its power expansion

$$\Phi = L Re \left[\sum_{n=1}^{\infty} \frac{1}{n} \mathbf{C}_n \frac{\mathbf{z}_2^n - \mathbf{z}_1^n}{R_{Ref}^{n-1}} \right]. \quad (2.13)$$

2.2.3 Magnetic Flux picked up by a rotating coil

Now it is assumed that the surface Σ represents the surface for all turns of a pick up coil rotating around the axis z_m (i.e. the windings are infinitely thin). The angle θ' describes a rotation of the surface Σ around the axis z_m . \mathbf{z}_2 and \mathbf{z}_1 are the positions of the extremities of the arc Γ at $\theta' = 0$. So for any angle θ' the location of the ends $\mathbf{z}_{1\theta'}$ and $\mathbf{z}_{2\theta'}$ is described by

$$\mathbf{z}_{1\theta'} = \mathbf{z}_1 \exp(i\theta') \quad \text{and} \quad \mathbf{z}_{2\theta'} = \mathbf{z}_2 \exp(i\theta'). \quad (2.14)$$

Using Equation (2.13) and (2.14) the flux Φ seen by a rotating coil is

$$\Phi(\theta') = Re \left\{ \sum_{n=1}^{\infty} K_n C_n \exp(in\theta') \right\}, \quad (2.15)$$

with K_n the coil's sensitivity to the n^{th} multipole

$$K_n = \left(\frac{N_w L R_{Ref}}{n} \right) \left[\left(\frac{\mathbf{z}_2}{R_{Ref}} \right)^n - \left(\frac{\mathbf{z}_1}{R_{Ref}} \right)^n \right]. \quad (2.16)$$

Equation (2.16) shows that K_n only depends on the coil geometry.

2.2.4 Voltage induced in a rotating pick up coil

The voltage induced by a flux change is given by Faraday's law

$$V = - \frac{d\Phi}{dt}. \quad (2.17)$$

A change of flux inside the coil is achieved either by varying the magnetic field (i.e. varying the magnet current) or by rotating the coil inside the magnetic field. Here the second method, called *rotating coil method*, is described. The angular dependence of the flux on the angular position of the coil is shown in equation (2.15). In the following the magnetic field is considered to be independent from time. Faraday's law gives the voltage versus time. To calculate the multipoles C_n the flux versus angle is needed.

Therefore the measurement is performed in the following way:

- The coil is turned by a motor.
- The voltage induced in the coil is fed to an integrator.
- The integrator is read out by a controller.
- An angular encoder triggers this readout to ensure equidistant readouts. This is needed by the following analysis which is based on a Fourier transform.

In the following this procedure is described mathematically. It is assumed that the N_w turn pick up coil is rotating around the z-axis with some angular velocity. Then the angle θ' at a given time t equals $\theta(t)$ and the angular speed equals its first derivative

$$\theta' = \theta(t) \quad \text{and} \quad \frac{d\theta(t)}{dt} = \dot{\theta}(t). \quad (2.18)$$

In the ideal case

$$\theta' = \omega \cdot t \quad \text{and} \quad \frac{d\theta(t)}{dt} = \omega, \quad (2.19)$$

with ω the ideal (i.e constant) angular velocity.

Faraday's law (2.17) is applied to Equation (2.15),

$$V(t) = -\dot{\theta}(t) \operatorname{Re} \left\{ \sum_{n=1}^{\infty} n \mathbf{K}_n \mathbf{C}_n \exp(\mathrm{i} n \theta(t)) \right\}. \quad (2.20)$$

The voltage is then integrated using an integrator

$$\Phi(t) = - \int_0^t V(t') dt', \quad (2.21)$$

assuming that the integration starts at $t = 0$.

The angular encoder triggers the readout of the integrator to ensure equally spaced angular steps. Since $\theta(t)$ gives the position of the coil versus time, its inverse function $t = \theta^{-1}(\theta')$ describes the time at which an angle was reached. Thus one can write the flux Φ_i given by the integrator for an angular interval $\theta'_i - \theta'_0$ as

$$\Phi_i = - \int_{\theta^{-1}(\theta'_0)}^{\theta^{-1}(\theta'_i)} V(t) dt. \quad (2.22)$$

θ'_0 is the angle at which the integration started and θ'_i

$$\theta'_i = \frac{2\pi}{P} i \quad i = 1 \dots P, \quad (2.23)$$

with P the number of readings per revolution. The flux Φ_i can be further written as

$$\Phi_i = - \int_{t_0}^{t_i} V(t) dt = - \int_{\theta'_0}^{\theta'_i} \frac{1}{\dot{\theta}} V(\theta) d\theta. \quad (2.24)$$

Φ_i corresponds to the value of the integral at t_i . Comparing the last term of the above statement to Equation (2.20) one can see that Φ_i is speed independent. A discrete Fourier transform is applied to the total readout $\Phi = \{\Phi_i \mid i = 1 \dots P\}$ of the integrator

$$\Psi = DFT[\Phi], \quad (2.25)$$

with Ψ the spectrum of the flux and DFT the discrete Fourier transform. After some calculation one can see that the multipoles \mathbf{C}_n are obtained by

$$\mathbf{C}_n = \frac{1}{\mathbf{K}_n} \Psi_n. \quad (2.26)$$

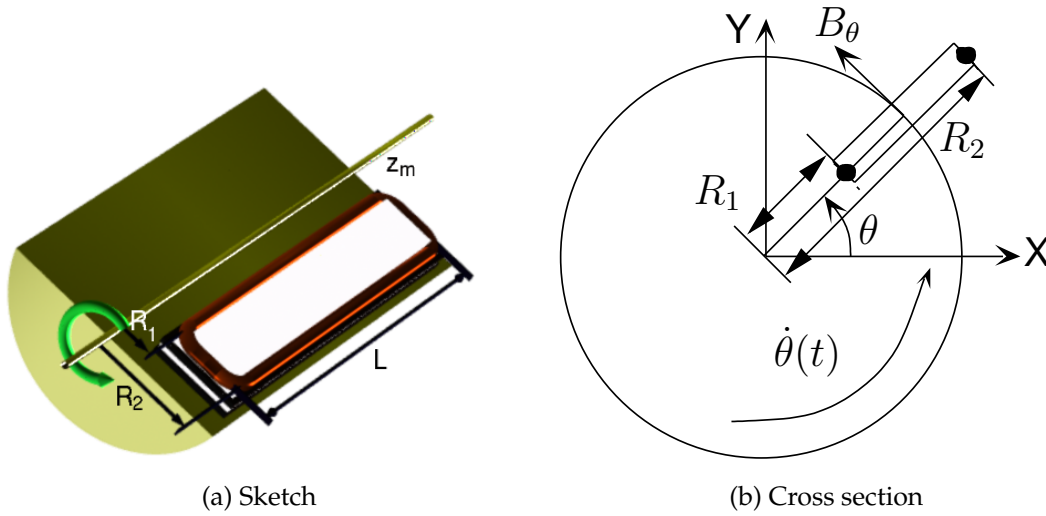


Figure 2.3: A radial coil. On the left a sketch of such a coil and on the right the cross section is shown. B_θ is the tangential component of the field. R_1 and R_2 are the radii of the windings. In the cross section the axis z_m is perpendicular to the paper plane. The position of the centre of the coil with respect to the x - axis is described by the angle θ and the coil's angular velocity with $\dot{\theta}(t)$.

2.3 Typical rotating coil layouts

The Formula (2.16) describes the sensitivity of the coil for an arbitrary location of the coil extremities with respect to the rotation axis. Two typical layouts are the *radial coil* and the *tangential coil*, which will be described in the following.

2.3.1 Radial Coils

In a radial coil all wires are located in one plane, which passes through the axis of rotation and is parallel to the axis of rotation. In its perfect form it is only sensitive to the tangential component of the magnetic field B_θ (see Figure 2.3).

The sensitivity of such a coil is obtained by replacing z_2 with R_2 and z_1 with R_1 in Equation (2.16))

$$\mathbf{K}_n = \frac{N_w L R_{Ref}}{n} \left[\left(\frac{R_2}{R_{Ref}} \right)^n - \left(\frac{R_1}{R_{Ref}} \right)^n \right], \quad (2.27)$$

with R_2 the outer diameter and R_1 the inner diameter of the coils windings.

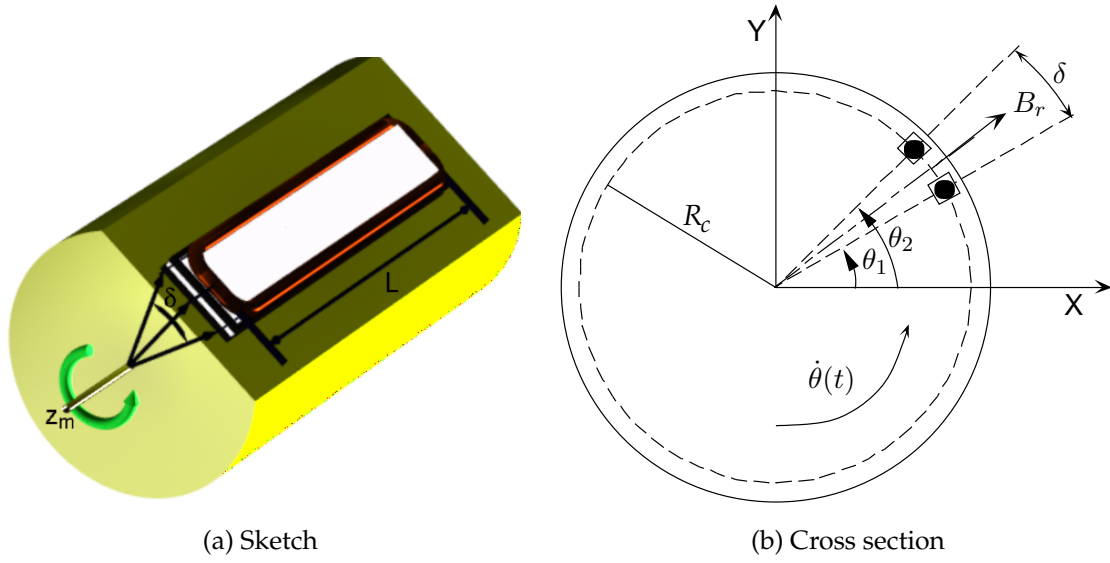


Figure 2.4: A tangential coil. On the left a sketch of such a coil and on the right the cross section is shown. B_r is the radial component of the field, R_c the radius to the centre of the coil and δ the opening angle of the coil. The axis z_m is perpendicular to the paper plane. The position of winding one with respect to the x -axis is described by θ_1 and the position of winding two by θ_2 . $\dot{\theta}(t)$ denotes the coil's angular velocity.

2.3.2 Tangential Coils

In a tangential coil all wires are located on the surface of a cylinder whose axis coincides with the axis of rotation. The sensitivities of a coil as shown in Figure 2.4 is calculated by substituting $\mathbf{z}_1 = R_c e^{i\theta_1}$ and $\mathbf{z}_2 = R_c e^{i\theta_2}$ in Equation (2.16)

$$\mathbf{K}_n = \frac{2N_w L R_{Ref}}{n} \left(\frac{R_c}{R_{Ref}} \right)^n (\exp(in\theta_2) - \exp(in\theta_1)), \quad (2.28)$$

with R_c the radius of the cylinder and $\theta_{1,2}$ the angle of the wire position. Substituting θ_2 with $\delta/2$ and θ_1 with $-\delta/2$, where δ is the opening angle of the coil, one can write the coil's sensitivity as

$$\mathbf{K}_n = -\frac{i2N_w L R_{Ref}}{n} \left(\frac{R_c}{R_{Ref}} \right)^n \sin\left(\frac{n\delta}{2}\right). \quad (2.29)$$

Note that such a coil is only sensitive to the radial component of the field.

2.3.3 Comparison of the two coil types

In Figure 2.5 the sensitivities of the two coil types are compared as a function of

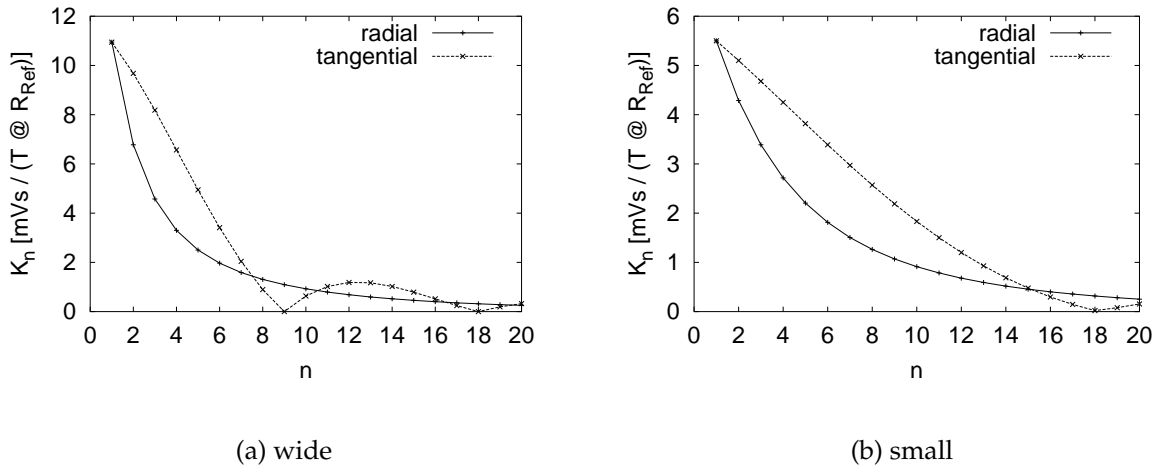


Figure 2.5: Sensitivity K_n of the coils (in Millivolt Seconds per Tesla at reference radius) to the multipole n . The sensitivity of the radial coil was calculated using Equation (2.27). The sensitivity of the tangential coil was calculated using Equation (2.29). For the plot labelled “wide” a coil with one turn was taken with $L = 1\text{ m}$. R_2 and R_c were set to 16 mm . R_1 was set to $\approx 5.0\text{ mm}$ and $\delta = 2\pi/9$. For the plot labelled “small” a coil with one turn was taken with $L = 1\text{ m}$. R_2 and R_c were set to 16 mm . R_1 was set to 10.5 mm and $\delta \approx 2\pi/18$. These parameters give the same coil width for the tangential coil and the radial coil in each plot. One can see the steadily decreasing sensitivity of the radial coil. The tangential coil’s sensitivity shows minima along the spectrum.

the harmonic order. The trait for each coil type is nicely visible. The sensitivity of the radial coil is steadily decreasing for higher harmonics. The tangential coil has a minimum along the spectrum. Its location is set carefully by choosing the opening angle δ .

In the system described here a tangential coil is only used for axis measurements. It is described in Chapter 3 in full detail. As the tangential coil is only used for axis measurements, the highest needed harmonic is the octupole. Choosing $\delta \approx 2\pi/9$ (see Equation 2.29) a high sensitivity was achieved for the quadrupole axis measurement still allowing to measure the octupole’s axis with a sufficient precision.

2.4 Compensated systems

In an accelerator magnet the main harmonic is typically 10^4 times stronger than the other harmonics. This means that the voltage signal induced by the main harmonic is $\approx 10^4$ stronger than the voltage signal induced by the other harmonics. The other

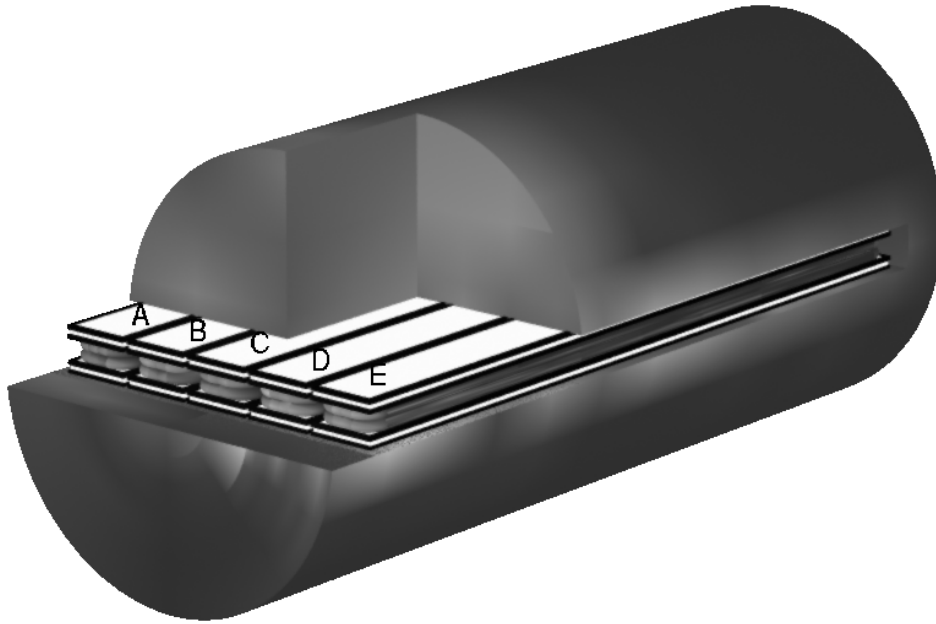


Figure 2.6: The field coil array (vulgo “harmonic coil”). One can clearly see the radial coil layout. All coils are located on one plane. The rotation axis coincides with the centre of the cylinder. The coil E is a spare coil. Drawing not to scale.

harmonics have to be measured with an accuracy to 2 ppm (see Table 1.1). A sophisticated arrangement of coils allows to measure the higher order harmonics with a system that has a very low sensitivity to the main harmonic increasing the tolerances required for the mechanics and electronics. The mechanical advantages are discussed in Section 2.6. Without this arrangement the electronics had to measure the induced voltage with a precision of $\approx 2\text{ ppm}$ which assumes a dynamic range of the measuring channel in the order of 10^6 to cover all needs (i.e. resolving $10\text{ }\mu\text{V}$ on a level of 5 V). This is technically hardly achievable, therefore the field measurement is split into two parts:

- the *absolute* part. One single coil is used to measure the field strength and its angle. The electronic system must guarantee a precision of $\approx 10^{-4}$ to allow the field strength measurement with the required precision ($1.5 \cdot 10^{-4}$).
- the *compensated* part, which is used to measure the higher order harmonics. Here an array of coils is used. They are located on one common body and arranged in such a way that a simple summation of the signals allows to cancel or at least reduce the dipole and quadrupole component (see Figure 2.6). Due to this reduction the voltage induced by the higher order harmonic has only to

be measured with a precision of $\approx 10^{-4}$ instead of $\approx 10^{-6}$ (i.e. $10 \mu V$ on a level of $50 mV$) which allows to reduce the requirements to the electronics by two to three orders of magnitude.

In our field quality measurement system only radial coils are used (see Figure 2.6). Coil A is used for the absolute system as it has the highest sensitivity to the main field. For the compensated system the signals of coils A to D are summed up using: $A - B - C + D$. For a perfectly manufactured array the dipole and quadrupole components would cancel. However small values are left due to small coil imperfections occurring in the fabrication, due to errors in the geometry of the coils on the support and due to the support misalignment with respect to its axis of rotation. These errors are on the order of micrometers. Therefore the bucking factor b is defined by

$$b = \frac{K_{m_{abs}}}{K_{m_{cmp}}}, \quad (2.30)$$

with $K_{m_{abs}}$ the sensitivity of coil A to the main multipole and $K_{m_{cmp}}$ the sensitivity to the main multipole of the coil array $A - B - C + D$. This factor has to be measured and is equal to the ratio:

$$\frac{V_{m_{abs}}}{V_{m_{cmp}}}, \quad (2.31)$$

with $V_{m_{abs}}$ the voltage induced in the absolute coil by the main multipole and $V_{m_{cmp}}$:

$$V_{m_{cmp}} = V_{m_a} - V_{m_b} - V_{m_c} + V_{m_d}, \quad (2.32)$$

with V_{m_a} the voltage induced in coil A by the main multipole and similarly for the coils B, C, D . For a dipole system a good bucking factor is in the range of 1000, for a quadrupole system in the range of 100 [16], because the dipole sensitivity is proportional to z^1 and the quadrupole sensitivity is proportional to z^2 (see equation (2.16)). The harmonic coil of the system described here has a quadrupole bucking factor of 300. Therefore the electronics of the system described here only needs to resolve $10 \mu V$ on a level of $\approx 1.5 mV$ to achieve a precision of $2 ppm$. The comparison between the sensitivity of the absolute and compensated system is given in Table 2.1 and Figure 2.7.

Table 2.1: The sensitivities of the coil array. The K_n labelled absolute represent the sensitivity for the main coil and the K_n labelled compensated represent the sensitivity of the compensated array. The values $|K_n|$ are plotted in Figure 2.7.

n	K_n			K_n		
	absolute			compensated		
1	13.6229	+	0.0341i	-0.0265	+	0.0409i
2	11.5682	+	0.0289i	0.0221	+	0.0249i
3	9.9596	+	0.0256i	9.8604	+	0.0270i
4	8.6886	+	0.0235i	6.2518	+	0.0224i
5	7.6749	+	0.0222i	7.6888	+	0.0226i
6	6.8585	+	0.0214i	6.2624	+	0.0210i
7	6.1944	+	0.0210i	6.2003	+	0.0212i
8	5.6489	+	0.0209i	5.4890	+	0.0208i
9	5.1962	+	0.0210i	5.1983	+	0.0210i
10	4.8169	+	0.0211i	4.7716	+	0.0211i
11	4.4960	+	0.0214i	4.4967	+	0.0214i
12	4.2220	+	0.0217i	4.2087	+	0.0217i
13	3.9859	+	0.0220i	3.9861	+	0.0220i
14	3.7807	+	0.0223i	3.7767	+	0.0223i
15	3.6008	+	0.0227i	3.6009	+	0.0227i

2.5 Analytical expressions for mechanical imperfections of rotating coil systems

The above formulae describe a perfect system. In the real world we have to consider a system of the type (setting $\theta' = \theta(t)$ in Equation 2.15)

$$\Phi(t) = Re \left\{ \sum_{n=1}^M K'_n(t) C_n(t) \exp[in\theta(t)] \right\}. \quad (2.33)$$

$C_n(t)$ describes dynamic effects in the magnet, $K'_n(t)$ the real coil sensitivities and their imperfections. The latter are:

- transversal vibrations of the coil as a rigid body with respect to the rotation axis
- torsional vibrations of the coil as a rigid body with respect to the angular ref-

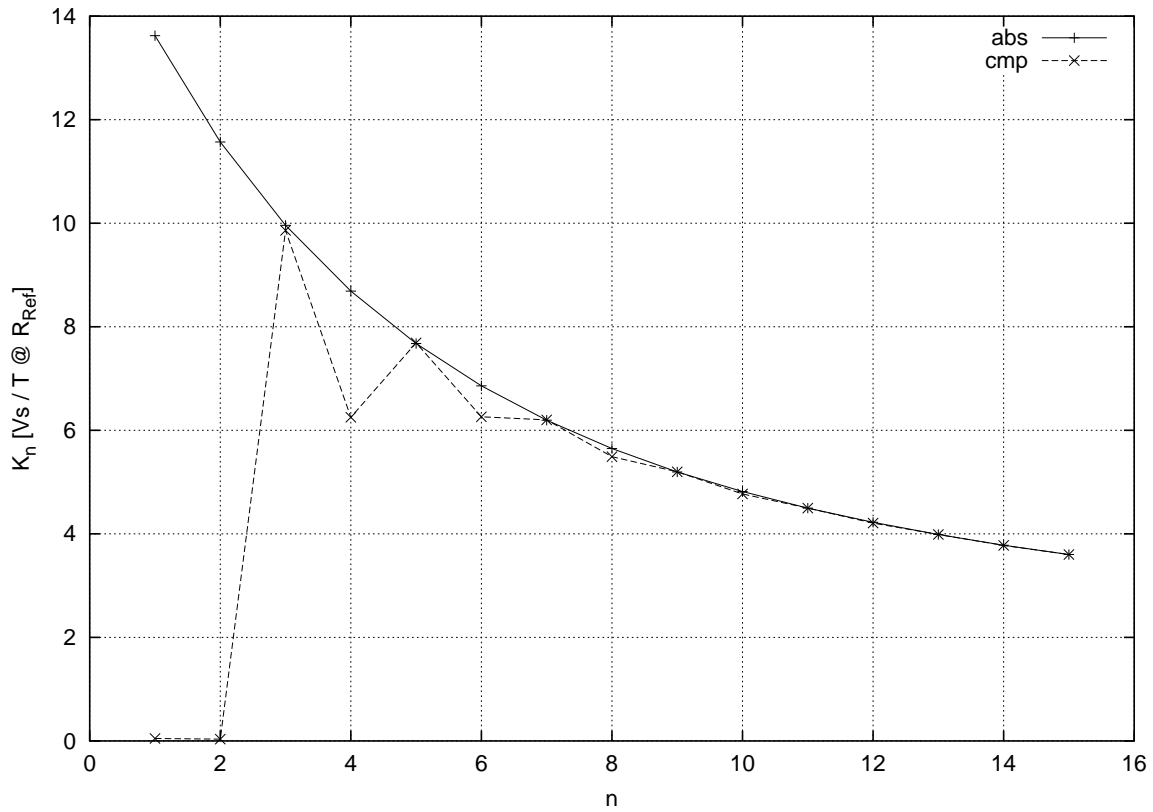


Figure 2.7: Comparison of the sensitivities K_n in (Volt seconds per Tesla at the reference Radius) for the absolute (abs) and the compensated (cmp) system versus the harmonic n for the harmonic probe. The absolute sensitivity shows the typical characteristics of a radial coil. The sensitivity to the dipole and quadrupole component is almost zero for the compensated system. The higher order harmonics match the system.

erence

- vibration of the coil body itself

In reality it is, however, impossible to know how the sensitivity of the coil changes versus time. Therefore one tries to single out the original K_n from the K'_n . The remaining term is seen as a perturbing term generating spurious harmonics diminishing the quality of the measuring system.

$\theta(t)$ describes the turning of the coil. In the ideal case

$$\theta(t) = \omega t, \quad (2.34)$$

with ω the angular velocity of the coil. Non ideal rotation introduces fake harmonics. An analytical expression for these is given in section 2.5.2. These calculations were presented in [27] and [26]. The calculations here follow the approaches of [26].

In the following analytical expressions are given for transversal vibrations and torsional vibrations of a coil in a pure quadrupole field,

$$C_n = 0 \quad \text{for} \quad n \neq 2.$$

2.5.1 Transversal displacements in a pure quadrupole field

To allow a correct measurement of the harmonics the axis of rotation must be stable. Here formulas are developed describing the spurious harmonics generated by a unstable rotation.

In the following the first factor of equation (2.16) is set to K_{const} and the second factor to K'_t

$$K'_n(t) = \underbrace{\left(\frac{N_w L R_{Ref}}{n} \right)}_{K_{const}} \underbrace{\left[\left(\frac{\mathbf{z}_2(t)}{R_{Ref}} \right)^n - \left(\frac{\mathbf{z}_1(t)}{R_{Ref}} \right)^n \right]}_{K_t(t)}, \quad (2.35)$$

introducing the time dependence of the wire position $\mathbf{z}_{1,2}$.

Assuming a disturbance $D(\theta)$ of the circular rotation of the coil, the sensitivity K_t is expressed by

$$K_t(t) = \left(\frac{\mathbf{z}_2 \exp(i\theta) + D(\theta)}{R_{Ref}} \right)^n - \left(\frac{\mathbf{z}_1 \exp(i\theta) + D(\theta)}{R_{Ref}} \right)^n. \quad (2.36)$$

Assuming $D(\theta)$ to be a periodic function of the type

$$D(\theta) = \sum_{q=-\infty}^{\infty} D_q e^{iq\theta}, \quad (2.37)$$

one can derive a spurious harmonic (see Appendix A.1.1), with overlined symbols indicating the complex conjugate

$$C_q^s = \frac{K_1}{K_q} \frac{D_{q-1}}{R_{Ref}} C_2 + \frac{\overline{K_1}}{K_q} \frac{\overline{D_{-q-1}}}{R_{Ref}} \overline{C_2}. \quad (2.38)$$

In the following the formulae for simple misplacements are given. These establish an orthogonal space in which all other vibrations can be described as the superposition of the basis.

Constant displacement

A constant translation $D(\theta) = D_0$ of the coil's rotation axis with respect to the coordinate system introduces a spurious harmonic

$$C_1^s = \frac{D_0}{R_{Ref}} C_2. \quad (2.39)$$

This effect is called feed down.

Periodic displacement of the rotation axis in $\cos(p\theta)$

A displacement of $D(\theta)$

$$D(\theta) = d \cos(p\theta) = \frac{d}{2} e^{ip\theta} + \frac{d}{2} e^{-ip\theta} \quad (2.40)$$

generates spurious harmonics of the type $p + 1$ and $p - 1$

$$\begin{aligned} C_{p+1}^s &= \underbrace{\frac{K_1}{R_{Ref} K_{p+1}}}_{\text{coil array}} \frac{d}{2} C_n \\ C_{p-1}^s &= \underbrace{\frac{\bar{K}_1}{R_{Ref} K_{p-1}}}_{\text{coil array}} \frac{\bar{d}}{2} \bar{C}_n \end{aligned} \quad (2.41)$$

The first term is determined by the coil array (thus marked coil array).

Periodic displacement of the rotation axis in $\sin(p\theta)$

A displacement of $D(\theta)$

$$D(\theta) = d \sin(p\theta) = \frac{d}{2i} e^{ip\theta} - \frac{d}{2i} e^{-ip\theta} \quad (2.42)$$

generates spurious harmonics of the type $p + 1$ and $p - 1$

$$\begin{aligned} C_{p+1}^s &= \underbrace{\frac{K_1}{R_{Ref} K_{p+1}}}_{\text{coil array}} \frac{d}{2} - i C_n \\ C_{p-1}^s &= -\underbrace{\frac{\bar{K}_1}{R_{Ref} K_{p-1}}}_{\text{coil array}} \frac{\bar{d}}{2} - i \bar{C}_n \end{aligned} \quad (2.43)$$

2.5.2 Shaft torsional vibrations / angular encoder incorrect triggering

The angular encoder is supposed to measure the angle of the rotating coil versus time. Three types of imperfections may decrease the accuracy of this measurement:

- *torsional imperfections* of the mechanical connections. The coil connection to the encoder is not sufficiently stiff. An example are eigen frequencies of these connections or angular lag between the real orientation of the coil and the current angle measured by the angular encoder.
- *incorrect timing* of the trigger. The measurement is triggered by the angular encoder. At each angle α_i a trigger impulse is sent to the readout controller which reads the current value from the integrator. If voltage spikes are induced into the trigger line, the electronics could interpret it as a trigger signal.
- *angular errors* of the encoder. Inside the encoder the angular counts are read from a disk mask fixed to its axis. If the mask was not precisely fabricated, it will generate trigger impulses at the wrong angle.

All these imperfections affect the measurement of the angular position of the probe, which generates spurious harmonics.

For considering a vibration of type $\theta = \theta_a + T(\theta_a)$ between the coil and the angular encoder, where θ_a is the reading of the angular encoder, $\mathbf{z}_{1\theta'}$, $\mathbf{z}_{2\theta'}$ in equation (2.14) are set to

$$\begin{aligned}\mathbf{z}_{1\theta'} &= \mathbf{z}_1 \exp(i\theta') \exp[inT(\theta_a)] \\ \mathbf{z}_{2\theta'} &= \mathbf{z}_2 \exp(i\theta') \exp[inT(\theta_a)].\end{aligned}\quad (2.44)$$

Inserting $\mathbf{z}_{1\theta'}$, $\mathbf{z}_{2\theta'}$ for $\mathbf{z}_{1,2}$ in Equation (2.13) one can calculate the coil sensitivities \mathbf{K}'_n to

$$\mathbf{K}'_n(\mathbf{t}) = \underbrace{\left(\frac{N_w L R_{Ref}}{n}\right)}_{K_{const}} \underbrace{\left[\left(\frac{\mathbf{z}_2}{R_{Ref}} \exp[inT(\theta_a)] \right)^n - \left(\frac{\mathbf{z}_1}{R_{Ref}} \exp[inT(\theta_a)] \right)^n \right]}_{\mathbf{K}_t(\mathbf{t})}. \quad (2.45)$$

If $T(\theta_a)$ is a periodic function, it can be written as a Fourier series

$$T(\theta_a) = \sum_{q=-\infty}^{\infty} \mathbf{T}_q \exp(iq\theta_a). \quad (2.46)$$

The generated spurious harmonics C_q^s (See appendix A.1.3) can be given as

$$C_q^s = \frac{n\mathbf{K}_n}{\mathbf{K}_q} \mathbf{T}_{q-n} i\mathbf{C}_n - \frac{n\overline{\mathbf{K}_n}}{\overline{\mathbf{K}_q}} \mathbf{T}_{-q-n} i\overline{\mathbf{C}_n}. \quad (2.47)$$

They are proportional to the sensitivity \mathbf{K}_n to the n^{th} harmonic. In the following the harmonics for simple vibrations are given.

Case of a small angular shift in $\cos(p\theta_a)$

If the angular shift is $T(\theta_a) = \zeta \cos(p\theta_a)$

$$T(\theta_a) = \zeta \cos(p\theta_a) = \frac{\zeta}{2} e^{ip\theta_a} + \frac{\zeta}{2} e^{-ip\theta_a}. \quad (2.48)$$

The only spurious harmonics generated for this case are

$$\begin{aligned} C_{p+n}^s &\approx \underbrace{\frac{nK_n}{K_{p+n}}}_{\text{coil array}} \frac{\zeta}{2} i C_n \\ C_{p-n}^s &\approx \underbrace{-\frac{n\bar{K}_n}{K_{p-n}}}_{\text{coil array}} \frac{\zeta}{2} i \bar{C}_n. \end{aligned} \quad (2.49)$$

Case of a small angular shift in $\sin(p\theta_a)$

If the angular shift is $T(\theta_a) = \zeta \sin(p\theta_a)$

$$T(\theta_a) = \zeta \sin(p\theta_a) = \frac{\zeta}{2i} e^{ip\theta_a} - \frac{\zeta}{2i} e^{-ip\theta_a}. \quad (2.50)$$

The only spurious harmonics generated are:

$$\begin{aligned} C_{p+n}^s &\approx \underbrace{\frac{nK_n}{K_{p+n}}}_{\text{coil array}} \frac{\zeta}{2} C_n \\ C_{p-n}^s &\approx \underbrace{\frac{n\bar{K}_n}{K_{p-n}}}_{\text{coil array}} \frac{\zeta}{2} i C_n. \end{aligned} \quad (2.51)$$

2.6 Spurious harmonics generated in compensated systems

For mechanical imperfections the degree of sensitivity to the quadrupole and dipole harmonic determines the magnitude of the spurious harmonic (see Equation (2.47) and (2.38)). In compensated system these sensitivities are reduced by the bucking factor (Equation 2.30). Therefore an error source generates a spurious harmonic in a compensated system, which is by the bucking factor smaller than the spurious harmonic generated in the absolute system. In Figure 2.8 the sensitivity of the coil

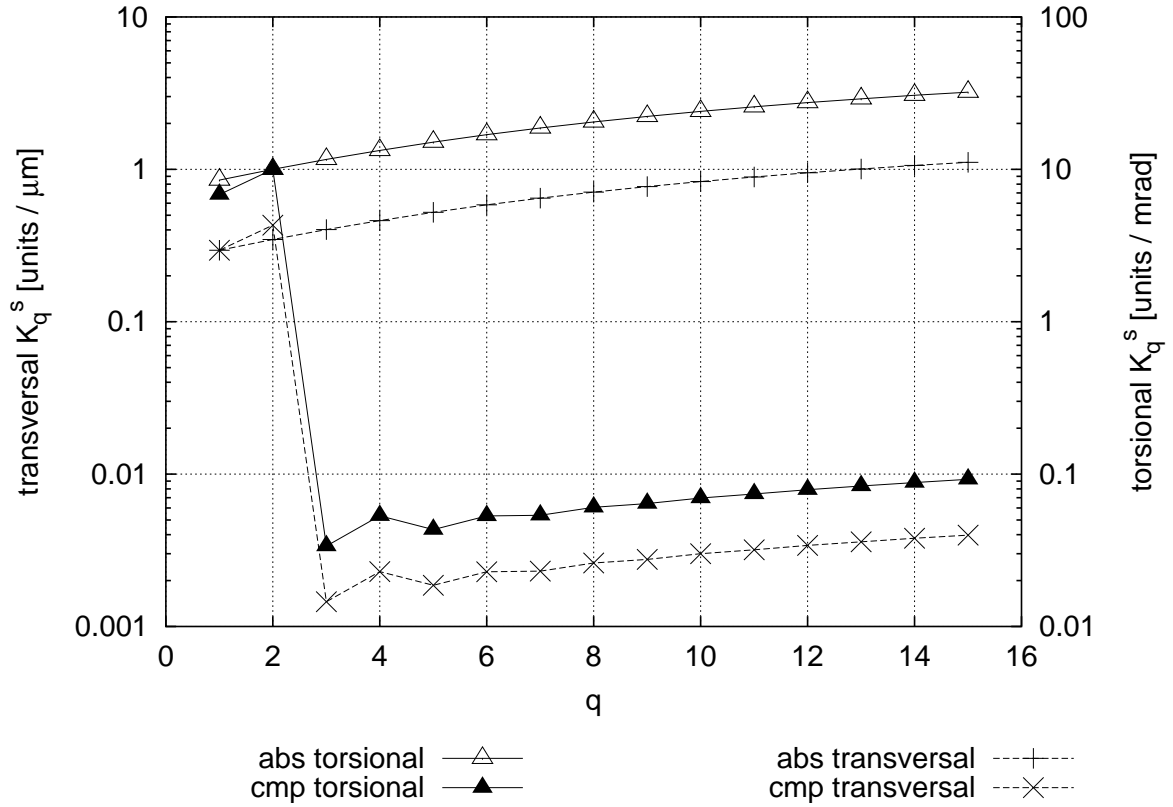


Figure 2.8: The sensitivities K_s (in Volt seconds per Tesla at the reference radius) of the absolute and the compensated system to mechanical vibration versus the order of the vibration q in a pure quadrupole system. $|pK_2/K_q|$ is plotted for the torsional vibration and $|K_1/K_q|$ for the transversal vibration. *abs* denotes the absolute system and *cmp* the compensated one. One can see that the spurious harmonics for the compensated system are by a factor of 300 smaller than the spurious harmonics for the absolute one.

array to the imperfections is plotted (i.e the absolute value of the factors marked afore “coil array”). For torsional vibrations $|2K_2/K_q|$ is plotted (evaluating the first term of Equation 2.51 for a quadrupole [$n=2$]). Thus, to estimate the effect of a transversal vibration with $p = 2$ one has to take the values of $q = 2 - 1 = 1$ and $q = 2 + 1 = 3$ (see Equation (2.43)) and multiply it with half the amplitude and the field strength. The corresponding spurious multipoles can be calculated by using (2.47) or for vibrations of type $\sin(p\theta)$ using (2.51). For harmonics induced by transversal vibrations $|K_1/(K_q R_{Ref})|$ was plotted. One can calculate the induced harmonics using (2.38) and for vibrations of type $\sin(p\theta)$ using (2.43).

The above statement is only valid for a stiff coil array. Otherwise the sensitivity of the compensated coil array (K_1 , K_2) to the dipole and quadrupole harmonic

changes and the above formulae are not valid any more. In this case one has to consider each coil separately and add their effects and sum them up taking the compensation gains into account.

Summary

Rotating coils allow to measure the integral of the magnet multipoles over the length of the coil. For our harmonic measurement a radial coil was chosen, because it has a more or less constant sensitivity and is simple to build. For the axis measurement a tangential coil was chosen to allow the mounting of a survey reference in its centre. Using a compensated coil array for the measurement of the higher order harmonics the requirements to the electronic and mechanical systems can be reduced. The effect of mechanical imperfections was given in section 2.5.1 and 2.5.2. Torsional vibrations induce spurious harmonics proportional to $K_2 \cdot C_2$, transversal vibrations induce spurious harmonics proportional to $K_1 \cdot C_2$.

Chapter 3

Description of the measurement system

360 arc quadrupoles and some tens of special SSS's have to be measured in cold condition. The main field has to be measured with a precision of $1.5 \cdot 10^{-4}$ and its angle to 0.2 mrad (For all requirements see Table 1.1). As these magnets have to be tested under operating condition the following systems need to be provided:

- *Cryogenic cooling equipment:* The magnets are operated at 1.9 Kelvin using superfluid helium. So a feeding box is needed to provide an inlet for the helium at various temperatures (as inside the cryostat more than one temperature level exists), and liquid nitrogen. All connections to the magnet need to pass the cryogenic station as cooling at 1.9 Kelvin runs with an efficiency of approximately 0.1%.
- *Quench protection system:* The magnets use superconducting technology. The superconductivity of the cables can break down for various reasons. Such a transition is called a “quench”. But then the current still needs to be transported. Without interaction all electrical energy would be dissipated at the break down spot potentially damaging the magnet. Thus, a quench protection system is needed, which measures the voltage drop of the magnet coil. A resistance indicates that a quench has occurred. If so the quench protection system activates the heaters, which turn the whole magnet in non superconducting mode and therefore the whole magnet dissipates its stored electrical energy.
- *Measurement structure:* The outermost shell of the cryostat is evacuated (see

Figure 1.10). In the LHC all magnets are connected one to another. In the measurement the magnets are connected to the feeding box at one side and at the other side the magnet is closed with an end cap. As the cross section is large, a pressure in the order of metric tons is generated on the end caps, which can deform the magnet. Therefore a mechanical structure has to enforce the feeding box and the end cap.

- *Power supplies:* The magnets have to be supplied with a current of up to 12 kA . During ramp voltages are up to 0.5 V . The cables connecting the magnet to the power supply however have a much higher resistance. Therefore the power supply can deliver up to 14 kA and 15 V .

The measurement system is located in the hall SM18, which is dedicated to magnetic measurement of cold magnets for the LHC machine (see Figure 3.1). The measurement system is based on rotating coils. Due to the strong magnetic fields inside the magnet the rotating unit, the associated angular encoder and the level meter are placed outside of the magnet demanding a long stiff mechanical connection between these devices and the coils. Choosing a ceramic shaft the necessary stiffness can be achieved. The voltage signal from the coils is processed by a preamplifier and electronically integrated using a precise digital integrator based on a voltage to frequency converter. The readout of the integrator is triggered by the angular encoder to ensure angular equidistant steps. This signal is then Fourier transformed. Taking the geometric factors of the coils into account one can compute the harmonics of the magnetic field.

As the magnet is operated at a temperature of 1.9 K , an anti-cryostat has to be mounted inside the magnet to allow the measurement of the field inside the aperture at room temperature. This anti-cryostat is of cylindric shape. Its axis may vary in a range of up to 2 mm along one metre. Therefore a reference system is established by a telescope to measure the coil's position inside the anti-cryostat. Using two reference quadrupoles the telescope frame can be attached to the SSS's fiducials.

3.1 Mechanical setup of the measurement system

The measuring system for the Arc SSS's (see Figure 3.2) consists of the motorised rotating unit, the shaft and the coil and is called "Antbear". It forms the mechanical

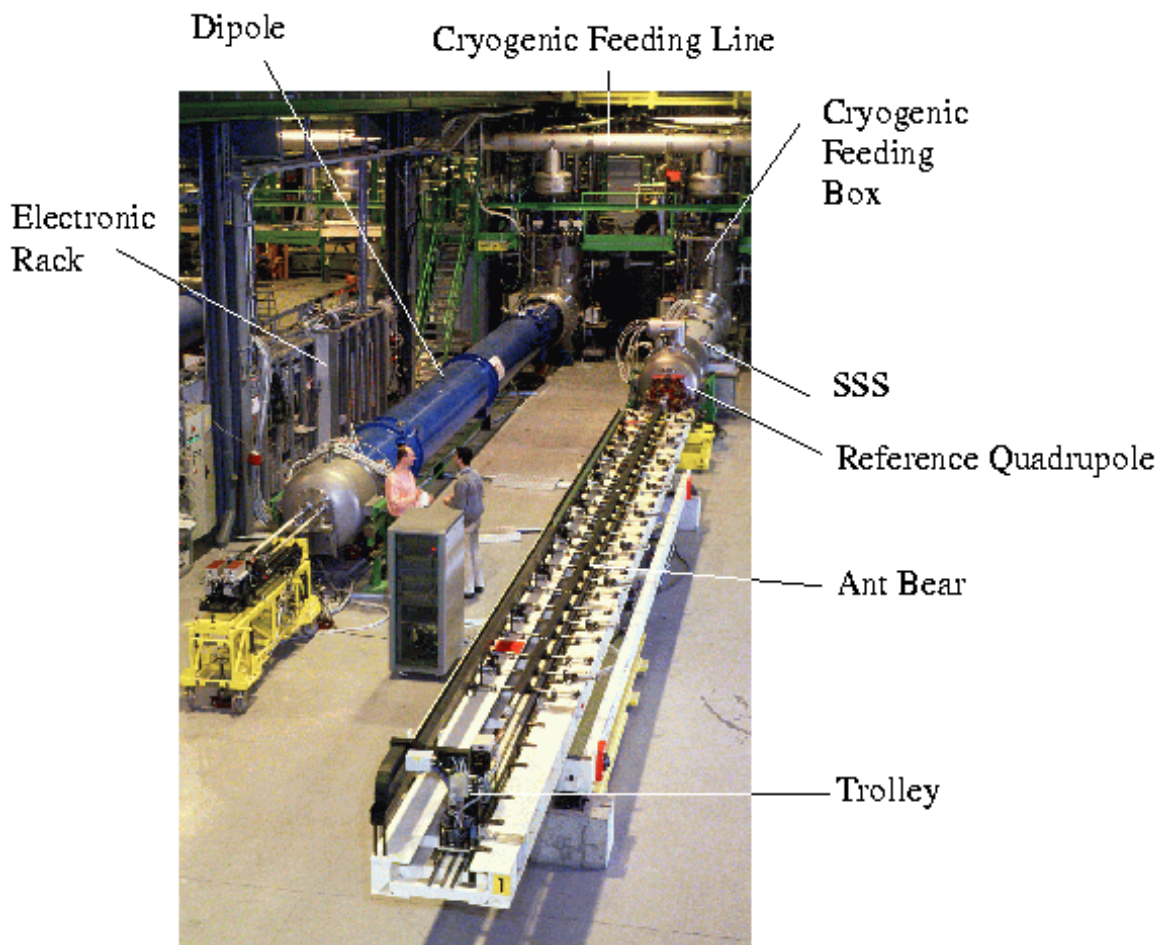


Figure 3.1: Setup of the quadrupole measurement bench in the hall SM 18. On the left in the horizontal blue cryostat a dipole is cooled for magnetic measurement. On the right the white cryostat of a SSS is visible. The Antbear is placed in front. The rotating unit is mounted on a trolley. This trolley can be placed arbitrarily.

part of the measurement system. The shaft can travel inside the half shells of the Antbear. The rotating unit together with the angular encoder and the inclinometer are mounted on a trolley. This trolley can be placed arbitrary at any longitudinal position. The motor of the rotating unit turns the shaft. At the end of the shaft the harmonic coil and the axis searching coil are mounted. This whole bench is fully automated and controlled by software. At each measurement point the rotating unit accelerates the whole shaft during one revolution, measures during one revolution and decelerates the shaft during one revolution. After that the whole procedure is repeated in the opposite direction. The average of these two measurements is independent of the angular lag of the shaft, while the difference allows to estimate the lag.

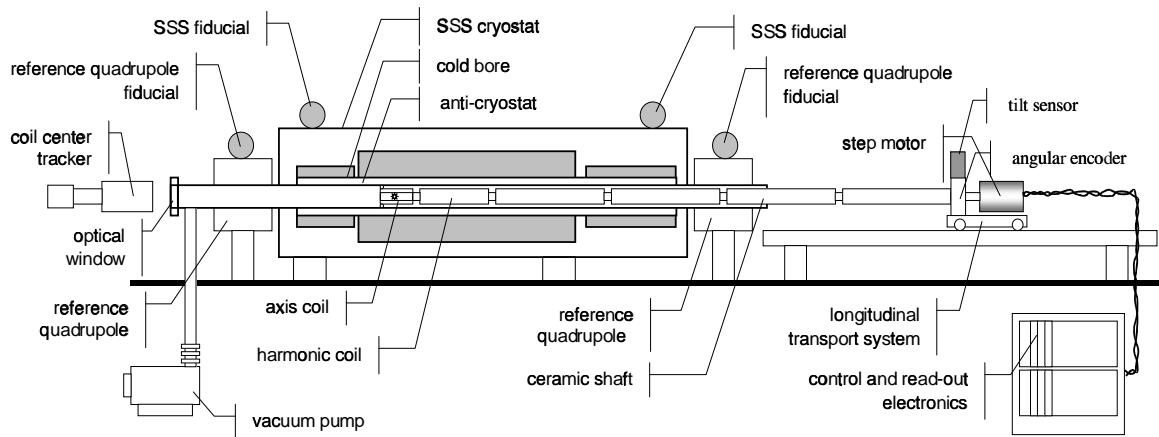


Figure 3.2: Sketch of the field quality measurement system. A stepping motor rotates the shaft, which is assembled of 8 elements. On the end of the shaft the two coils are mounted. The SSS is enclosed by two reference quadrupoles. The Antbear is visible on the right, the tracker on the left.

The shaft itself is composed of eight modules. Each module consists of a ceramic pipe (Al_2O_3) with two Vetresit (according to SN 277 208 and NF – C26 – 151) interconnects at the end. As the anti-cryostat is not totally straight, the shaft must be able to follow the shape. The harmonic coil's motion must not be disturbed by an axis kink between the coil array and the shaft. Therefore a lateral flexible “joint” still providing angular stiffness is formed by two titanium bellows (Ti_6Al_4V , see Figure 3.3) and the last shaft element (see Figure 3.2). One bellows connects the two last elements of the shaft, the other the last element and the harmonic coil array. This compound can accept a kink with an angle smaller than 0.1 mrad . As the shaft and the bellows must rotate inside high magnetic fields their materials must be non-magnetic (not to disturb the field) and non conducting. Otherwise the induced eddy currents would generate an unacceptable large torque on the whole mechanics. The bellows are rather small, therefore a titanium alloy was acceptable. The shaft supporting ball bearings are made of plastic except the last two, which are made of ceramic. The ceramic ball bearings guarantee a movement with a precision of $< 11\text{ }\mu\text{m}$ according to their specification [29]. All electrical cables transmitting the signals from the coils are placed inside the shaft.

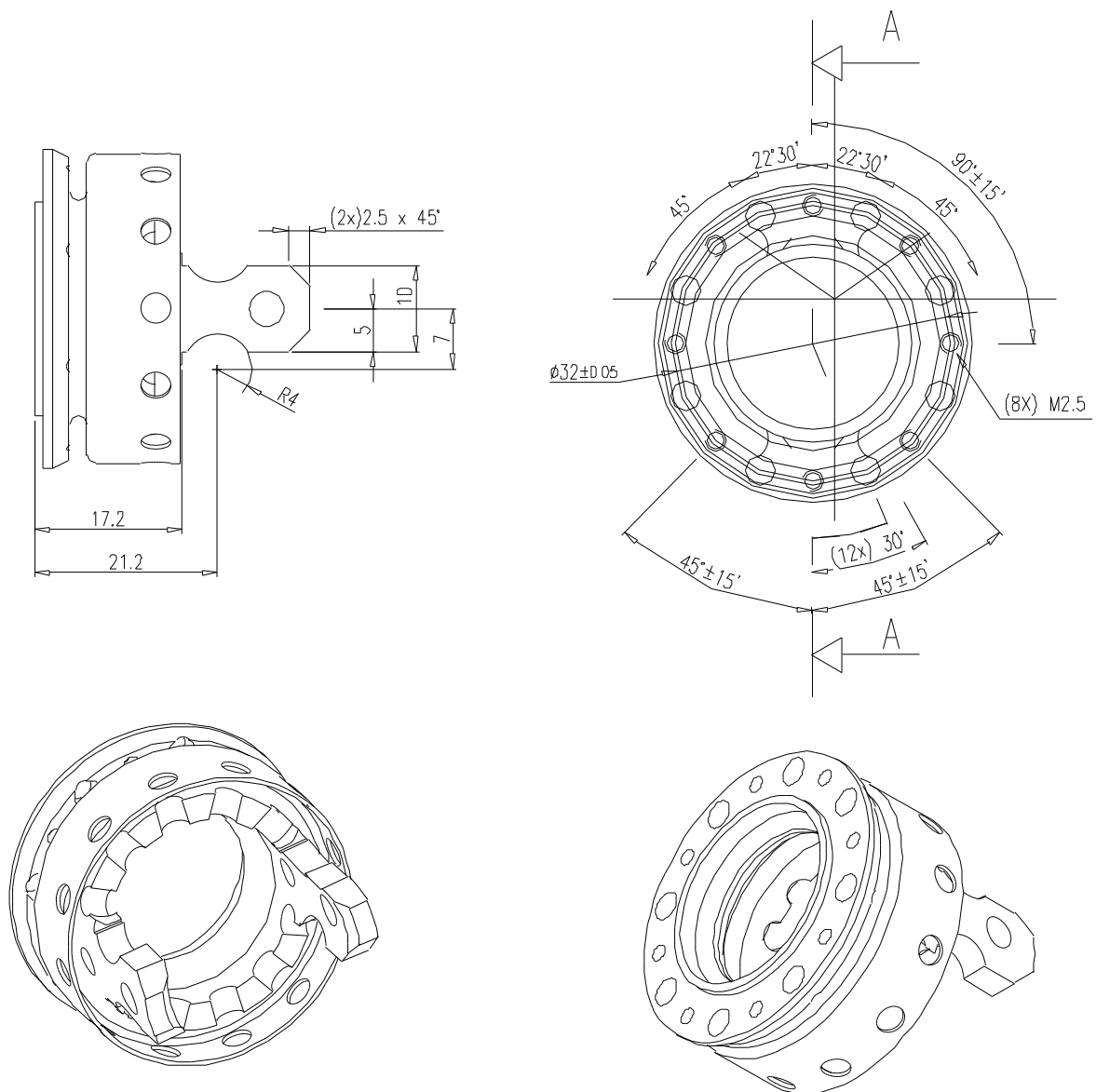


Figure 3.3: Different views of the bellows. A bellows connects the field quality coil array to the shaft and another the two last shaft segments. The bellows are made from a Titan - Aluminium - Vanadium alloy. Drawings not to scale. All dimensions in millimetres. All angles in degrees.

3.2 Coils used

Two coil arrays establish the core part of the magnetic measurement. A photo is shown in Figure 3.4. The field quality coil array has five radial coils (see Figure 3.5). The technical drawing of this coil is given in Figure 3.6. They are mounted in the middle of two half shells, which are made of Vetresit. These radial coils are all of the same type. The outermost coil (coil A) is used for the absolute measurement (See

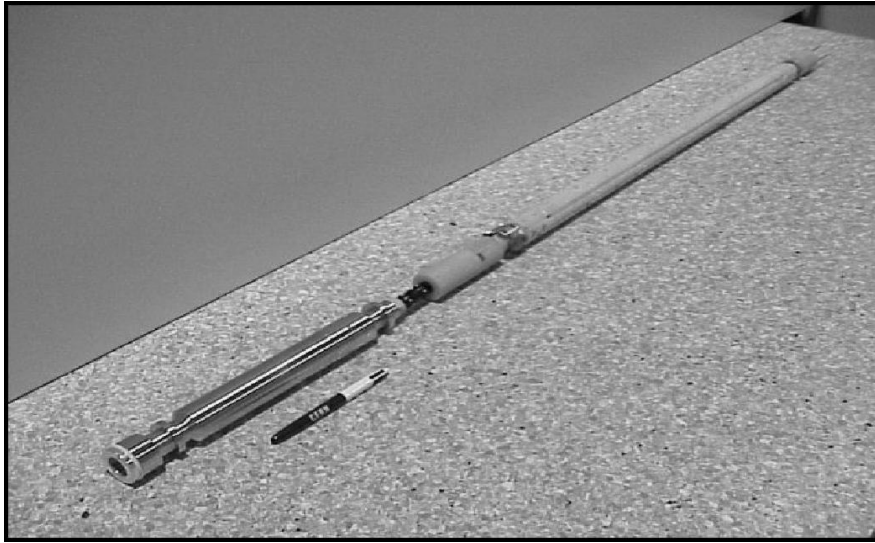


Figure 3.4: The field quality and the axis searching coil arrays. The field quality coil array has a length of 680 mm. The coils itself have a length of 600 mm. From the axis searching coil only the vacuum container is visible. It is made of non-magnetic stainless steel.

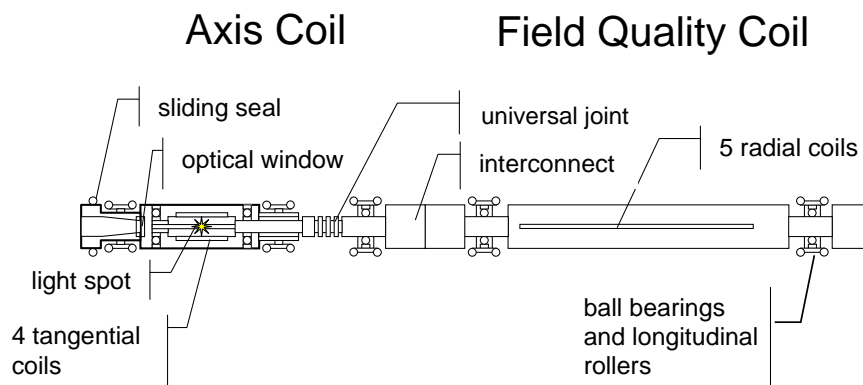


Figure 3.5: Sketch of the field quality and axis measurement coil arrays. These two arrays establish the core measurement system. The harmonic coil array consists of 5 radial coils. Each coil is $\approx 600\text{ mm}$ long. The array support is made of Vetresit. The ball bearings are made of ceramic. A universal joint transmits the rotation to the axis searching coil array. The axis searching coil array is mounted inside a stainless steel container which holds the seal.

Section 2.4 and Figure 2.6). From this measurement the field strength and angle is derived. An electrical connection of the type $A - B - C + D$ allows to compensate the quadrupole and the dipole. With this array the higher order multipoles are measured. The parameters of these coils are given in Table 3.1. The sensitivity of coil A versus the multipole is given in Figure 3.7.

For the higher order multipoles the sensitivity of the coil array is roughly the same as for coil A. The sensitivities for the dipole and quadrupole are roughly 300

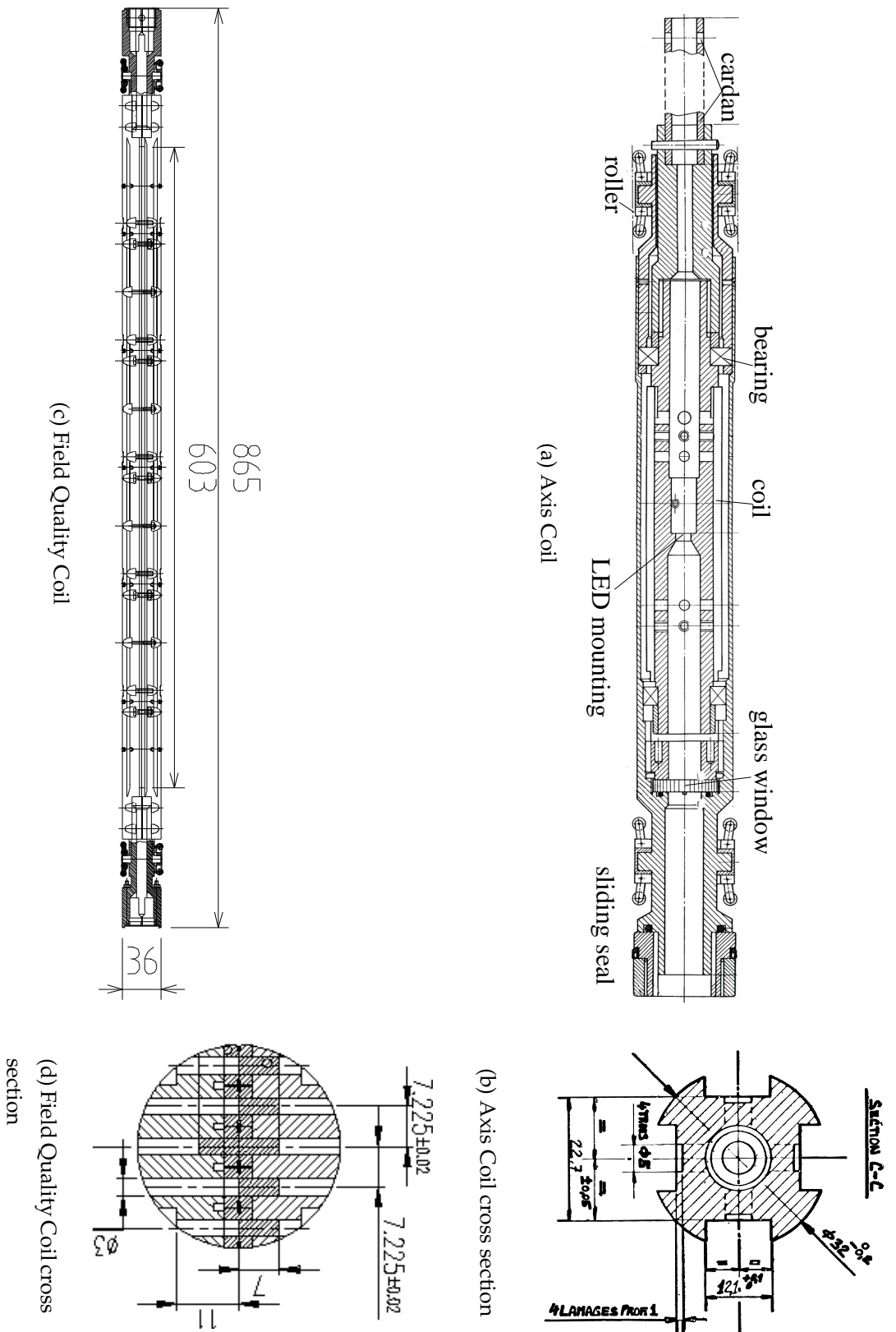


Figure 3.6: Technical drawing of the coils. Please note that the drawing are not to scale. All dimensions in millimetres. The cross section of the axis searching coil array shows nicely the layout of a tangential coil array body. The coil body gaps support the coils. The field quality coil is much longer than the axis searching coil. The cross section of the field quality coil shows the typical radial coil body. Two half cylinders support the measuring coils in the middle. The harmonic coil length differs slightly from the length given in Table 3.1 as here the outer length of the coil body is shown, in the aforementioned table the inner length is given. The bearings are made of ceramic. The coil bodies are made of Vetrest. The glass window is made of BK7. Its surfaces are planar with an optical quality of $\lambda/10$. The LED is mounted in the middle of the axis searching coil.

Table 3.1: Geometry of the harmonic coil array. The coil *A* is used for the absolute measurement. The coils *B – D* together with coil *A* form the compensated system. Coil *E* is placed as a backup. From the length and the radii the surface of a coil can be calculated. Here the calibrated magnetic surface A_m is listed. R_2 is the outer radius (in millimetres) and R_1 the inner radius (in millimetres). L describes the length of the coil (in millimetres) and N the number of windings. The angle θ_c (in rad) gives the angle of the coil to the x -axis.

Coil name	A_m [mm ²]	R_2 [mm]	R_1 [mm]	L [mm]	θ_c [rad]	N_w
A	231590	17.086	11.786	599.3	0	64
B	231720	9.844	4.544	599.3	0	64
C	231570	2.686	−2.614	599.3	0	64
D	231250	9.907	4.607	599.3	π	64
E	231110	17.139	11.839	599.3	π	64

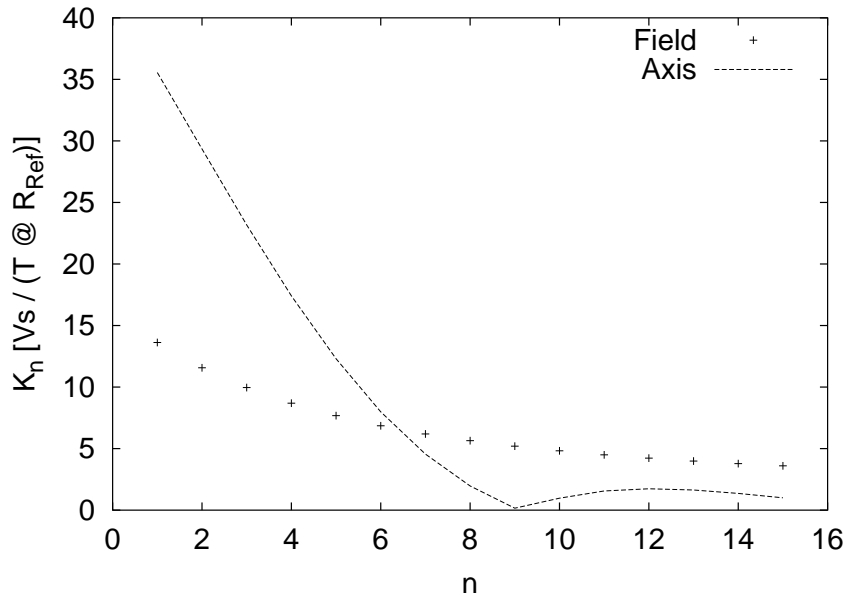


Figure 3.7: Sensitivity of the coil arrays. The sensitivity (in Volt seconds per Tesla at the reference radius R_{Ref}) is plotted versus the multipole n . The graph labelled “Field” shows the sensitivity of the absolute coil (coil *A*) of the field coil array. The graph labelled “Axis” shows the sensitivity of the coil *A* of the axis searching coil.

times smaller. A comparison of the compensated array to coil *A* is given in Figure 2.7.

The axis searching coil array is made of tangential coils. Four 100mm long coils are mounted on a common hollow cylinder. The parameter of these coils are given in Table 3.2. A Light Emitting Diode (LED) is mounted inside this cylinder on the

Table 3.2: Geometry of the axis searching coil. The coil A is used for the axis measurement. The other coils are placed as a backup. From the length and the width the surface of a coil is calculable. Here the calibrated magnetic surface A_m is listed. A_m is the magnetic surface (in millimetres) and R_c the radius of the cylinder on which the coil is placed (in millimetres). $w_t = R_c \sin(\delta)$ (in millimetres) is the width of the coil and L the length of the coil (in millimetres). θ_c describes the angle between the coil and the median plane and N_w , the number of windings.

Coil name	A_m [mm ²]	R_c [mm]	w_t [mm]	L [mm]	θ_c [rad]	N_w
A	604411	18.605	9.455	99	$\pi/2$	600
B	604422	18.605	9.455	99	π	600
D	604280	18.605	9.455	99	0	600
E	603731	18.605	9.455	99	$-\pi/2$	600

axis (see Figure 3.5). A diaphragm with a diameter of 0.2 mm is fixed in front of the LED. The axis searching coil array rotates inside a stainless steel cylinder. At the end of the cylinder a glass window of optical quality is mounted, whose necessity is discussed in Section 3.4.

3.3 Electrical setup of the measurement system

The signal from the coils has to be processed and analysed to yield the field properties. (The mathematical discussion was given in Section 2.2.4.) The first signal processing steps in these chain are performed by analogue and digital electronics.

To get the compensated signal the coils are galvanically connected on the patch panel as shown in Figure 3.8. The output of both systems is then amplified by preamplifiers. To obtain better independence from rotation instability the signal is integrated [27]. The angular encoder triggers the readout of the integrator and ensures that the flux is measured at equally spaced angular steps. The integrators [30, 31] are fabricated as VME Cards. An external controller then transfers the data to a computer for online measurement control and further data analysis.

The integrator consists of two main components:

1. A voltage to frequency converter (VFC). A voltage of 5 V is converted to a frequency of 250 kHz . With decreasing voltage the frequency decreases as well. A voltage of -5 V Volts is converted to 0 Hz .
2. A counter. It counts the pulses coming from the VFC. The total counts are

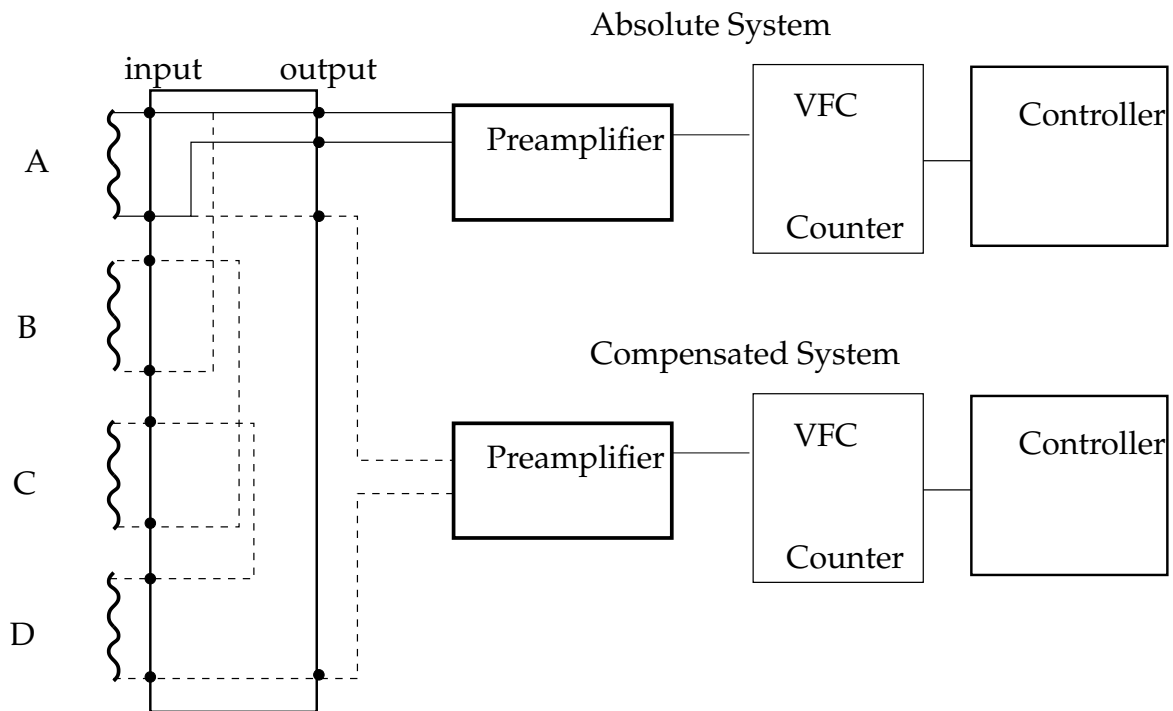


Figure 3.8: Electrical system setup. The solid lines indicate the cabling of the absolute coil. The dashed lines indicate the signal cables of the compensated system. The cables are connected to a preamplifier. The Voltage to Frequency Converter (VFC) and the counter form the integrator. A controller reads the signal out.

equal to the input of the VFC integrated over time.

The integrator is shipped with additional logic supporting a triggered readout of the counter and shift registers in order not to lose any input during readout.

3.4 Optical setup of the system

The magnetic field is measured inside the aperture, which has a diameter of 50 mm . An anti-cryostat with an inner diameter of 40 mm is mounted inside the aperture. The anti-cryostat surface can not be used as a reference, as its axis is varying arbitrarily up to 2 mm per metre. A tracker establishes a reference inside the magnet [32, 33]. It consists of a Cubic-PrecisionTM telescope and a CCD Camera, which is equipped with a digital signal processor (DSP). This device is called Short Range tracker (SRT). The cubic precision telescopes were developed for long distance high accuracy survey tasks (see also Figure 3.9).

The telescope images the diaphragm illuminated by the LED inside the axis

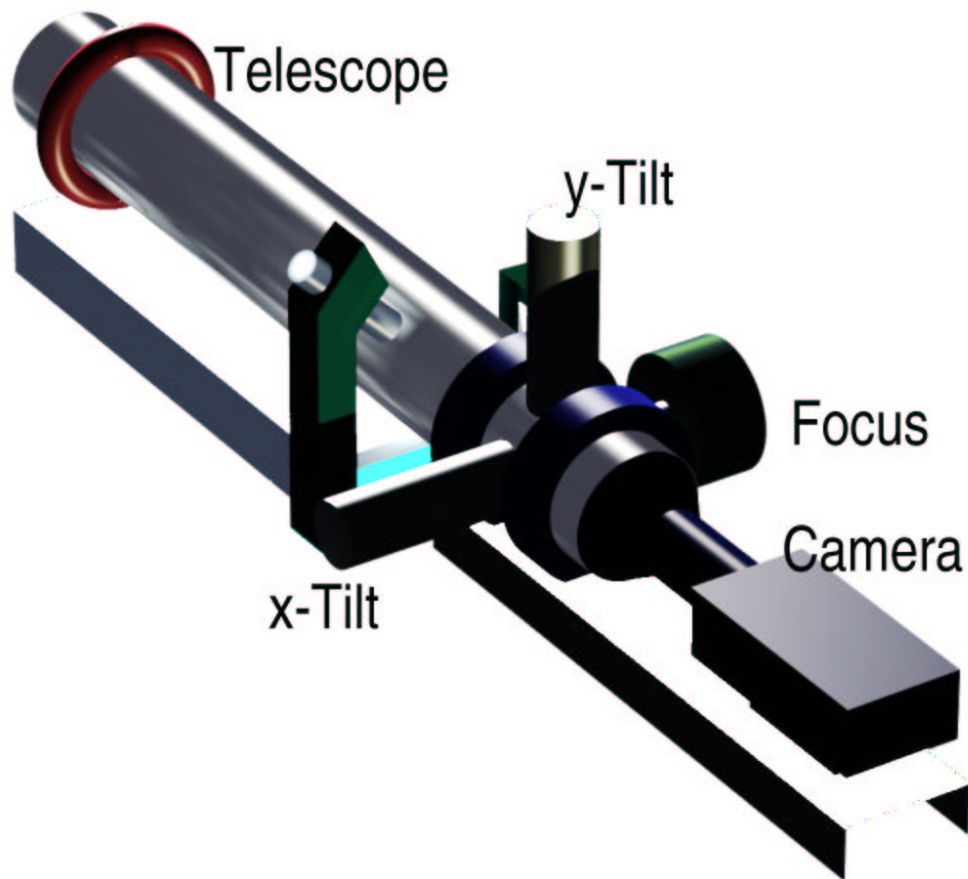


Figure 3.9: Sketch of the tracker system. It consists of two main parts. The telescope images the diaphragm on the CCD. The telescope is fully motorised. The focus knob is driven by a step motor. The tilt plates are also motorised. With the help of the tilt plates the image is brought as near to the middle of the CCD Chip as possible. The digital signal processor (DSP) reads the intensity values of the CCD Chip and calculates the position of the image. This sketch is not to scale.

searching coil on the CCD Chip. This telescope has two tilt plates in its optical path, which allow to introduce an offset into the optical axis in the two directions x and y . By turning these tilt plates the image is moved as near to the centre of the CCD Chip as possible (see Figure 3.10). The inclination of the tilt plates is recorded. After that the DSP reads the intensity values from the CCD Chip. To eliminate noise it sets anything under a threshold to zero. This threshold is set to 80 out of a maximum of 255 [34]. From the resulting image the centre of mass is calculated (in units of pixels). Two types of calibrations were performed with this telescope. One established the transformation factor from pixels to millimetre for the CCD - Camera (see Figure 3.11). This factor mainly depends on the distance between the camera and the telescope. The second calibration measured the transformation factor from the tilt plate angle (in steps of the used motors) to millimetres. This factor has a small

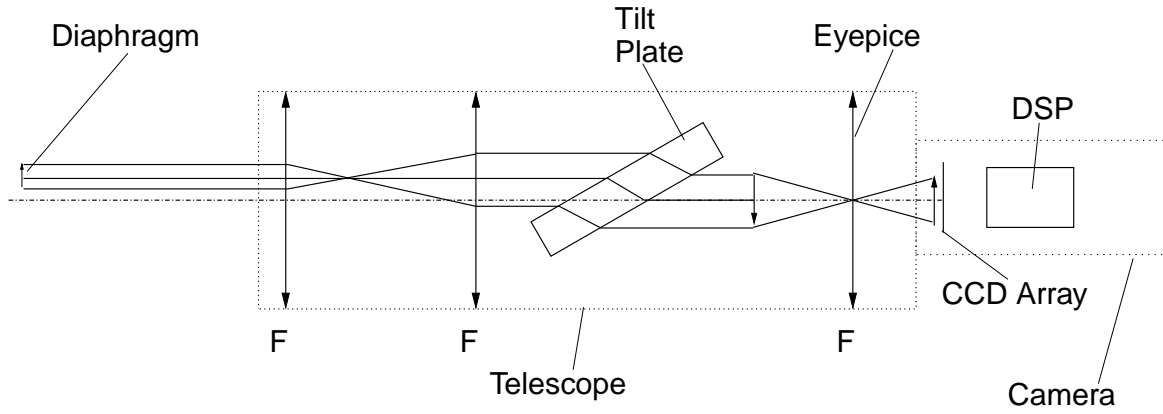


Figure 3.10: Sketch of the tracker system. This sketch is not to scale.

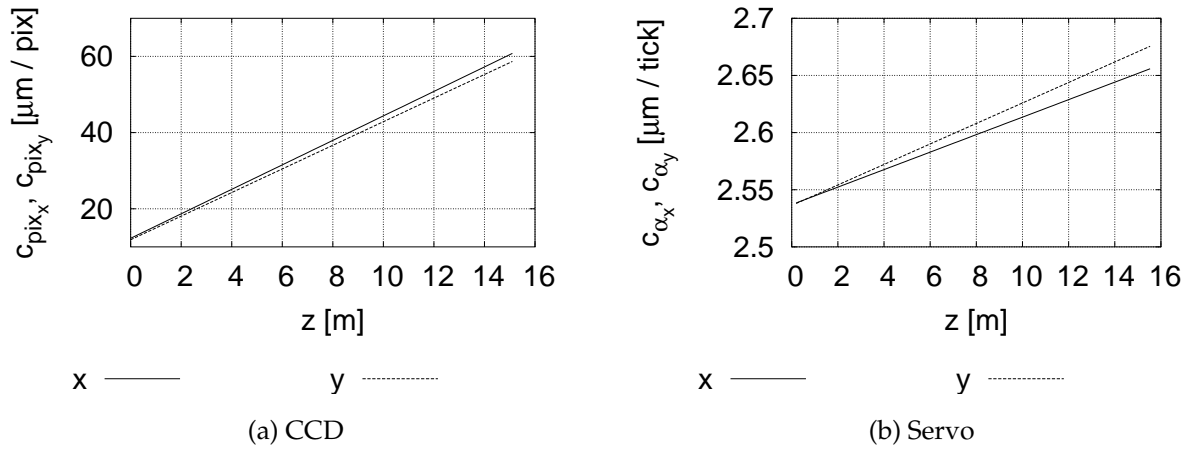


Figure 3.11: Scale factors for the tracker. The dependence of the scale factors on the distance between the telescope and the object z is shown here. c_{pix_x}, c_{pix_y} are the respective calibration factors for the CCD-Camera and $c_{\alpha_x}, c_{\alpha_y}$ the respective factors for the servos. The y coordinate is vertical, z points from the telescope to the object, and xyz establish a left hand coordinate system. The CCD labelled graph shows the factors for the CCD-chip. The Servo labelled graph shows the factors for the servos.

dependence on distance. The real offset of the image from the axis is given by

$$o_{tel_x} = o_{\alpha_x} \cdot c_{\alpha_x} + o_{pix_x} \cdot c_{pix_x} \quad (3.1)$$

$$o_{tel_y} = o_{\alpha_y} \cdot c_{\alpha_y} + o_{pix_y} \cdot c_{pix_y}, \quad (3.2)$$

with o_{tel} the offset measured by the telescope, $o_{\alpha_x}, o_{\alpha_y}$ – the offsets measured using the tilt plates, and o_{pix_x}, o_{pix_y} – the offsets measured by the CCD Camera, and $c_{\alpha_x}, c_{\alpha_y}, c_{pix_x}, c_{pix_y}$ – the corresponding calibration factors. The transfer of the telescope frame to the outer fiducials is discussed in Section 3.8.

As the anti-cryostat touches the cold mass via the cryogenic supports, heat drains off from the anti-cryostat inside. Therefore the inner tube of the anti-cryostat is heated by a wire producing a non constant temperature along the tube differing from the ambient temperature. Air inside this tube would create gradients possibly bending the light beam up a few millimetres [35]. Therefore the anti-cryostat is evacuated between the axis searching coil container and the optical window (see Figures 3.2 and 3.5). Through these windows the tracker measures the light spot.

3.5 The power supply

The current for the magnets is provided by a power supply. This power supply can deliver 13 kA at 600 V . The ripple of the power supply can influence the quality of the magnetic measurement. Connecting an oscilloscope to a coil the induced voltages due to the power supply's instabilities were measured. The biggest contribution was found to be 0.14 mV at a frequency of 3 Hz .

3.6 Measurement procedure

The bench is capable of measuring all magnetic parameters in one run. The whole setup allows to place the coil at any arbitrary longitudinal position. To obtain all field parameters all magnets have to be scanned. In the following all steps are outlined:

1. The harmonic coil is placed inside the first reference quadrupole. The angular offset of the Antbear's angular measurement system is measured with respect to gravity using the known direction of the reference quadrupole field.
2. The axis searching coil is placed inside the first reference quadrupole. A magnetic and an optical measurement are performed. This establishes the first point of the telescope reference frame. The vertical axis of this frame is aligned with gravity.
3. The harmonic coil is placed stepwise in the magnets to scan the whole field along the magnets.

4. The axis searching coil is placed inside the magnet with a step rate of 300 *mm*. At each step a magnetic and an optical measurement are performed. Even without covering the whole magnet, the axis can be measured with good precision, as the magnet and anti-cryostat deformation is smooth.
5. The harmonic coil is placed inside the second reference quadrupole. This measurement allows to control the twist of the shaft as the field direction of the second reference quadrupole is known. The angular offset of the Antbear's angular measurement system is measured. This measurement should be inside the acceptable error of $\approx 0.5 \text{ mrad}$.
6. The axis searching coil is placed inside the second reference quadrupole. A magnetic and an optical measurement are performed delivering the second reference point for the telescope frame.
7. A survey measurement is performed to measure the position of the reference quadrupoles with respect to the SSS's fiducials. Together with the calibration data of the reference quadrupoles, which measured the distance of the quadrupole's axes to their fiducials, the telescope frame is referred to the SSS's fiducials.

3.7 Analysis Procedure

3.7.1 From the electronic output to the Flux

The electronics provides the flux versus angle and versus time. The harmonics of the magnet have to be calculated with respect to the main multipole axis. For this result the following steps are necessary [36, 26]:

First the drift of the integrator has to be corrected [36]. The signal of the integrator $\Phi_I(t)$ can be described as

$$\Phi_I(t) = \int_0^t [f(t') + U_0] dt' = F(t) + U_0 \cdot t, \quad (3.3)$$

with f the signal from the coil and U_0 the input offset of the integrator (see also Figure 3.12).

The last point of the coil signal is measured at the same angular position as the first point. Therefore the signal must be identical as well. The integrator sets the

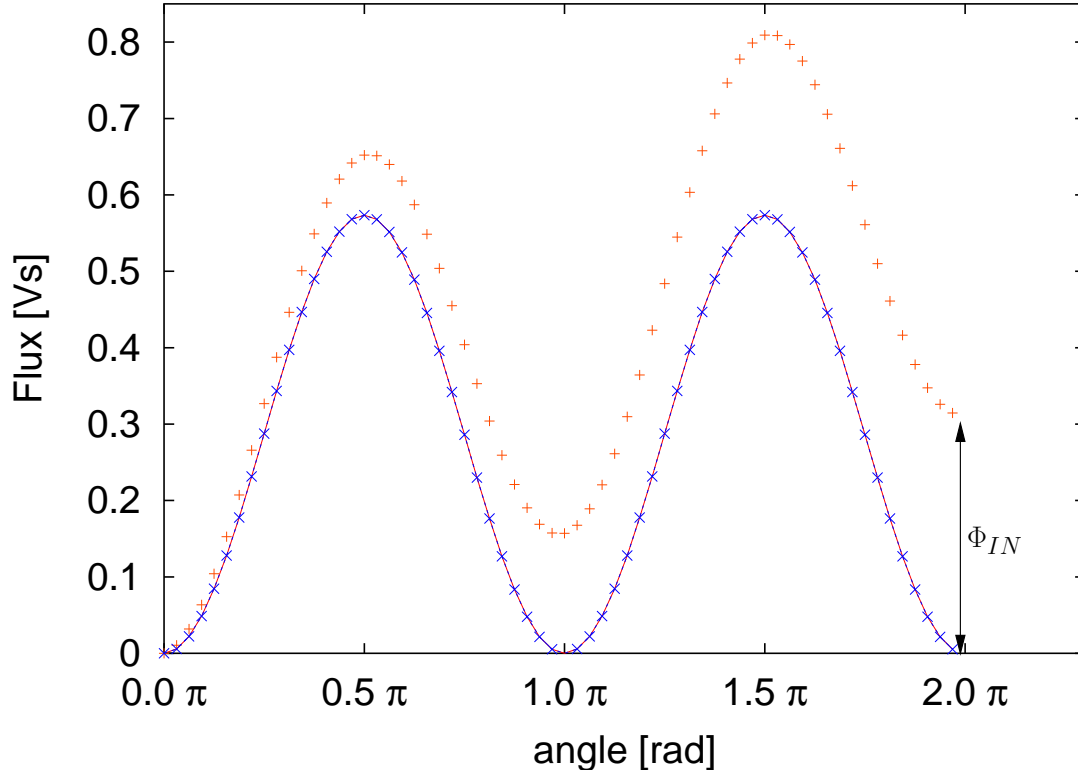


Figure 3.12: Illustration of the offset correction. The measured Flux Φ_I (in Volt Seconds) versus the angle θ (in radian) of the coil is shown. The +’s represent the measurement points, the line the ideal signal and the x’s the corrected signal. By applying the described correction the influence of the offset can be totally removed.

first point artificially to zero. Therefore $F(t = P) = 0$, with P the time necessary for one revolution. The value of that point is identical to $U_0 \cdot P$. The offset is subtracted at each data point using

$$\Phi_{Iic} = \Phi_{Ii} - \frac{U_0 P}{P} t_i = \Phi_{Ii} - \frac{\Phi_{IN}}{P} t_i, \quad (3.4)$$

with Φ_{Ii} the i^{th} point measured at t_i , Φ_{Iic} the i^{th} corrected measurement point, N the last point, and Φ_{IN} the value of the last point.

3.7.2 Calculating the multipoles

The next steps to the final data are:

1. The output of the integrator is Fourier transformed and scaled by the coil sensitivities (see Equations 2.25 and 2.26).

2. The centre of the axis is calculated. For all magnets except the dipole the centre of the field is given by the feed-down (see Equation 3.7).
3. The angle of the main multipole is calculated. The phase of the main multipole is given by

$$\phi = \arctan\left(-\frac{A_m}{B_m}\right). \quad (3.5)$$

The angle of the field is then given by

$$\alpha = \frac{\phi}{m}. \quad (3.6)$$

4. A new coordinate system is established. The axis of the magnetic field is the origin of this system. The y coordinate is parallel to the field direction.
5. All coordinates are transferred to this coordinate system as described by Equation (2.3) and (2.4).

3.8 Axis Measurement

The basic design idea of the Antbear allows the simultaneous measurement of the field quality and the axis. From the magnetic measurement only the offset of the magnetic axis with respect to the rotation axis is known. The transfer of this axis to the fiducials on the cryostat is the main challenge.

The offset of the magnetic axis to the axis of rotation \mathbf{a}_m is given by “feed down” (see Equation 2.39)

$$\mathbf{a}_m = -\frac{R_{Ref}}{m-1} \frac{\mathbf{C}_{m-1}}{\mathbf{C}_m}, \quad (3.7)$$

with C_m the strength of the main multipole m and C_{m-1} the one-order lower multipole; e.g. for the quadrupole $m = 2$. So one calculates \mathbf{a}_m using

$$\mathbf{a}_m = -R_{Ref} \frac{\mathbf{C}_1}{\mathbf{C}_2}. \quad (3.8)$$

The centre of the rotation axis of the axis searching coil is marked by a diaphragm with a diameter of $200 \mu m$ and illuminated by a LED (see Figure 3.5). In the telescope frame the position of an axis point \mathbf{a}_p is given as

$$\mathbf{a}_p = \mathbf{a}_t + \mathbf{a}_m, \quad (3.9)$$

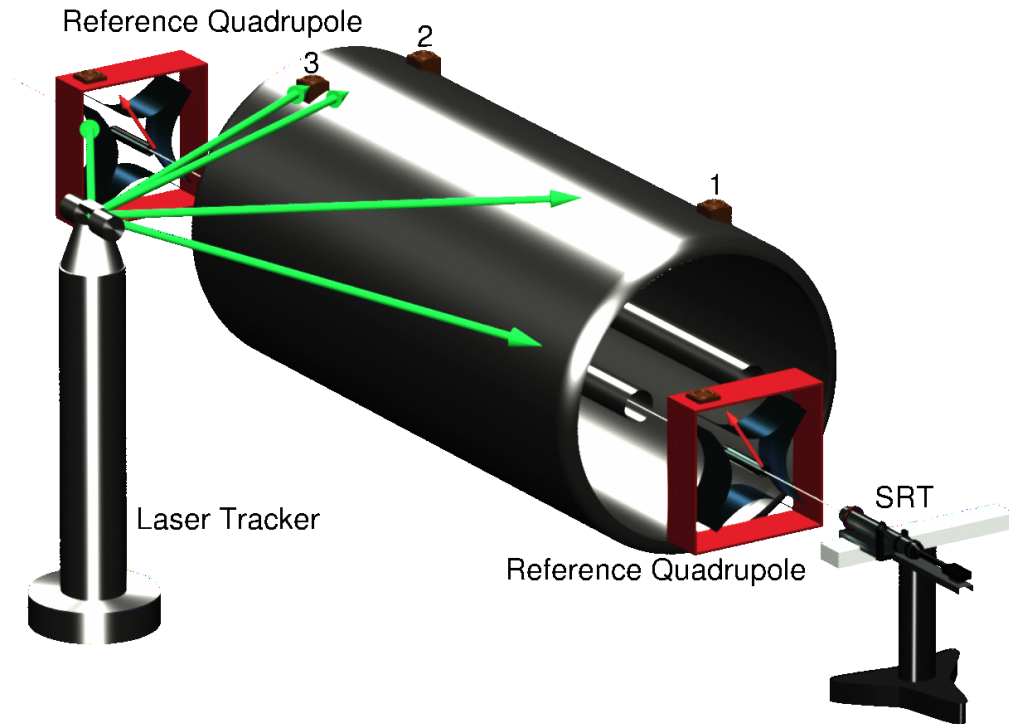


Figure 3.13: Axis measurement equipment. The Laser tracker measures the position of the survey targets (green arrows). The reference quadrupole axis is measured with respect to the fiducials. The reference quadrupole's axes offset to the survey target is measured on a dedicated bench (red arrows). The telescope tracker (SRT) establishes a frame inside the aperture. It is attached to the reference frame using the reference quadrupole axes. The vertical axis of this frame is chosen parallel to gravity.

with \mathbf{a}_t the position of the LED in the telescope frame and \mathbf{a}_m the position of the magnetic axis with respect to the rotating axis. The systematic difference of the diaphragm position to the coil's rotating axis is called wobble. This wobble is calibrated measuring the position of the LED at different angles of the coil.

Inside the reference quadrupoles the axis is measured as well. (See Figure 3.13.) These quadrupoles are equipped with fiducials. The distance of the magnetic centre to the fiducials was measured on a dedicated measurement bench (small arrows). A survey measures the location of the reference quadrupoles with respect to the SSS fiducials (long arrows). Combining these two measurements gives the position of

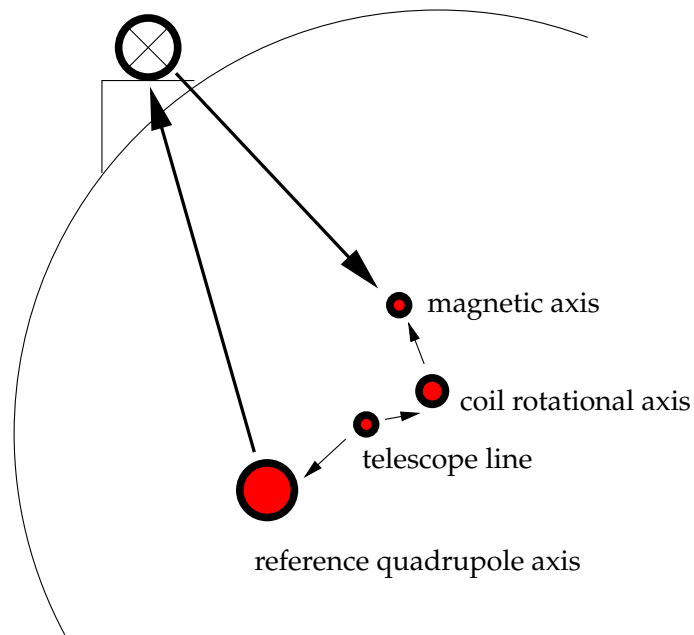


Figure 3.14: Procedure of measuring the axis. In the centre of the axis searching coil a LED is mounted. At each measurement point the telescope measures the position of the LED. The magnetic measurement gives the offset of the magnetic axis to the telescope axis. From these two measurements the location of the axis is known in the telescope frame. The distance between the axes of the reference quadrupoles and their fiducials is measured on a dedicated bench. The reference quadrupole position is measured with respect to the SSS's fiducials. The telescope frame can be attached to the survey frame adding the reference quadrupole fiducials position to the position of the axis.

the reference quadrupole in the survey frame. The telescope frame is referred to these points (see Figure 3.14).

3.8.1 Calculating the rst - values

The users of the magnetic measurement data need the data in the rst - frame. This frame describes the fiducials location with respect to the magnet axes. Its origin is located next to the magnet's centre. Its s -axis is pointing parallel to the magnet's axes. Its t -axis is pointing upwards and r is added in such a way to establish a right handed coordinate system. A description is given in Appendix C.1.

Chapter 4

Qualification of the field measurement

The systems setup has been described in Chapter 3. The principles are not new, the scale and the demands, however, are challenging. For this reason a thorough understanding of the influence of all error sources is necessary. A simulation tool called Truffaldino (named after the main character of [37]), was implemented and is discussed in Section 4.1. The majority of the effects discussed in here can be calculated analytically. All parameters describing the system are gathered in the simulation, which helps to avoid gross errors in the calculation.

A separation was always made between the measurement of the field axis and the other field properties. The later is referred to as “field measurement” or “measurement of the harmonics”. Even if artificial, this distinction is acceptable as the field measurement qualification has to focus on the mechanic and electronic performance of the system, whereas the optical system must be considered as the most critical part of the axis system.

This chapter will focus either on effects, which have not been treated before in the relevant CERN literature, or on effects which have been treated, but for which a more concise description was possible using the aforementioned tool:

- First the type of the error will be described, its effect on the measurement discussed, and then information is presented obtained from either the simulation or the measurement or both.
- Treating the mechanical artefacts one has to solve the coupling of the different errors sources. Using an adapted bucking scheme the different error types of mechanical nature can be distinguished and then treated separately.

- Electromagnetic noise pickup was observed with an oscilloscope. The simulation allows to predict the influence on the field measurement for all considered error sources.

4.1 Truffaldino, the simulation tool

While searching for the source of errors (e.g. electrical noise, imperfection of the coils' rotation, spurious marks in the angular encoder) in rotating coil arrays one can see that different malfunctioning components can produce similar effects. An analytical treatment of nearly any effect is available but generally only ideal magnets containing no other multipole than the main one are considered (i.e. neglecting finite size effects or field errors). Considering more than one effect renders the analysis already more difficult. Previous codes were developed using a purely numerical approach ([38, 39]). This tool (published in [40]), however, uses a semi-numerical approach which calculates the effects of coil imperfections (e.g. coil vibration) analytically. It is discussed in Appendix B in full detail.

4.1.1 Physical Models

In this simulation first principles are used to describe each element's physical properties and its imperfections. The implementation of each element was kept as simple as possible but still so to allow input from experimental experience. As an example the torsional vibrations of mechanical connections are modelled using a series of decaying frequencies and not by trying to calculate the eigen frequencies and those coupled in by the motor. Special partial differential equation solvers exist for this task. Their output can be fed in as decaying frequencies. As it will be shown in Section 4.3.4 such vibrations can be measured and then put into the simulation using the aforementioned series to calculate the effect on the measurement. The model of the different components are described (see also Figure B.1) analytically by the following relations:

1. *The motor* that drives the coil shaft gives the following time dependent angle

$$\theta(t) = \omega t + \sum_{i=1}^N A_i \sin(a_i t + \phi_i), \quad (4.1)$$

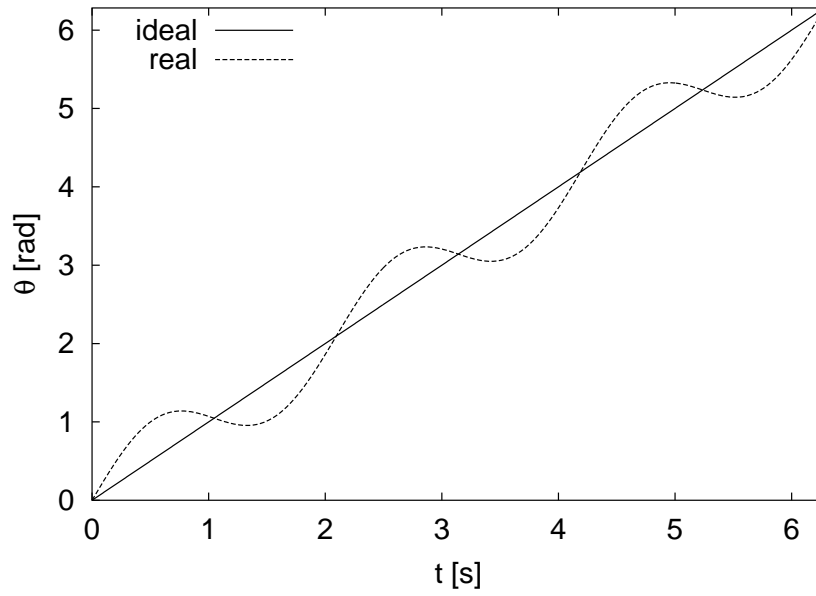


Figure 4.1: Model of the motor. The angle of the motor θ (in radians) is plotted versus time t (in seconds). A motor is seen as ideal motor if it rotates with constant speed. Further it can have eigenfrequencies. This is illustrated here by setting $N = 1$ and $A_i = 3$.

where the first term describes the ideal case and the second term adds a motor vibration with A_i the amplitude of the i^{th} natural frequency of the system of frequency a_i and phase ϕ_i (see also Figure 4.1).

2. *Mechanical connections* that couple the coil to the motor. These connections can vibrate with their natural frequencies which can influence the measurement. This can be modelled as

$$\beta(t) = \theta(t) + \sum_i e^{-f_i t} B_i \sin(b_i t + \psi_i), \quad (4.2)$$

with β the angle of the connection on the coils side, θ the angle on the motor's side, f_i the damping factor, B_i the amplitude of its i^{th} natural frequency b_i with phase ψ_i (see also Figure 4.2). This torsion allows to simulate a system, where coils or coil arrays are connected to each other longitudinally. Such a system is described in [11]. In the simulation only the analysed coil is represented by the rotating coil model, the other coils are treated as mechanical components.

3. *Rotating coils*; their voltage is given by (2.20) or by the ideal case setting $\beta(t) = \omega t$, with ω the nominal speed of the motor. A transversal vibration

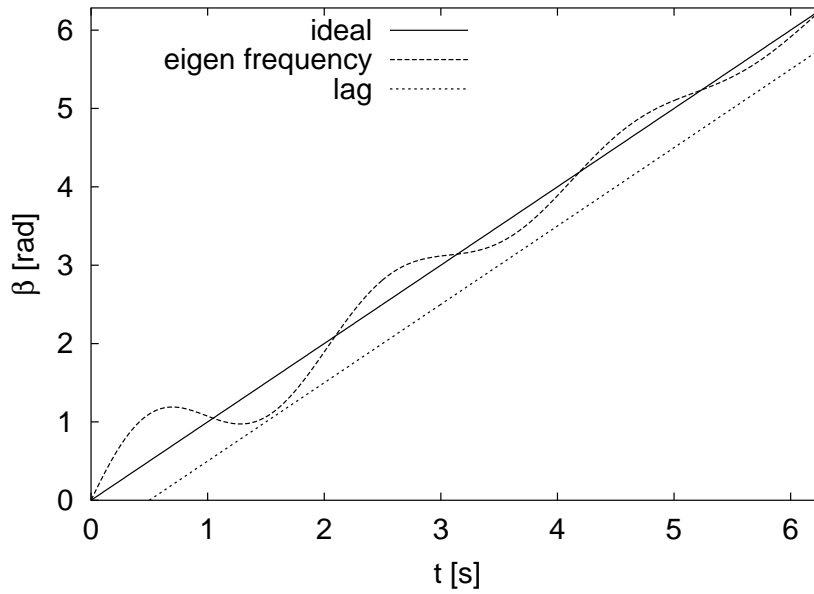


Figure 4.2: Model of the mechanical connections. The angle of the connection β (in radians) versus time t (in seconds) is shown. A connection is seen as ideal if infinitely stiff. Its eigenfrequencies can start to oscillate, but are assumed to be damped in time.

is modelled using Equation (A.15). The *mechanical connections* provide modelling of torsional vibrations of the mechanical elements coupling the coil to the motor and the angular encoder. As main artefact an unstable motion of the coil is considered. This axis deviation $D(\beta)$ is described by a Fourier series

$$D(\beta) = \sum_i D_i \sin(d_i \beta_t + \rho_i), \quad (4.3)$$

with $D_i = x + iy$ the amplitude, d_i the frequency index, and ρ_i the phase of the i^{th} Fourier component. Here the series independent argument is the angle of the coil β , as axis instabilities – e.g. generated by a bad bearing – tend to depend on the angle (see also Figure 4.3). The voltage induced in the coil is then calculated by (see also Section A.1.2)

$$-\frac{d}{dt}\Phi(\beta) = -\frac{d}{dt}Re\left\{ K_n C_n e^{in\beta} + \sum_{p=1}^{n-1} \binom{n-1}{p} K_{n-p} \left[\frac{D(\beta)}{R_{Ref}} \right]^p C_n e^{i(n-p)\beta} \right\}, \quad (4.4)$$

with Φ the flux seen by the coil, and K_n the sensitivity of the coil to the n^{th} multipole C_n .

4. *The angular encoder* that triggers the measurement. In the simulation it is used to determine the appropriate times for the trigger. These events will then be

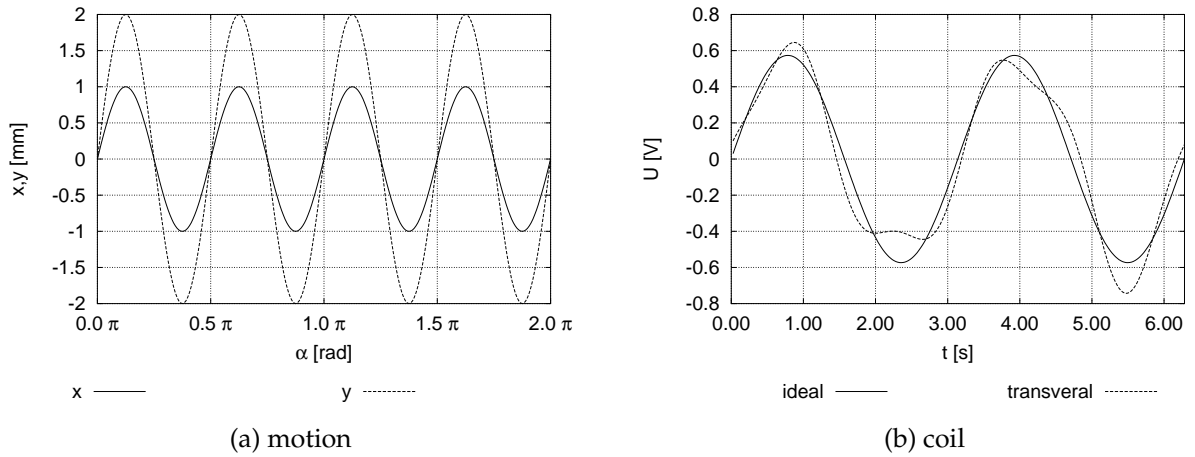


Figure 4.3: Model of the rotating coil. On the right the graph labelled “ideal” shows the output of a coil turning in a pure quadrupole field. An ideal coil will signal the voltage exactly depending on the position. As artefacts the transversal vibration of the coil’s rotation axis is considered. On the left the output of the Fourier series is shown using only one summand with $D_1 = (1 + 2i)10^{-3}[m]$, $d_1 = 4$ and $\rho_1 = 0$. On the right the ideal signal of the sector as well as the signal disturbed by the above movement is shown.

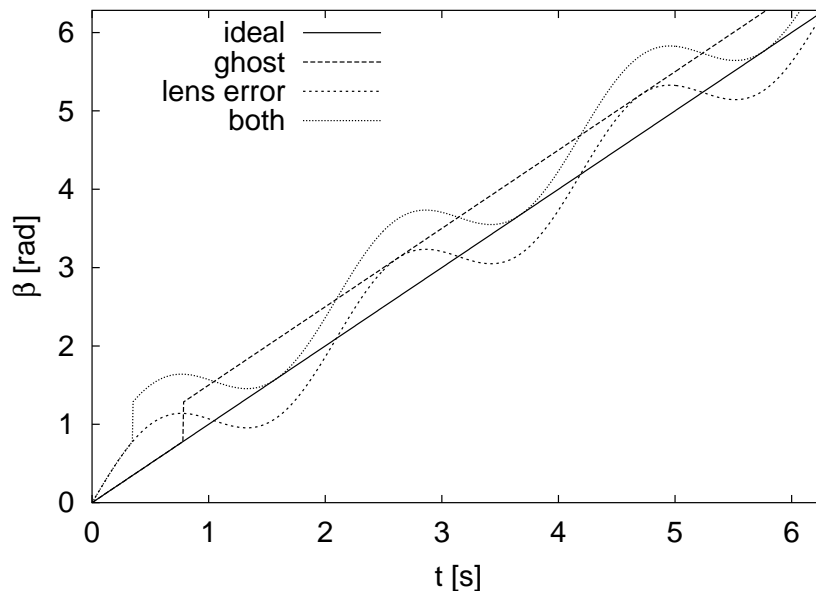


Figure 4.4: Model of the angular encoder. The ideal case is that it triggers exactly at the right moment. However its marks can be misplaced periodically (labelled lens error here), or one mark could be entirely missing (labelled ghost).

used to calculate the flux Φ . As its artefacts periodic errors of the marks and missing marks are considered (see Figure 4.4).

5. *Cables* that transfer signals from source to receiver can pick up electromagnetic noise from the environment. Its output voltage U_O is given by

$$U_O = U_I + U_N, \quad (4.5)$$

with U_I the input voltage and U_N the electromagnetic noise. An example of such noise is given later.

6. *Electronics* consisting of compensation circuitry, preamplifier and integrator. The ideal behaviour is given by

$$\Phi'_{OE} = \int_{t'_0}^{t'_0+P} G_P \sum_i G_{C_i} U_{IC_i} dt, \quad (4.6)$$

where Φ'_{OE} is the integrated voltage, G_P the gain of the preamplifier, U_{IC_i} the input voltage and G_{C_i} the gain of the i^{th} channel of the compensation circuitry. t'_0 is the start time of the measurement, and P the time period needed for one revolution. These devices can have input and output voltage offsets, non linear amplification and a non linear transfer function.

4.1.2 Implementation

In the real system the behaviour of each component is influenced by the attached devices and the surrounding environment. In order to reflect reality as closely as possible an object oriented hierarchy was chosen for the simulation. In Section 4.1.1 the parameters to simulate imperfections were described. These parameters are encapsulated in each module and allow a simple switch between “ideal” and “real” behaviour.

One part of the field quality analysis focuses on the higher order harmonics. These are generally in the order of 100 to 10 ppm of the main field. Therefore the accuracy of the calculation must be in the range of 1 ppm or 6 digits. Equation (2.20) shows that the contribution of each harmonic is summed up in the time domain. This means that the contribution to the voltage of any other multipole than the main starts at the fourth digit of the main harmonic. The accuracy requirements can be fulfilled calculating with a 15 digits' accuracy.

4.2 Electrical effects

In this section I will discuss artefacts of electrical nature. Error sources due to imperfections of the measurement electronics are described next to effects generated by the power supply. The experimental detection of the effects discussed in here is the same despite their different origin. An oscilloscope is connected to the measuring cable outputs and its signal is analysed.

4.2.1 Preamplifier offset

The goal of the magnetic measurement is to describe the magnetic field in the multipole representation. Integrating and angular triggering renders a signal less dependent on the coil's rotation speed [27, 12]. In Section 3.7 it was shown, that the harmonics are obtained by a Fourier analysis of the signal. An offset of the preamplifiers yields a linear drift of the integrator output signal given by

$$\int_0^t a \, dt' = a \cdot t. \quad (4.7)$$

In Section 3.7.1 it was shown that the last measurement point is equal to $a \cdot t$. Following the outlined analysis a constant offset can be subtracted. This whole procedure works perfectly for a DC offset.

Here the influence of electrical noise on this correction is studied. Pick up of electrical noise can effect the last point and the procedure given in Section 3.7.1 is not valid any more. As the electronics would not allow non-continuous signals, any integrator input can be expressed as a Fourier series

$$U_I(t) = \sum_i a_i \sin(b_i t + \phi_i), \quad (4.8)$$

with U_I the input voltage of the integrator, a_i the amplitude, b_i the frequency and ϕ_i the phase of the i^{th} component. By integration one gets

$$\int_0^P \sum_i a_i \sin(b_i t + \phi_i) dt = \sum_i \int_0^P a_i \sin(b_i t + \phi_i) dt = - \sum_i \frac{a_i}{b_i} \cos(b_i t + \phi_i) \Big|_0^P. \quad (4.9)$$

Using the periodicity of the sinus one can calculate the last expression to

$$\begin{aligned} & \sum_i \frac{a_i}{b_i} \cos(b_i t + \phi_i) \Big|_0^P = \\ & \underbrace{\sum_i \frac{a_i}{b_i} \cos(b_i t + \phi_i) \Big|_0^{2k\pi \leq P}}_0 + \sum_i \frac{a_i}{b_i} \cos(b_i t + \phi_i) \Big|_{2k\pi \leq P}^P \\ & k \in \mathcal{N} \quad \wedge \quad 2k\pi < P \quad \wedge \quad 2(k+1)\pi > P, \end{aligned} \quad (4.10)$$

with \mathcal{N} the natural numbers. Only incomplete periods of the noise debase the measurement of the last point. Due to the integration the amplitudes are divided by the frequency, and therefore the integration decreases the noise. Further it should be noticed that the integrator works similar to a high-pass filter. Therefore the standard correction method is still applicable in the presence of normally experienced noise. In the following one example is treated. Observing a new noise spectrum necessitates a new treatment to qualify the influences.

4.2.2 Low frequency ripples

Beside the signal treating electronic the power supply can affect the measurement.

For the current ripple discussion the data and graphics shown here were taken on a bench dedicated to dipole measurement, because the effect was more clearly visible there due to a bad power supply. After the demonstration it will be concluded what effect is expected on the quadrupole bench. A power supply was to be qualified for the aforementioned bench. When connecting an oscilloscope to the coil's output some oddness was detected in the rotating coils signal.

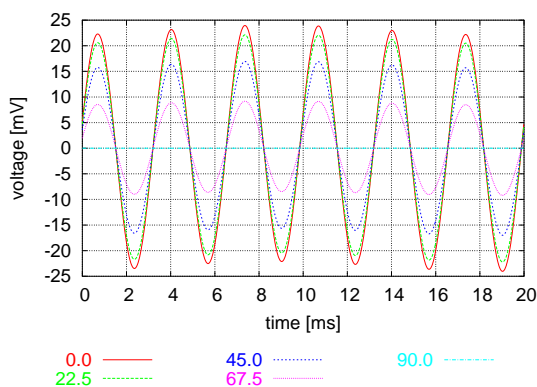


Figure 4.5: Scope measurement with a stationary coil

The voltage output of the coil was measured using an oscilloscope keeping the coil stable. Then the coil was turned by 15 degrees. Again the measurement was repeated. This was done up to 90 degrees. In Figure 4.5 one can see that the induced voltage steadily decreases. The frequencies chosen for modelling are 300 Hz (main frequency) and 50 Hz (“beating frequency”).

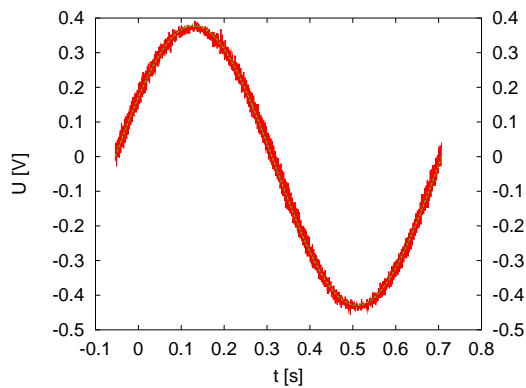


Figure 4.6: Scope measurement during coil's rotation

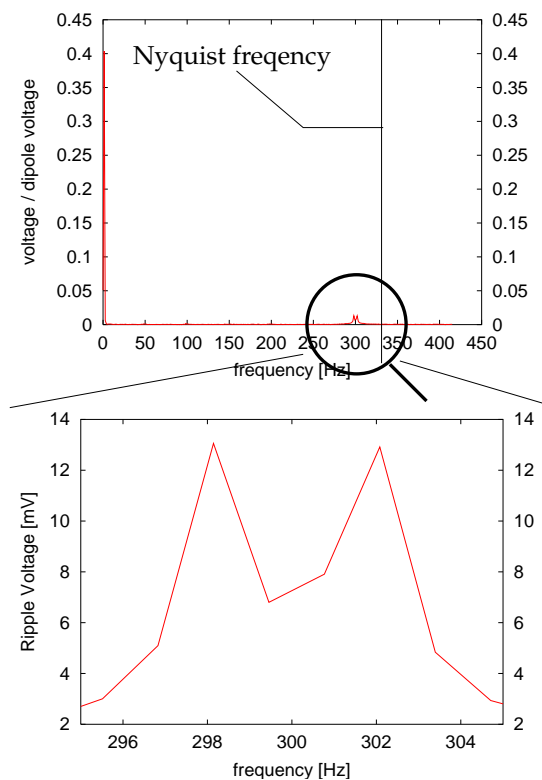


Figure 4.7: Spectrum of the Scope measurement

Now a measurement was made with the oscilloscope while the coil was rotating (see Figure 4.6). The solid line indicates the ideal undisturbed signal generated by a dipole. From a glance one would assume that just random noise is overlaying the ideal signal.

The above measured signal was Fourier transformed (see Figure 4.7). The line “Nyquist frequency” denotes the maximally resolvable frequency of the rotating coil system. Note the small peak near to the line labelled Nyquist frequency, which is generated by the ripple with an amplitude of approximately 5% of the dipole signal. 250 data points are read out during one revolution of the coil. As the coil needs 0.76 seconds for one revolution, the maximally resolvable frequency is $250/0.76/2 \approx 164 \text{ Hz}$. All higher frequencies are folded back. So frequencies around 328 Hz are folded back to the low frequencies area, which also contains the multipole information.

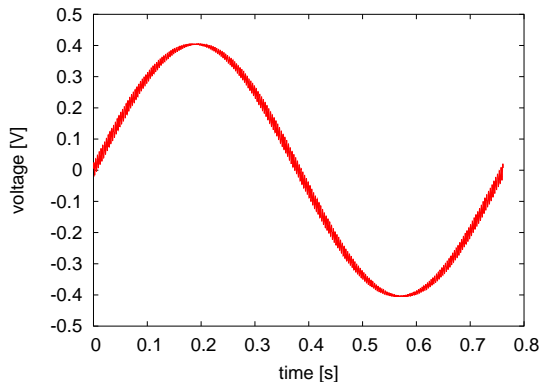


Figure 4.8: Calculation of the sector output

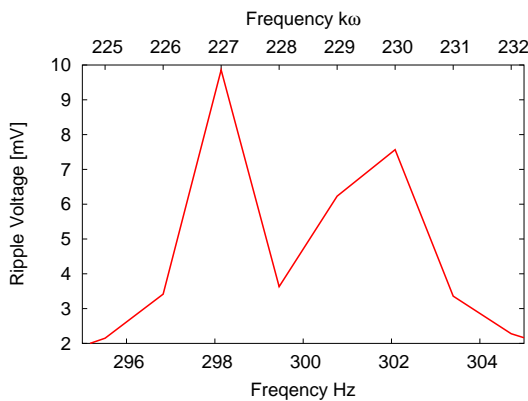


Figure 4.9: Spectrum of the calculation. The coefficients are shown versus the frequency (in Hertz). The scale above the figure gives the multiples of the coils rotation frequency.

To verify that this artefact is generated by the ripple, the whole system was simulated assuming a power supply with a ripple of 5 mA at 300 Hz and 1.2 mA at 50 Hz with a nominal current of 25 A . In Figure 4.8 the simulated output of the voltage induced in the coil is shown. Comparing this figure to Figure 4.5 one can note a remarkable difference. Due to the selection of the frequencies only the ripple influence is left. Note that at the maxima of the voltage the ripple induced signal is zero as the flux change seen by the coil is zero there (see Equation 2.20). So the ripple signal can be seen as two frequencies around 300 Hz with a beating frequency equal to the coil's rotation frequency.

The signal of Figure 4.8 was Fourier transformed. The derived spectrum is similar to the one shown in Figure 4.7. In Figure 4.9 the peak is magnified. As the coil's rotating frequency is not an exact integer, each coefficient is contributing to more than one bin.

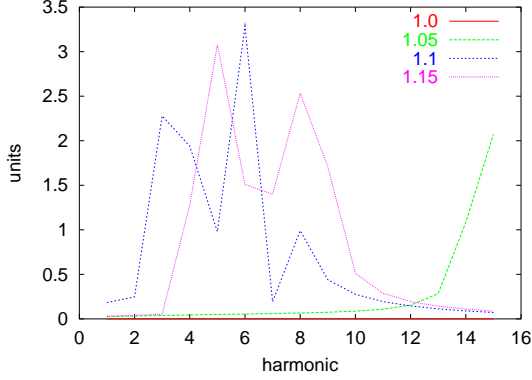


Figure 4.10: Dependence of the influence on the speed.

The considered system can resolve only 250 readings during one revolution. As aforementioned this results in a Nyquist frequency of 164 Hz . All frequencies near this frequency and its multiples can be folded into the low frequency range overlapping with the information of the magnet multipoles. In Figure 4.10 the effect is presented for different speeds. The motor speed at which the measurement data were taken was set to 1.0. One can see, that a small change ($\approx 10\%$) in the speed can result in a spurious main field measurement. The graph labelled 1.15 was already “folded” once more than the graph labelled 1.1.

The current ripple can affect the measurement of all harmonics, but for the higher harmonics the effect is smaller by the bucking factor. The amplitude of the voltage induced by the ripple (see Figure 4.5 and Figure 4.6) was $\approx 25\text{ mV}$ on top of the dipole induced signal of $\approx 400\text{ mV}$. The harmonics are obtained from the output of the integrator. Therefore the strength of the normalised harmonic c_{RI} induced by the ripple is calculated as

$$c_{RI}(t) = \int U_{RI} \sin(\omega_{RI}t' + \phi) dt' = \frac{U_{RI}}{\omega_{RI}} (1 - \cos(\omega_{RI}t + \phi)), \quad (4.11)$$

with U_{RI} the ripple voltage, ω_r cycling frequency and ϕ the phase of the ripple. The main harmonic strength can be estimated similarly. The harmonics are often given in units, i.e. with respect to the strength of the main harmonic (see Equation 2.2). Therefore the absolute value of the normalised harmonic $|c_{RI}|$ induced by the ripple can be calculated as

$$|c_{RI}| = \frac{U_{RI}}{U_m} \frac{\omega_m}{\omega_{RI}} = \frac{30}{400} \frac{1.4 \cdot 2\pi}{300 \cdot 2\pi} \approx 3.5 \text{ units}, \quad (4.12)$$

with U_m the voltage induced by the dipole, and ω_m the rotating frequency of the coil. 1.5 units are acceptable (see Table 1.1), therefore the induced voltage must not be larger than two percent of the maximum voltage. The ripple induced coil voltage

is the derivative of the flux Φ with respect to time t (see Equation 2.17)

$$U_{RI}(t) = -\frac{d\Phi}{dt}. \quad (4.13)$$

Assuming a pure dipole field the voltage is given as

$$\begin{aligned} U_{RI}(t) &\approx -\frac{d}{dt} \text{Re} [\mathbf{K}_1 \mathbf{C}_1 \exp(i\omega_{RI}t)] \\ &= -\frac{d}{dt} \text{Re} [\mathbf{K}_1 \mathbf{c}_{\text{mag}} I_{RI} \exp(i\omega_{RI}t)] \\ &= -\omega_{RI} \text{Re} [\mathbf{K}_1 \mathbf{c}_{\text{mag}} I_{RI} \exp(-i\omega_{RI}t)] , \end{aligned} \quad (4.14)$$

with I_{RI} the ripple current, ω_{RI} the cycle frequency of the ripple, and \mathbf{c}_{mag} the magnet's transfer constant. As for the voltage the current has to be compared to the main current. To estimate the current one has to consider the effect of the time dependent and the effect of the time independent part of the field. To guarantee the precision of $1.5 \cdot 10^{-4}$ one has to demand that the time dependent part is smaller by this factor than the time independent part

$$\frac{\omega_{RI} c_{\text{mag}} I_{RI}}{c_{\text{mag}} I_{\text{mag}}} = 300 \cdot 2\pi \frac{I_{RI}}{I_{\text{mag}}} < 1.5 \cdot 10^{-4}. \quad (4.15)$$

Thus the acceptable ripple current is calculated to 0.1 ppm.

All numbers above were given for the dipole bench and power supply. As one can see even such a high frequency can influence the measurement. The limits however are also valid for the quadrupole power supply. A single frequency yields exactly one spurious harmonic, if the frequency coincides with a frequency of an induced multipole. If not, it contributes to the neighbouring multipole frequencies as well. The quadrupole supply induced ripple voltage was measured to 0.15 mV at 3 Hz. If the quadrupole's coil rotates with a frequency of $\frac{3}{2}$ Hz the quadrupole induced signal has a frequency of 3 Hz and the ripple would interfere with its signal. The voltage induced by the main field is 0.3 V at injection level. Using Equation (4.12) and $U_{RI} = 0.15 \text{ mV}$, $\omega_{RI} = 3 \text{ Hz}$, $U_m = .3 \text{ V}$ and $\omega_m = \frac{3}{2}$ the ripple's effect is calculated to 2.5 units. So starting from the double injection current the magnet induces enough voltage in the measurement coil to allow the measurement of the main field with an accuracy of $1.5 \cdot 10^{-4}$.

The influence of the ripple is linked to the magnet's main field and therefore its effect on the measurement of the main harmonic was given here. In the compensated system it is smaller by the compensation factor.

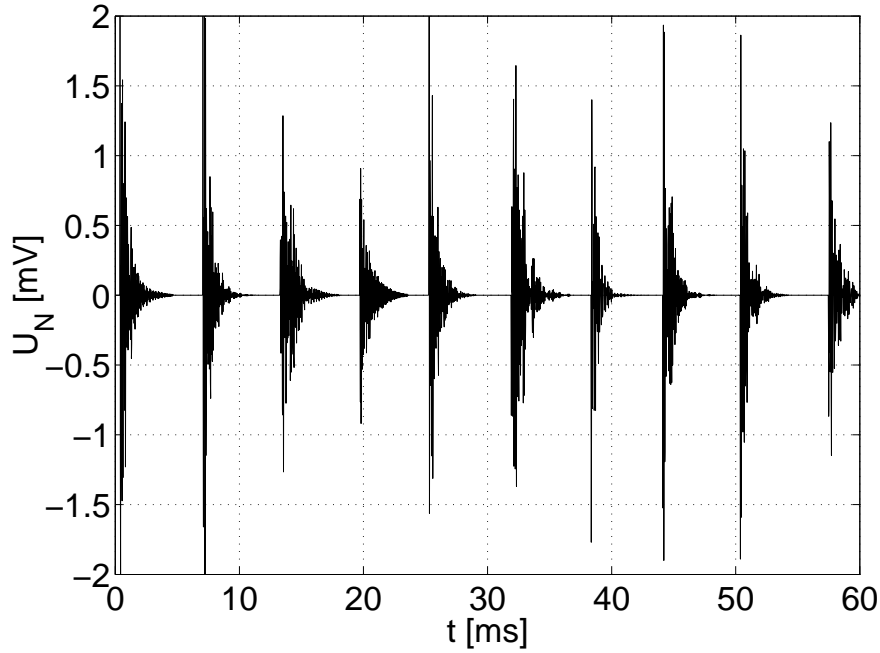


Figure 4.11: Model of the noise in the cable. The induced voltage (in millivolts) is plotted versus time (in milliseconds). One can see the spacing of approximately 600 Hz .

4.2.3 Medium frequency electrical noise

Many different types of equipment are needed to perform the magnetic measurement in cold condition. Most equipment is based on electricity and emits electromagnetic noise. Here the influence of a thyristor bench based power supply is treated. These thyristors typically work at multiples of the power frequency cutting the current at some phase. Due to the significant inductive component of the load (magnet) in the circuit one expects electrical noise transmitted to the environment when one thyristor cuts the current to zero.

To identify the influence of this noise on the system an oscilloscope was plugged to the coil cables. The displayed signal was modelled using the following equation (see also Figure 4.11)

$$U_N(t) = \sum_{i=1}^N q_i e^{-r_i(t-t_{0i})} \sin[s_i(t-t_{0i})]. \quad (4.16)$$

U_N is the noise induced voltage for one peak. N is the number of frequencies contributing to the peak set to 10, s_i is the frequency set randomly between 50 and 100 kHz , q_i the amplitude of the i^{th} frequency set uniformly randomly between $\pm q_{\max}$ with q_{\max} the maximum amplitude, r_i is the decay of the frequency set uniform randomly between $3 \cdot 10^3$ and $1 \cdot 10^3\text{ s}^{-1}$ and t_{0i} is the start time of the peak set

Table 4.1: Influence of the electrical noise on the harmonics. The induced fake normalised harmonics $C_n/C_2 \cdot 10^4$ (in Tesla at the reference radius) is given versus the maximum voltage q_{max} (in millivolts) of the peak.

voltage q_{max} [mV]	0.1	1.0	10.0
$[C_n/C_2 \cdot 10^4] \ C_2 = 1.5 \ T @ \ R_{Ref}$	10^{-4}	10^{-3}	10^{-2}
$[C_n/C_2 \cdot 10^4] \ C_2 = 0.2 \ T @ \ R_{Ref}$	$7 \cdot 10^{-4}$	$7 \cdot 10^{-3}$	$7 \cdot 10^{-2}$

so that one peak would start every millisecond with a uniform random variation of 1 millisecond.

In the simulation it was assumed that the noise effects the signal after the analogue compensation, where the signal is smallest and therefore the signal change is biggest. Based on the data from the simulation the influence of this noise is given in Table 4.1.

The influence on the harmonics is correlated with the maximum amplitude of the noise and shows roughly the same amplitude for all harmonics. As Fourier series need the whole spectrum of frequencies to describe discontinuities as shown in Figure 4.11, the series contains low frequencies as well. Due to aliasing [41] – the maximal resolvable frequency in the system is $125 \omega / 2\pi$ – these frequencies are amplified and therefore an influence on the harmonic measurement is visible. However in a realistic range (1 to 5 mV) the effect on the harmonics is still within the limits.

4.2.4 Difference between current ripple and voltage noise

The effect of flux ripple and voltage noise can be seen when a oscilloscope is connected to the coil's cable. The screen of the oscilloscope will look something like the graph shown in Figure 4.5. The following tests can be made to distinguish the two: The coil is left stationary and the induced voltage is measured. An amplitude varying with the angle, as shown in Figure 4.6, indicates a flux ripple. A Fourier transform should be applied to the signal during the coil's turn as a second test. A double peak separated by the main's harmonic frequency should be visible (see Figure 4.9). As the flux is proportional to the area, and the inductance proportional to the flux (see Equation 2.13 and 2.17) the effect should disappear if the coil is disconnected from its cables and the signal is observed in a closed loop.

The environmental noise shown in the above section generates a lot of frequencies. A generator of one single frequency would generate a scope signal similar

to the one generated by the flux ripple. In the case of superconducting accelerator magnets the cryostat in combination with the anti-cryostat shields the electromagnetic noise sufficiently. Therefore it is less likely that the coil itself picks up the noise than the cables connecting the coil to the electronic. Again disconnecting the coil and closing the loop the signal of the environmental noise should be detectable.

So if one sees a signal that could be linked to environmental noise or flux ripple, one should take data, after disconnecting the coil. If this signal is still visible it is related to environmental noise, if it disappears it could be related to flux ripple.

4.3 Mechanical effects

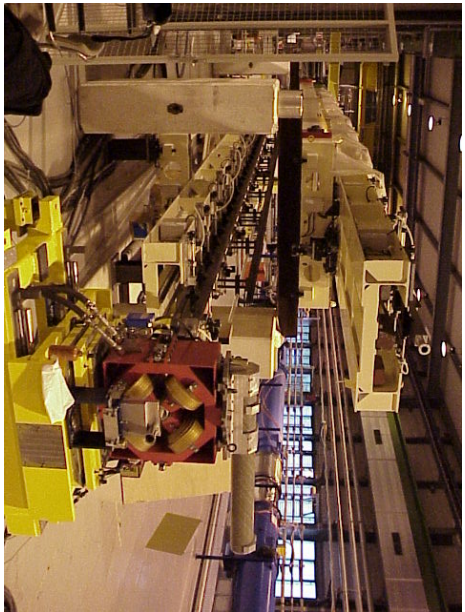
Besides the electrical equipment the mechanical equipment affects the quality of the measurement. In Chapter 3 the great size of the setup is visible. The shaft has a length of 13 m, over its length a mechanical angular stiffness of 1 mrad has to be provided. The coil rotation must be controlled with a quality of a few micrometers. In this section the steps which were performed for the mechanical assessment are described together with their results. Possible artefacts are:

- angular twist of the shaft,
- torsional vibrations of the shaft and
- transversal vibrations of the coil.

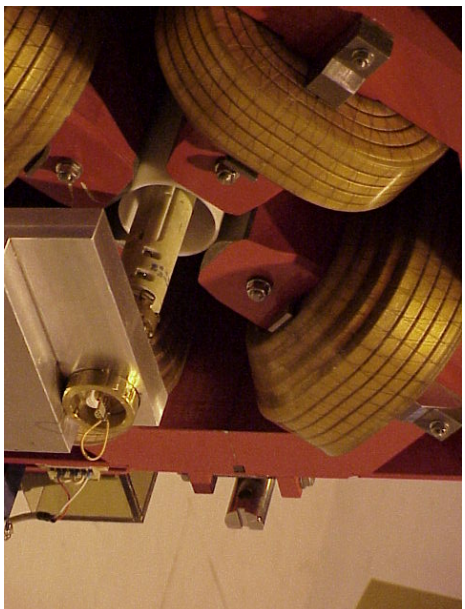
The estimation of the angular lag is straightforward. The mean value of a clockwise and a anti-clockwise rotation yields the real angle, the difference allows to estimate the lag. The torsional vibrations of the shaft and the transversal vibrations of the coil array are more difficult to measure. In the following a shaker test is explained, which allowed to verify that the simulation can correctly calculate the generated harmonics. The next step is then to show that the vibrations induced by the shaker can be measured. The comparison of the measurement to the measured shaker movement gave confidence in the procedure, and therefore it was applied to the signals measured with the standard measurement setup. Thus, the torsional vibrations of the shaft and the transversal vibrations of the coil were measured and found to be acceptable. In the following the whole procedure is explained in full detail.

4.3.1 The shaker test

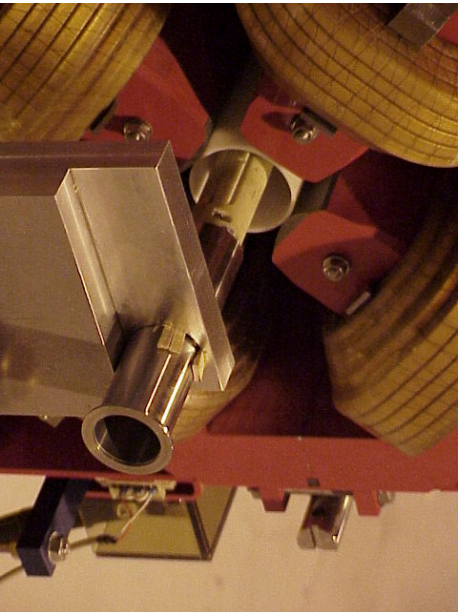
The first step toward the validation of the mechanical qualification was performed by the shaker test, which enforces a transversal vibration of the coil. The equations describing the signal of a lateral oscillating coil were given in Section 2.5.1. Four cylindric cams were machined out at one end of a cylinder, each with a height of 1 mm (see Figure 4.12). This cylinder was mounted on to the end of the harmonic coil (see Figure 4.13) and put through an oval hole made in the holder forming the guidance. The cams were sliding on a horizontal surface of the holder. Using lubricating oil the shaker formed a sliding contact bearing with a known imperfection.



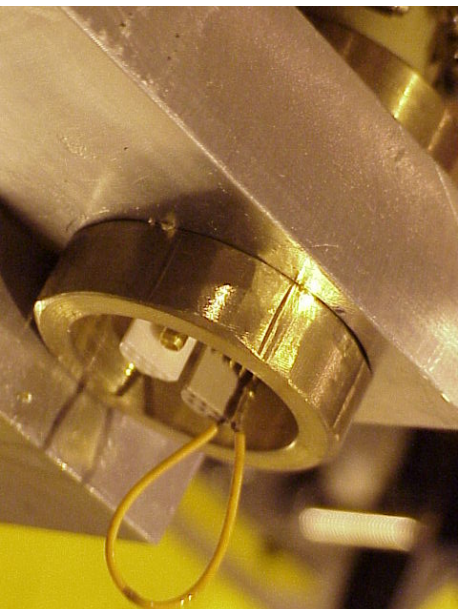
(a) Setup



(b) Shaker



(c) Fixation of the additional tube



(d) Shaker detail

Figure 4.12: Photos of the experimental setup for the shaker test. The left part shows the ball bearing test, the right part the shaker test. One can see the Antbear and a reference quadrupole. On the viewers side the shaker support and the shaker are mounted. For the bearing test a normal metal tube was inserted in the elliptic hole and fixed by wooden wedges.

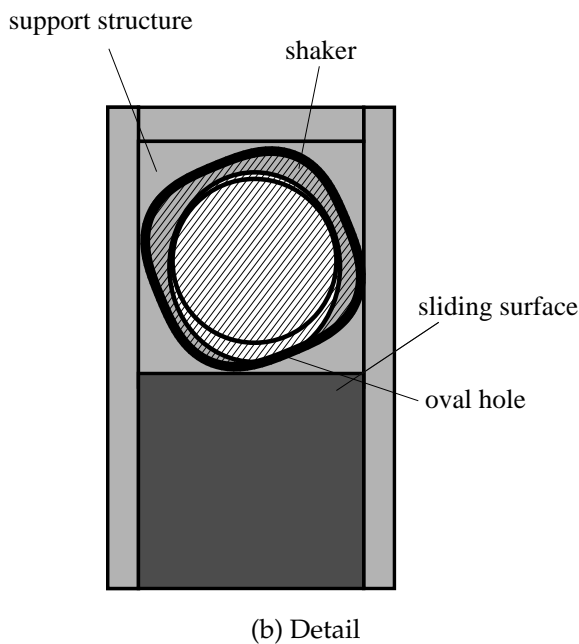
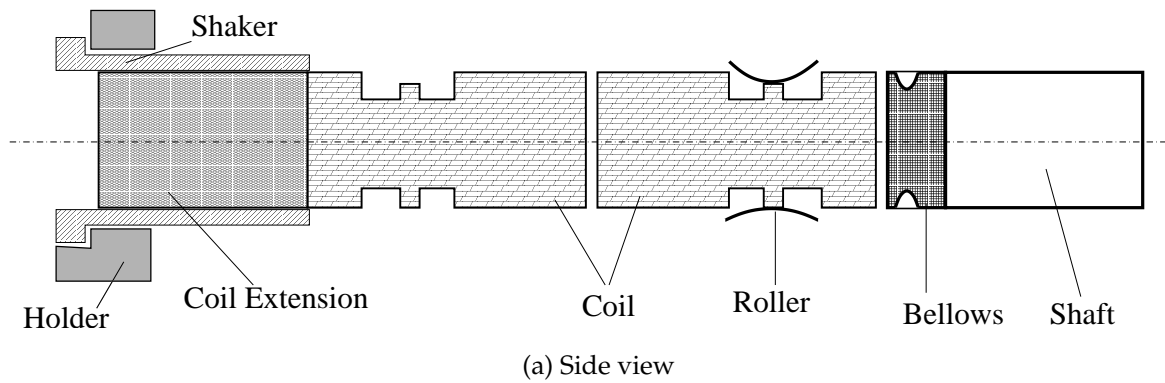


Figure 4.13: Sketch of the eccentric. The eccentric is mounted on one end of the coil array (a). The eccentric disk itself slides on a metal plate. Lubricant controls the friction. The eccentric has 4 cams (b) inducing a spurious sextupole and decapole.

During each revolution the coil was lifted vertically four times by 1 mm at one end due to the cams. On the other end of the coil the ball bearing kept the coil's lateral position stable.

In Section 2.6 the analytical expressions for the spurious harmonics generated by mechanical imperfections in a pure quadrupole field were shown. It was pointed out there that the magnitudes of the spurious harmonics generated by transversal vibrations depend on K_1 , the sensitivity of the coil array to the dipole. Those gen-

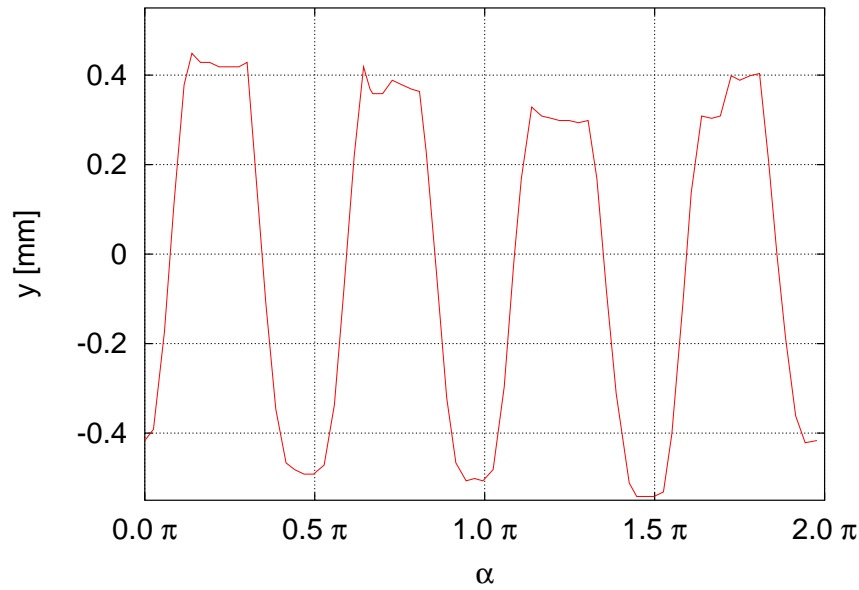


Figure 4.14: Shape of the shaker measured using a dial gauge. The angle α of the coil (displayed by the angular encoder) versus the reading of the gauge (y in millimetre) is displayed.

erated by torsional vibrations of the coil array with respect to the angular encoder depend on K_2 , the sensitivity of the coil array to the quadrupole. Therefore four measurements were performed using different compensation schemes [42, 43]:

1. The absolute measurement using coil A . This shows the influence of all mechanical effects on the measurement.
2. The quadrupole and dipole compensated measurement using the coil array $A - B - C + D$. From this measurement the harmonics of the magnet were derived.
3. The dipole compensated measurement using the coil array $A - C$. Subtracting the multipoles measured by the compensated system one gets the spurious harmonics caused by torsional vibrations.
4. The pure quadrupole compensated measurement using the coil array $A - B + D$ yielding the harmonics due to the transversal vibrations.

Further a dial gauge was attached to the cylindrical end of the coil and the movement of the coil at the shaker end was recorded (see Figure 4.14). As the magnet is shorter than the coil, and the coil was only shaken at one end, this movement was

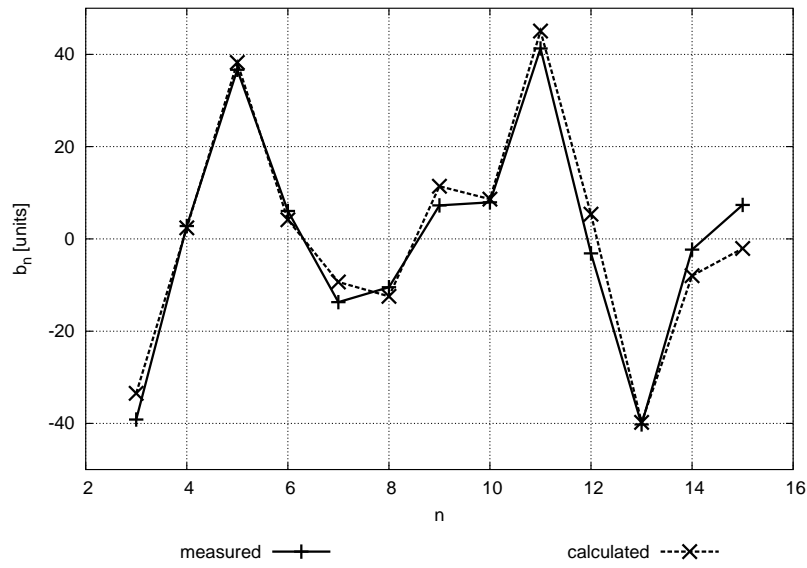
scaled for a coil of the length of the magnet and shaken parallel to its axis. This movement was Fourier transformed and used to describe the coil's irregular motion to the simulation. Using the simulation the effect on the measurement was calculated taking all harmonics into account (see Equation A.15). The simulation assumes two dimensional fields, which means that it will only yield correct results, if the field of the magnet has the same property along the axis of the coil. As the coil is longer than the magnet, a scaling was necessary to take the magnet length into account. In this measurement the interest is put on the generated spurious harmonic amplitude as compared to the main field strength (see Equation 2.43 and 2.51). Normalised harmonics possess this characteristics (see Equation 2.2). Thus, using normalised harmonics the higher order harmonics are scaled to the strength of the magnet and therefore the higher order harmonics of the simulation are comparable to the higher order harmonics of the measurement. In Figure 4.15 one can see that the calculated and measured harmonics match nicely. To estimate the precision of the magnetic field measurement the difference of the forward harmonics to the backward harmonics was calculated. It was found that they varied on the order of 5 units. One can see that the shape of the two curves is identical but they differ by 15% in size. As the bellows is not connected directly at the ball bearing (see Figure 4.13(a)) the shaft end has to follow a counter movement. All the ball bearing holders are spring loaded, and therefore the ball bearing performed some counter movement. The radial uncertainty of 15% is calculated to $\approx 30 \mu m$ in radius, and therefore the result is acceptable.

4.3.2 Shaker induced transversal vibrations of the coil

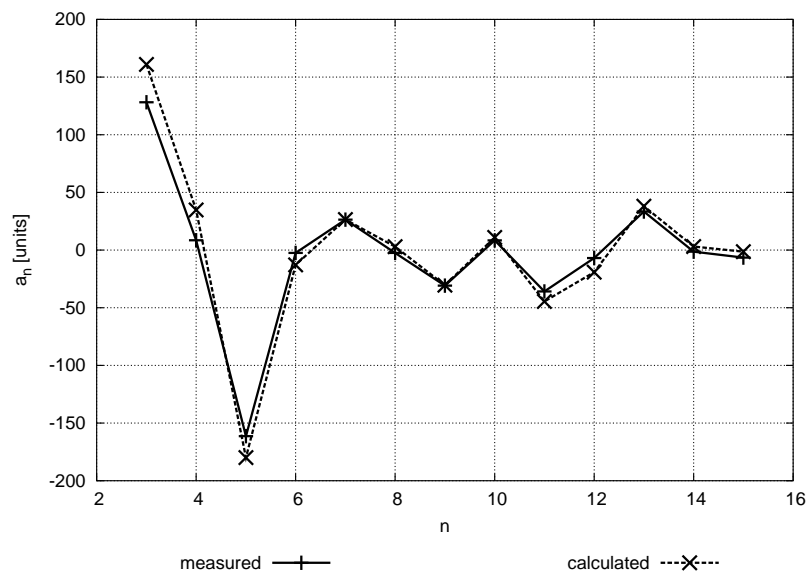
In the previous section it was shown that the generated spurious harmonics can be calculated. In a quadrupole field the spurious harmonics $C_{p\pm 1}^s$ generated by one vibration mode $d \sin(p\theta)$ are given as (see Equation (2.43)) with d the amplitude of the vibration mode

$$\begin{aligned} C_{p+1}^s &\propto \frac{d K_1}{K_{p+1}} \\ C_{p-1}^s &\propto \frac{d K_1}{K_{p-1}} \end{aligned} \quad (4.17)$$

Please note that one vibration mode generates two harmonics. To reverse the point one has to take the spurious harmonic spectrum and search for the possible sources. One can see from the above formulae that the influence of the odd and even vibrations are decoupled. The even harmonics are only generated by the odd vibrations



(a) normal



(b) skew

Figure 4.15: Spurious harmonics induced by the shaker. The normalised harmonics were measured bucking the quadrupole and calculated using the measured movement. In the above figure the results are shown for the normalised b_n and the skew harmonics a_n versus the multipole n . The spurious sextupole and decapole are nicely visible. The precision of the measured curves is ≈ 5 units (difference of the harmonic rotation between the ones measured, when the coil was turning in one direction and the ones when the coil was turning in the opposite direction).

and vice versa.

In the bucking scheme $A - B + D$ only the quadrupole sensitivity is decreased. As the dipole sensitivity is still large the measured higher order harmonics are dominated by the spurious harmonics due to lateral vibrations. Subtracting the magnet's higher order harmonics measured with the standard setup only the spurious harmonics remain, which are now called vibrational harmonics. All calculations presented in this chapter were based on these harmonics. Due to the quadrupole compensation only the harmonics with a higher order than the main harmonic are meaningful. Therefore the lowest resolvable vibration mode is $p = 4$. The highest used harmonic of the magnet's spectrum was $n = 15$. For calculating the vibrations the following assumptions were made:

1. The spurious sextupole is only generated by the vibration with a frequency index $p = 4$.
2. The spurious octupole is only generated by the vibration with a frequency index $p = 5$.
3. The spurious multipole at $n = 14$ is only generated by the vibration with a frequency index $p = 13$.
4. The spurious multipole at $n = 15$ is only generated by the vibration with a frequency index $p = 14$.

These assumptions are necessary to render the problem calculable as the values of the spurious dipole and quadrupole are not available. In Figure 4.15 one can see that the harmonics of $n = 14, 15$ are not larger than the precision of the measurement (5 units). Therefore these assumptions are acceptable.

The calculation was performed following these steps:

1. Using the information of the spurious sextupole the corresponding deviation for the index $p = 4$ was calculated.
2. Using this deviation the spurious decapole was calculated.
3. From the difference of the measured spurious decapole and the calculated one the deviation for the index $p = 6$ was calculated.
4. Point two and three were repeated similarly for all higher harmonics up to harmonic 15.

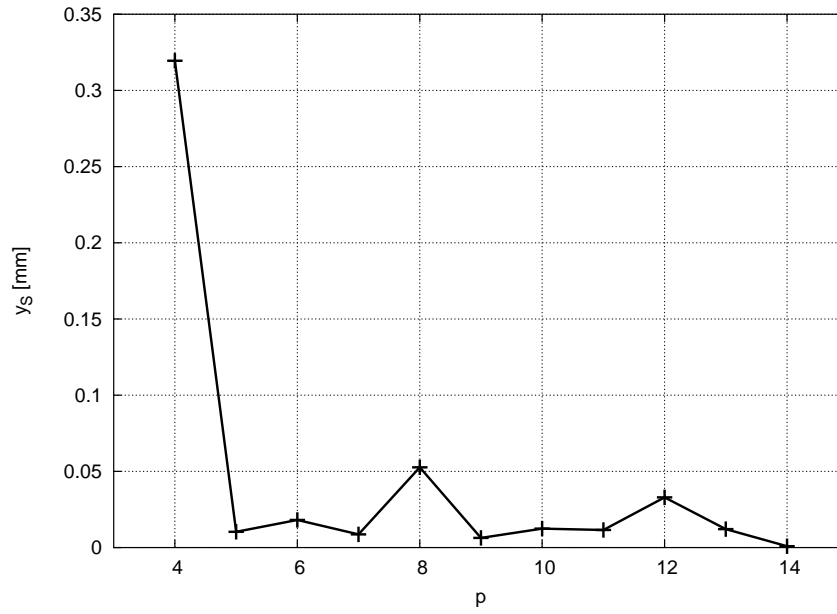


Figure 4.16: Calculation of the lateral vibration amplitudes from the measurement using the shaker. The absolute amplitude of the vibration y_s (in millimetre) induced by the shaker is plotted versus the index of the rotation frequency p . The biggest one is at index $p = 4$, as the shaker had four cams. Its amplitude coincides nicely with the properly scaled shaker strength.

This procedure was also performed starting from harmonic 15. The mean of the two calculations was considered as the measured transversal even vibrations. Starting from the octupole the odd measured vibrations were calculated in a similar fashion. The result of this calculation is visible in Figure 4.16. The mechanically measured and scaled amplitude of 0.32 mm matches nicely the magnetically measured amplitude.

4.3.3 Transversal vibrations of the coil in the measurement system

The above results convinced us that the lateral vibrations can be calculated following the aforementioned procedure. The same measurement as described above was also performed with the ball bearing instead of the shaker and the same calculation was applied to that data. In Figure 4.17 the result is shown. The highest measured amplitudes are in the order of $2\text{ }\mu\text{m}$. In Table 1.1 it was stated that the absolute signal has to be measured with an accuracy of $1.5 \cdot 10^{-4}$. Using Equation (2.43) the maximal acceptable lateral vibration amplitude for $p = 1, 3$ is equal to $10\text{ }\mu\text{m}$. The spectrum coefficients of the “ball bearing measurement” are all below $2.5\text{ }\mu\text{m}$. Even if the co-

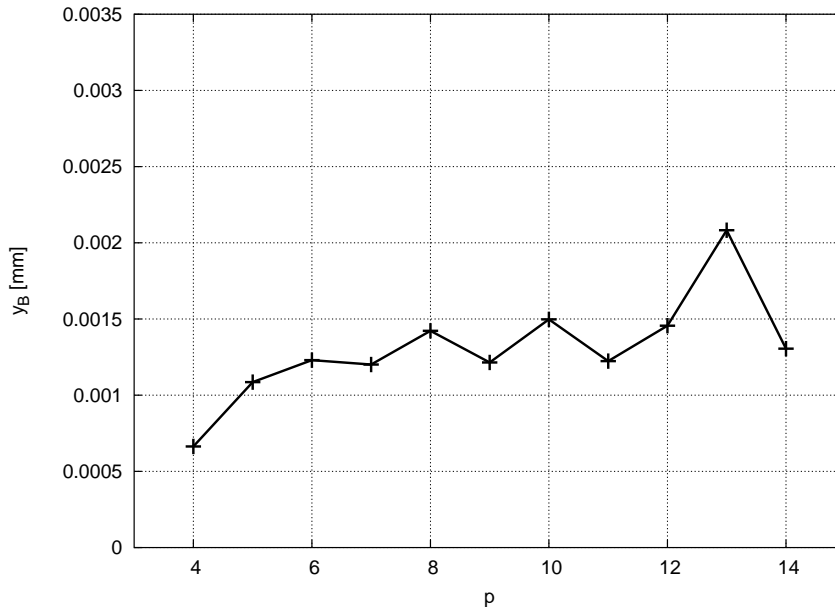


Figure 4.17: Calculation of the lateral vibration amplitudes from the measurement using the bearing. The absolute amplitude of the vibration y_B (in millimetre) is plotted versus the index of the rotation frequency p using the standard ball bearing instead of the shaker.

efficients for the frequencies $p = 1, 3$ were not measured it can be assumed that they are of the same order and only a quarter of the acceptable limit. The measurement of the higher order multipoles can tolerate vibrations of up to $50 \mu m$. The calculated vibrations are far lower than that limit.

4.3.4 Torsional shaft vibrations induced by the shaker

From the above calculations the transversal vibrations of the coil were estimated. The spurious harmonics induced by a torsional vibration of the shaft are given in Equation (2.51). The spurious harmonics induced by one torsional vibration mode $\zeta \sin(p\theta)$ are given by

$$\begin{aligned} C_{p+1}^s &\propto \frac{\zeta K_n}{K_{p+n}} C_n \\ C_{p-1}^s &\propto - \frac{\zeta \overline{K_n}}{K_{p-n}} C_n . \end{aligned} \quad (4.18)$$

n denotes the dominant harmonic in Equation (2.51), so n is 2 here.

Here the dominant sensitivity is the quadrupole sensitivity. The dipole compensation scheme $A - C$ was used to reduce the influence of the spurious harmonics induced by lateral vibrations. Similar to the lateral vibrations one vibration mode p induces a mode lower by two and higher by two. So the influence of torsional vibra-

tions are decoupled for all frequencies, whose index has not the same value modulo 4. From the harmonics measured in the dipole compensation scheme the magnet harmonics were subtracted and the remaining harmonics considered as pure spurious harmonics induced by the torsional vibrations. Similar as for the calculation of the transversal vibrations the following assumptions were made:

1. The spurious sextupole is only generated by the vibration with a frequency index $p = 5$.
2. The spurious octupole is only generated by the vibration with a frequency index $p = 6$.
3. The spurious decapole is only generated by the vibration with a frequency index $p = 7$.
4. The spurious dodecapole is only generated by the vibration with a frequency index $p = 10$.
5. The spurious multipole at $n = 12$ is only generated by the vibration with a frequency index $p = 10$.
6. The spurious multipole at $n = 13$ is only generated by the vibration with a frequency index $p = 11$.
7. The spurious multipole at $n = 14$ is only generated by the vibration with a frequency index $p = 12$.
8. The spurious multipole at $n = 15$ is only generated by the vibration with a frequency index $p = 13$.

Here the border conditions are questionable, especially as they cover the whole available range. The goal of this calculation, however, is to obtain an estimate of the overall amplitude of the torsional vibrations. If one of the border conditions is not fulfilled, the error will propagate during the calculation, and the calculated vibrations will be bigger than the real ones. Still the result allows to give an upper limit for the vibrations. Similar steps were performed as above:

1. Using the information of the spurious sextupole the corresponding torsional amplitude for the index $p = 5$ was calculated.

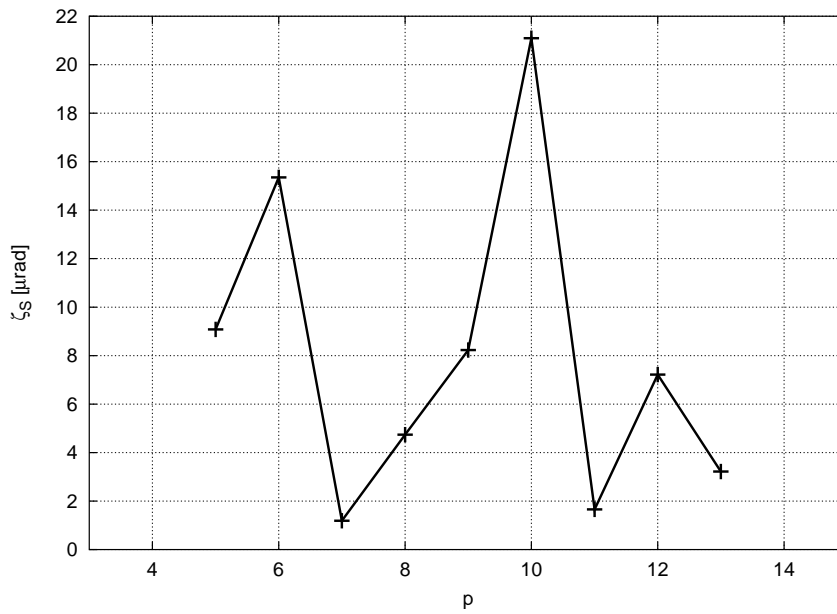


Figure 4.18: Calculation of the torsional vibration for the measurement with the shaker. The absolute amplitude of the vibration ζ_S (in milli rad) is plotted versus the index of the rotation frequency. $p = 1$ coincides with the rotation of the coil, 2 is equal to a frequency occurring twice during the rotation.

2. Using this deviation the spurious quadrodekupole was calculated.
3. From the difference of the measured spurious quadrodekupole and the calculated one the deviation for the index $p = 9$ was calculated.
4. Point two and three were repeated similarly for all higher harmonics up to harmonic 15 without taking the upper bounds into account.

It was repeated in the opposite direction too, without taking the lower bound into account. The mean value of the two values was taken and is shown in Figure 4.18. The amplitudes were found to be smaller than $\approx 20 \mu rad$.

4.3.5 Torsional shaft vibrations at measurement conditions

As the same measurement was performed with a coil equipped with two ball bearings the same analysis described above was performed. The amplitudes were found to be smaller than $10 \mu rad$ (See Figure 4.19). For the absolute and compensated measurements the maximal acceptable amplitudes are $100 \mu rad$ and $800 \mu rad$ respectively. So the amplitude of the vibration estimated by the measurement is ten times smaller than the limit.

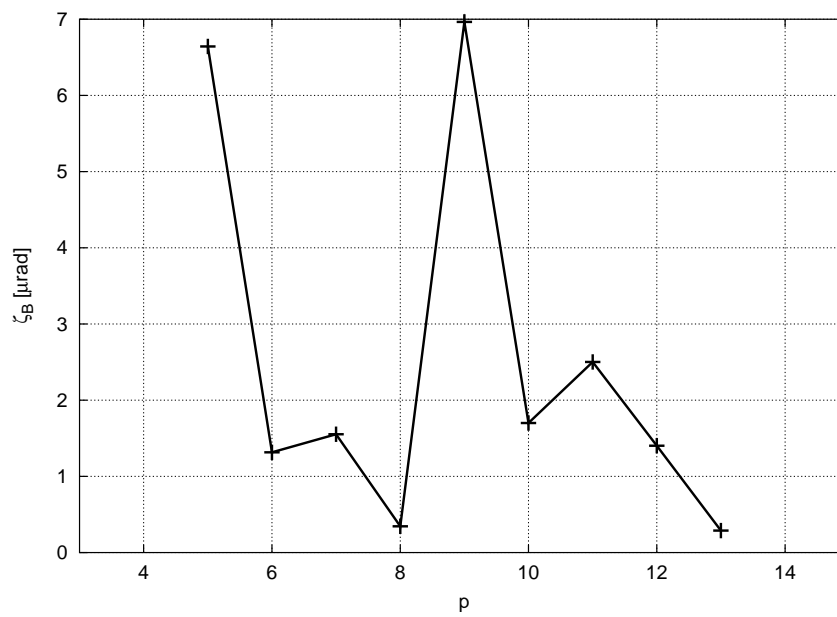


Figure 4.19: Calculation of the torsional vibration amplitudes for the measurement with the bearing. The absolute amplitude of the vibration ζ_B (in milli rad) is plotted versus the index of the rotation frequency. $p = 1$ coincides with the rotation of the coil, 2 is equal to a frequency occurring twice during the rotation.

4.4 Motor speed vibrations

So far vibrations between the coil and the angular encoder were considered. Now vibrations are considered which are induced by the motor. All data discussed here are only calculated. Further it is assumed that the shaft transmits the vibrations directly to the coil array without any change of the spectrum. As the angular encoder is located next to the motor, the angular encoder triggers the readout at the right moment, as long as the assumption of the shaft's behaviour is correct. Introducing the motor vibrations into the system, the shaft's reaction can be estimated by the aforementioned measurement and analysis method (see Section 4.3.4). All electronics have offsets which generate spurious harmonics if not properly corrected. In the following the effect of motor vibrations depending on the applied correction method is described. The signal generated by each component and the propagation of that influence will be illustrated. The motor vibration amplitude was chosen too large to be realistic, but it allows to visualise its influence on the system.

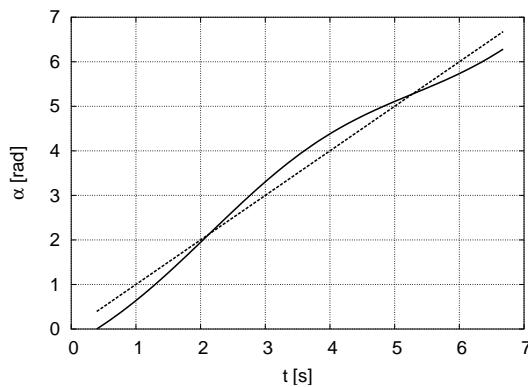


Figure 4.20: The angle of the motor α (in radians) is plotted versus time t in seconds.

The *motor* angle versus time is visible in Figure 4.20. The straight line marks the ideal behaviour. The deviation is due to the vibration. The speed was chosen to be one turn per second. The amplitude of this vibration was chosen to be 40% of the speed.

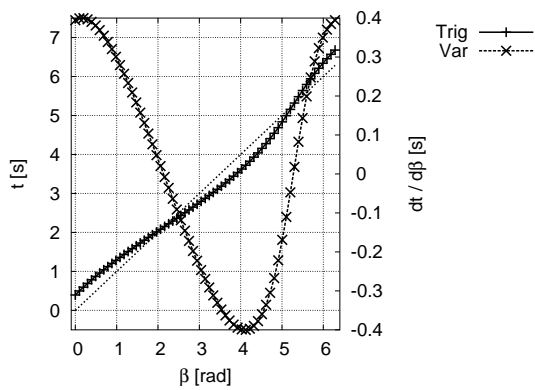


Figure 4.21: The time of the trigger impulse sent by the angular encoder t (in seconds) is plotted versus the angle β (in radians) as measured by the angular encoder (left scale). The variation of the trigger events $dt/d\beta$ is shown on the scale at the right.

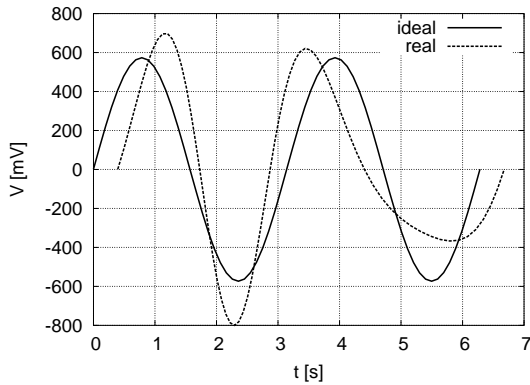


Figure 4.22: The output of the field probe (in milli volts) is plotted versus time t (in seconds).

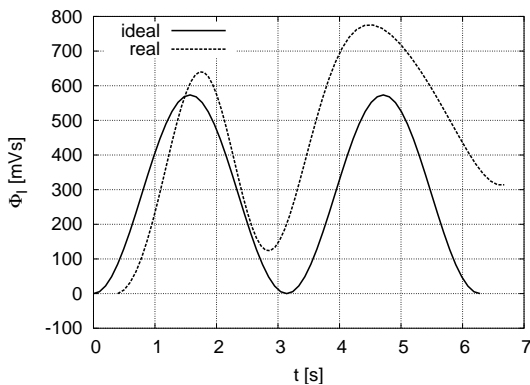


Figure 4.23: The integrated signal Φ_I (in millivoltseconds) is plotted versus time t (in seconds).

In Section 3.7.1 the method to correct the integrator offset was described. In the following graphs the advantage over a previously used method will be described.

The *angular encoder* triggers the measurement to ensure equally spaced steps. The crosses mark the time points, when the trigger occurs (labelled Trig). The plot (Figure 4.21) shows the angle versus the trigger time on the left scale. The variation of the trigger events from the ideal regular time spacing is shown on the right hand scale (labelled “Var”).

The *sector* or field probe measures the field. The induced voltage versus time is given in Figure 4.22. On the plot one can clearly see the “deformation” of the signal due to the vibration.

The output of the *integrator* Φ_I is given on the left. The “deformation” of the plot is due to the irregular motion. The shearing is the result of the integrator’s input offset ($= 50 \text{ mV}$).

Both methods use the fact that the offset of the last point N is equal to the integrator offset Φ_{IN} . In the standard method (in the graphs it is labelled 'cor') the time spacing between the points is taken into account. Previously the offset was subtracted by using:

$$\Phi_{Iic} = \Phi_{Ii} - \frac{\Phi_{IN}}{N}i, \quad (4.19)$$

with Φ_{Iic} the corrected flux, and Φ_{Ii} the i^{th} output of the integrator. (In the graphs the results of this method is labelled 'average'.)

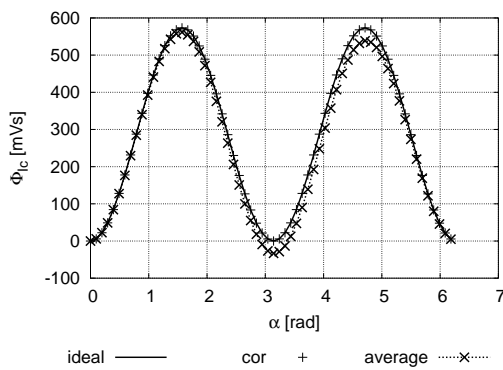


Figure 4.24: The flux Φ_{IC} (in millivoltseconds) after correction is plotted versus the angle of the sector β (in radians).

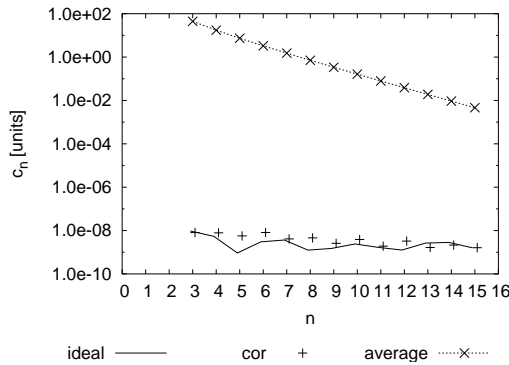


Figure 4.25: The normalised calculated harmonics c_n (in units) are plotted versus the order of the harmonic n .

In Figure 4.24 the fluxes are plotted. The line shows the ideal flux. The flux calculated with the standard method nicely matches the ideal signal. The flux calculated with the “average” method shows a easily visible deviation from the ideal flux.

The corrected flux is analysed for its harmonic content. The difference between the ideal result and the result from the standard correction method is due to the numerical limit of the calculation. The “average” method is not able to correct the integrator output.

The standard correction method allows to correct the integrator offset and motor vibrations within the limits of the numerical calculation. This limit is a few magnitudes smaller than the measurement precision. Therefore motor vibrations per se will not debase the measurement. They can, however, enforce vibrations of the following mechanical connections, which can be estimated as described in Section 4.3.4. The chosen amplitude is ten times larger than a realistic vibration. Using

the “average” called correction method spurious harmonics of 100 units were generated. Even 10 units are not acceptable for such a system. Therefore without a precise timing as used here a much better controlled rotation would be necessary.

Conclusion

Different effects deteriorating the measurement quality were considered. First the influence of electrical noise was discussed, followed by the qualification of the mechanical quality of the system. Finally the effect of the coupling of motor instabilities and the integrator offset were described. In the following table the limits for the different effects are listed, which still allow an accurate measurement.

Table 4.2: Acceptable limits for the different imperfections.

type	unit	absolute system		compensated system	
		requirement	effect	requirement	effect
torsional	<i>mrاد</i>	0.1		0.8	
transversal	μm	10	10^{-4}	50	$2 \cdot 10^{-6}$
spikes	<i>mV</i>	–		3	
ripple	<i>ppm@300 Hz</i>	35		–	
integrator offset	<i>V</i>	No effect if properly corrected			

Chapter 5

Qualification of the axis measurement

Quadrupoles focus the beam of an accelerator, so particles heading off the orbit are bent back (see also Section 1.1.3). A misplacement of a quadrupole generates a faked dipole and distorts the closed orbit and the total beam performance. Therefore the axis of the quadrupoles has to be measured with respect to the outer fiducials to allow a precise installation of the magnet with respect to the closed orbit. These fiducials are survey marks, which are used as external references to install the magnet.

5.1 Discussion of the accuracy target

Due to the size of the LHC active suspension of the magnets or beam based alignment is not feasible. Therefore the following effects have to be considered to formulate the measurement accuracy target:

- *The precision of the survey measurements:* The tunnel has a circumference of 27 kilometres. The magnets can be installed with a maximum accuracy of 0.5 mm with respect to the ideal orbit. For the machine performance the alignment of a magnet with respect to its neighbours is more important than its alignment with respect to the global ideal orbit. This means, a smooth and slowly varying orbit distortion has no effect on the beam. Therefore the magnet's position is measured with respect to its neighbours as well. Then calculations are made to arrange them on a smooth curve. The magnets can be placed with respect to this curve with an accuracy of 0.15 mm [44]. From the axis measurement its location with respect to the fiducials is derived. Any error in this measurement

will result in a wrong installation and alignment of the magnet in the tunnel. Thus, the accuracy of the axis measurement must be more accurate than the installation precision, not to degrade the total machine performance.

- *The movement of the tunnel:* Earth is not solid rock. The tunnel shows different movements within different areas, which can be up to 0.5 mm per year [45, 46]. Although these movements are slow, an axis measurement with much better accuracy than the movement does not improve the performance of the machine.
- *Beam requirements:* A misplaced quadrupole generates a dipole. This dipole generates an orbit distortion. All fake dipoles induced by quadrupoles must be compensated by the dipole correcting system. It can cope with a maximum offset of 0.37 mm assuming a Gaussian distribution of all quadrupole misalignments.

Following the aforementioned considerations the magnet alignment working group established the target of 0.15 mm as the required precision, which obviously must be considered as an ambitious target. The axis of the quadrupole magnets for HERA were measured with an accuracy of 0.2 mm . Further on, even if the magnet is only 3 m long, the cryostat containing the quadrupole, cryogenic supply and end cap sum up to a total length of 12 m . So the precision of 0.15 mm has to be achieved over 12 m .

The data representation of the magnet is given in the rst - frame (see also Figure 5.1). The centre of the coordinate system is the magnetic centre of both magnets. The t axis points upwards, the s axis is parallel to the apertures and the r axis is oriented in such a way that a right hand rst - system is established. The calculation procedure is presented in Appendix C.1.

5.2 System Parts

In the following the performance of each part of the axis measurement equipment will be discussed with focus on the optical equipment. It limits the achievable precision and is therefore the most critical part of the axis measurement setup.

In Section 3.8 the measurement procedure was outlined. The magnetic axis location starts the vector chain, all subsequent steps are performed optically. In Chap-

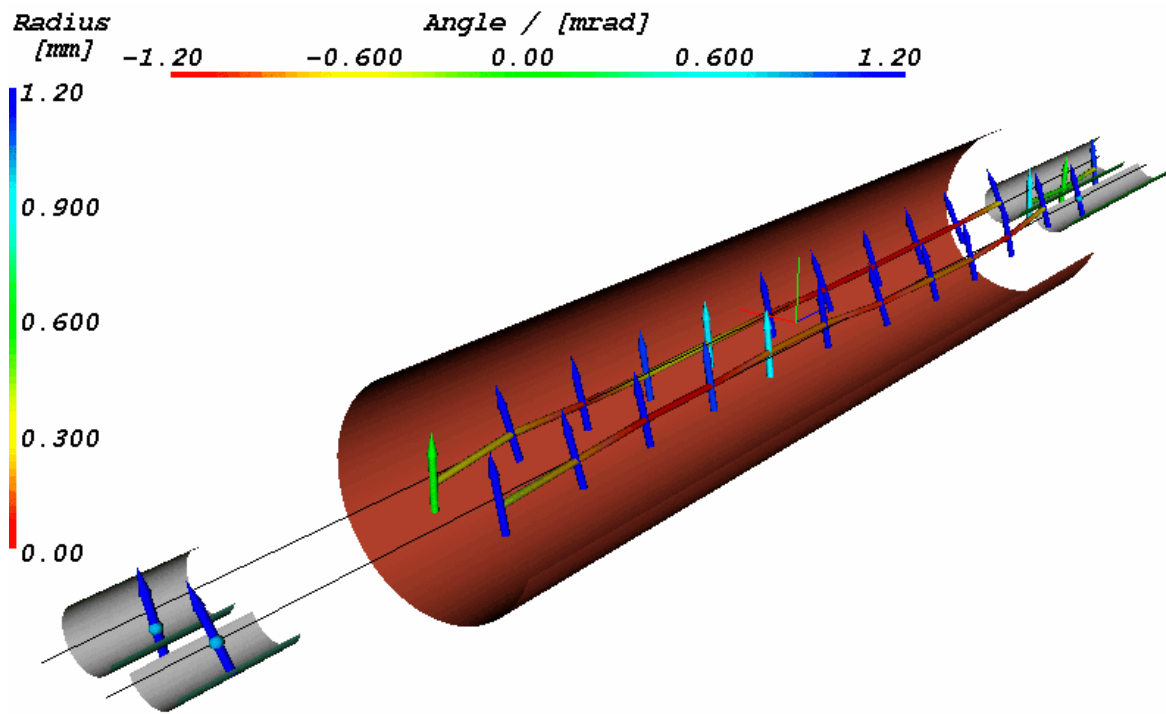


Figure 5.1: The final goal of the measurement is the description of the magnetic axis in the r, s, t frame. The r axis is marked red and describes the lateral offset, t , marked green, describes the vertical offset. s describes the offset of the fiducials to the centre of the magnet. The curves indicate the measured axis and the arrows indicate the direction of the field. The arrows indicate the angle of the field. The angle is oversized, but the arrows are coloured according to their real angle (see the colour bar at the top). The spheres and tube indicate the location of the axis, the offset is oversized, too. The real offset is indicated by the colour of the spheres and tubes (see the colour bar at the left). In the front one point of the octupole is visible followed by the measurement points of the quadrupole. On the rear end the measurement points of the sextupole are indicated. The offset from the ideal axis is oversized to make the shape visible. The colouring of the points and lines shows the offset (colour bar on the left). These data were taken from the first campaign of SSS3.

ter 4 the performance of the magnetic measurement system was shown. Here it will be shown that the requirements to the magnetic part of the axis measurement are softer than the requirements for the field quality measurement. The main concern will focus on the optical performance of the axis measurement system and on the necessary steps to guarantee this performance during the whole measurement campaign.

5.2.1 Axis Searching Coil

The offset a_m of the magnet field axis to the rotating coil is given by the “feed down” (see Equation 3.7 and 2.39)

$$a_m = -\frac{R_{Ref}}{m-1} \frac{C_{m-1}}{C_m}, \quad (5.1)$$

with C_m the strength of the main multipole m , and C_{m-1} the strength of its predecessor. The error of this measurement is given by

$$\Delta a_m = -\frac{R_{Ref}}{m-1} \Delta c_{m-1}, \quad (5.2)$$

with c_{m-1} the normalised harmonic (see Equation 2.2) of the predecessor. Setting Δa_m to $10 \mu m$ one can calculate Δc_{m-1} to ≈ 6 units. This requirement is 4 times softer than the requirement to the absolute field measurement (see also Table 1.1). From Equation (5.2) one can see that the requirement is even softer for the correctors, which are quadrupoles or higher order magnets.

5.2.2 Glass Window Influences

The anti-cryostat is heated to prevent its icing, its temperature can vary locally from 8 to 25 degree Celsius [47]. The LED of the axis searching coil is measured optically through the anti-cryostat. The temperature gradient generated by the temperature difference between the ambient air and the air of the anti-cryostat can deflect the light beam up to $5 mm$ [35]. Thus the anti-cryostat is evacuated to reach reliable operating conditions.

Two glass windows are necessary to evacuate the anti-cryostat and allow the measurement of the LED's lateral position. The one mounted at the rear end of the anti-cryostat is the bigger one. It consists of BK7, has a diameter of $50 mm$ and a thickness of $15 mm$.

An estimate using the mechanical properties of the glass [32], whose properties are listed in Table 5.1, yields a deformation of a few tenth of micrometers. If one calculates the maximum light beam deflection, it is below $10 \mu m$. For further confidence the following test was performed: The axes of the magnets were measured a few times in the telescope frame with a different tilt of the glass window next to the telescope. All results were identical within the measurement precision. Therefore one can conclude that the deformation of the glass window due to the ambient air pressure does not affect the axis measurement.

Table 5.1: Glass window parameters. The properties of the window mounted at the end of the anticryostat are listed here.

material	BK 7
diameter	50 mm
thickness	15 mm
elasticity modulus	$82 \cdot 10^3 \text{ N/mm}^2$

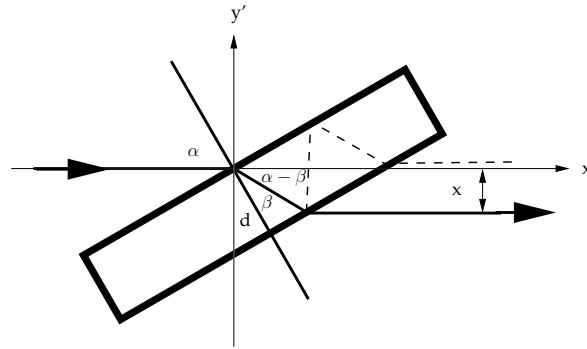


Figure 5.2: Offset of an light path due to a tilted plate with a thickness d . The plate was turned around the z' -axis, which is normal to the paper plane pointing upwards. The tilt plate's normal is inclined by an angle α from the negative x' -axis. The angle β is calculated by Snells' law. Parallel polarised light oscillates in the $x'y'$ -plane and normal polarised light oscillates in the $x'z'$ -plane. The dashed line represents the path of light, which has been reflected twice. It has an offset x with respect to the normal traversing light.

Influence of reflections of the LED Light on the measurement The light coming from the LED is also reflected by the surfaces of the glass window and could disturb the measurement, as the reflected light could vary the intensity of the image of the LED. In Figure 5.2 the dashed line shows which path the reflected light has to take to influence the measurement. It must be first reflected back by the outer surface of the glass window, reflected again by the inner surface and then transmitted to the observer. The intensity of the reflection and the transmission of a surface is described by Fresnel's law ([48, 49]). The reflectivity \mathcal{R} for parallel \parallel and vertical incidence \perp is described by

$$\mathcal{R}_{\parallel} = \frac{\tan(\alpha_i - \alpha_t)}{\tan(\alpha_i + \alpha_t)} \mathcal{E}_{\parallel} \quad (5.3)$$

$$\mathcal{R}_{\perp} = -\frac{\sin(\alpha_i - \alpha_t)}{\sin(\alpha_i + \alpha_t)} \mathcal{E}_{\perp}, \quad (5.4)$$

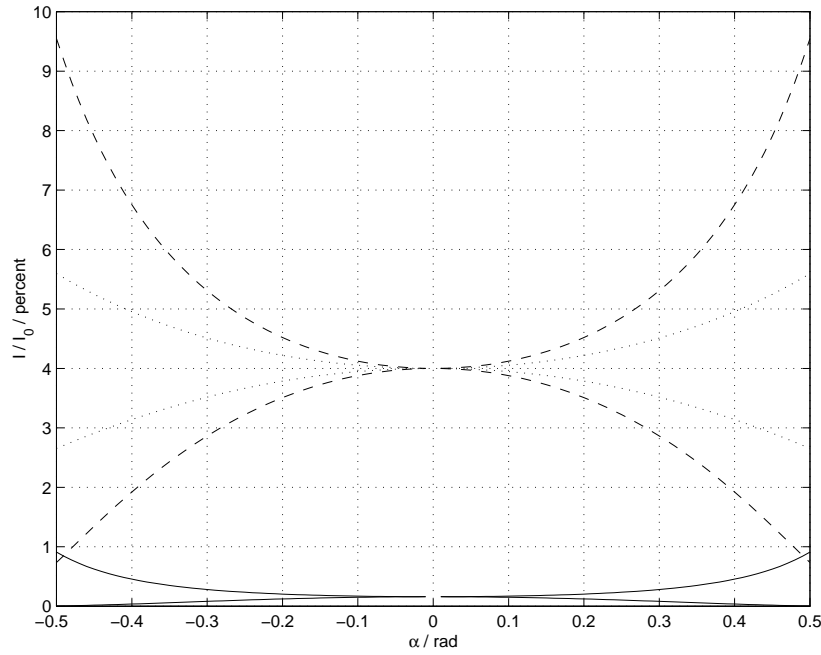


Figure 5.3: The percentage of the reflected intensity I over the original intensity I_0 versus the angle of the glass surface α . For this calculation the refractive index of glass was assumed to be 1.5. The percentage for passing from the air to the glass is shown in the dotted curves, for the opposite direction in the dashed curves. The solid curves represent the reflected intensity for double reflection on glass (As indicated in figure 5.2 with the dashed line). The up bound graphs are the results for vertical polarised light, the down bound graphs for parallel polarised light.

with α_i the angle of the incident wave, and α_t the angle of the transmitted wave and \mathcal{E} the electrical vector of the light. For a detailed deduction see [48, 49]. The transmission \mathcal{T} is given by

$$\mathcal{R} + \mathcal{T} = 1. \quad (5.5)$$

The aforementioned beam has been reflected by the back surface, reflected from the front, and transmitted by the back. As the intensity is the square of \mathcal{E} , the final intensity I is given by

$$I = (\mathcal{R}^2)^2 I_0, \quad (5.6)$$

when ignoring absorption in the glass, with I_0 the light passing the glass without reflection. In Figure 5.3 the percentage of reflected light versus the inclination of the plate is shown. The solid line represents the percentage reflected by two surfaces. This gives a reflection with an intensity of 0.16 % of the original beam's intensity at an angle of 0.1 rad. This angle is much larger than the inclination found on the installation. As any silicon detector is a linearly working device, (contrary to the

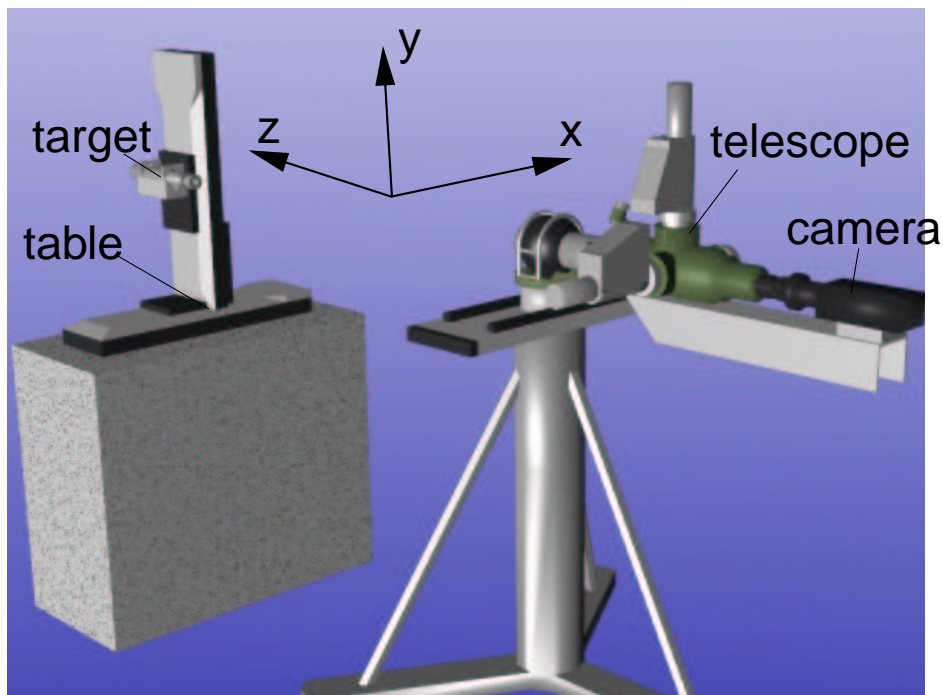


Figure 5.4: Sketch of the tracker calibration system. On the left the table mounted on a concrete block is visible. On the right the telescope is resting on the tripod. Courtesy of Sebastien Gonzalve [50].

eye, which is a logarithmic “device”), a reflection contributes as much as $\approx 0.2\%$ to the intensity distribution. As a rule of thumb, one can assume that a CCD - Camera has not a better intensity accuracy than 2%. The reflections generated by the glass window can be safely neglected, as the reflection’s intensity is only a tenth of the intensity measurement precision of the CCD - Camera.

5.2.3 Telescope calibration

For the axis measurement two optical systems are used: the laser tracker and the telescope tracker. The former is a commercial product shipped with its own calibration procedure. The latter is an application specific instrument built for its very purpose. The calibration procedure was implemented by Sebastien Gonzalve [50]. It was shown in Section 3.4 that the scaling factors depend on the distance between the telescope tracker and the target. Therefore the calibration has to be performed in the following way: The telescope is installed at a certain distance from the table (e.g. 1.5 m, see Figure 5.4). The table moves the target to a grid of points (see Figure 5.5). At each point the tracker measures the position of the target. These two

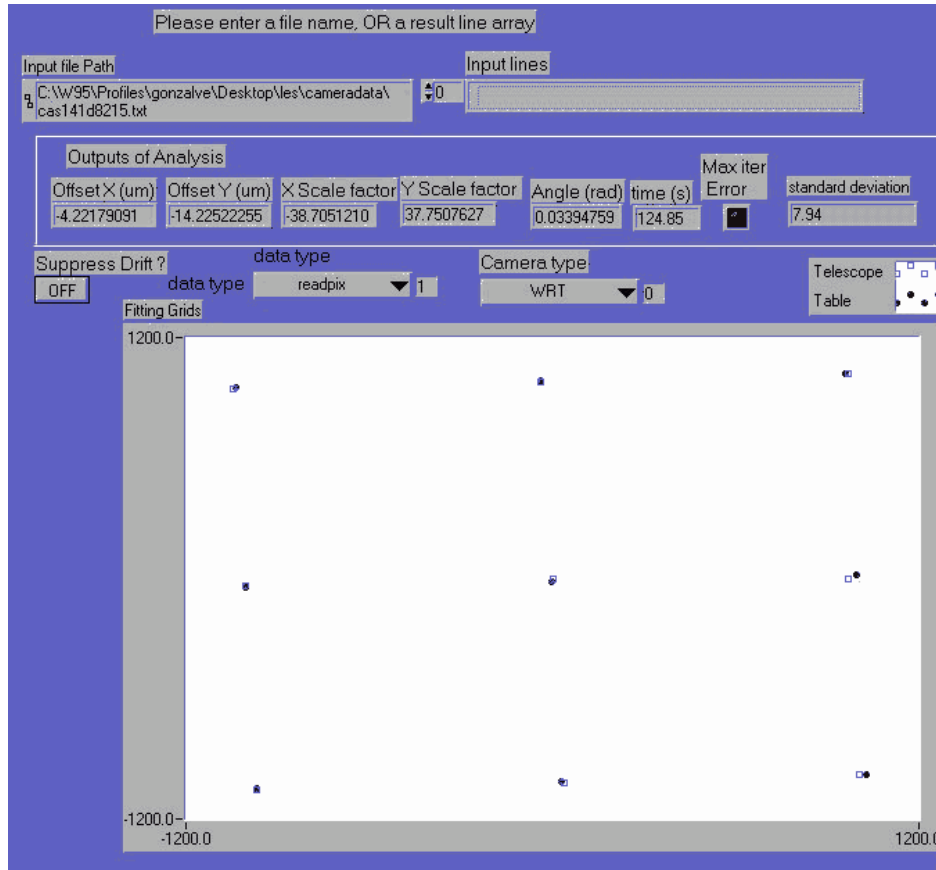


Figure 5.5: Sketch of the tracker calibration system. The table sets the target to a grid of points. At each point the telescope measures the position of the target. The data are displayed here. The circles represent the table's positions and the squares the telescope measurement. Comparing the measurement to the table values the telescope is calibrated. Courtesy of Sebastien Gonzalve [50].

measured grids are then compared against each other. By turning, shifting and scaling the telescope grid, it is matched with the table grid. The scaling factors for the x and y coordinate are the calibration factors for that distance. (The turn and the shift depend on the initial setting of the tracker versus the table.) This measurement is repeated over the whole z range (1.5 - 14 m). To obtain a scaling factor for any z -distance these scaling factors are fitted with the rational polynomial

$$z = \frac{a + b \cdot st^d}{a + b \cdot st^d + 1} + c, \quad (5.7)$$

with st the steps of the step motor, and a, b, c, d the fitting parameter. The whole measurement may appear simple, the high precision ($< 30 \mu m$), however, over a distance of 14 m is challenging. Air fluctuations between the target and the telescope can deform the light beam significantly. The grid was chosen, since the calculation

still gives good results even if the measurement quality of some points is decreased. It was experienced during the usage of the bench that these influences are detectable by visual examination of the grids. Then appropriate action can be taken to improve the environment (e.g. closing open doors, removing heat sources).

5.2.4 Checking the straightness of the telescope axis

The aforementioned procedure checks the correctness of the scale factors. The straightness of the optical axis can not be checked with the above procedure. The optical axis of the telescope tracker was checked and commissioned on the vendors side. A second telescope (WRT) however arrived later and was checked at CERN. The principle of the check is the same for all types of telescopes, so the procedure is illustrated using this calibration. For this measurement the laser tracker was used as the reference system (see Figure 5.6). The telescope was placed on one support. Then three other supports were placed in the telescope line of sight. On each support a fiducial was fixed. The support next to the camera and the support on the far end were used as reference points. The support in the middle was used as measuring point. A standard retroreflector was used for the laser tracker. The “firefly” was used as a target for the telescope tracker. It is special made sphere, having the same dimension and precision as the standard retroreflector but housing an illuminated diaphragm located at the sphere’s centre.

The measurement was carried out in the following way:

1. First the firefly was placed on the reference points. The reference points were aligned to be on the axis of the WRT.
2. These points were measured by the laser tracker using its standard target.
3. Now the procedure was started to measure the intermediate points:
 - (a) The middle support was placed at a proper measurement position and the target was aligned to the telescope line using the laser tracker.
 - (b) The position was measured by the laser tracker.
 - (c) The firefly was placed on the support and the position was measured by the telescope tracker.
4. After every other intermediate point the reference points were remeasured to warrant the precision during the whole measurement.

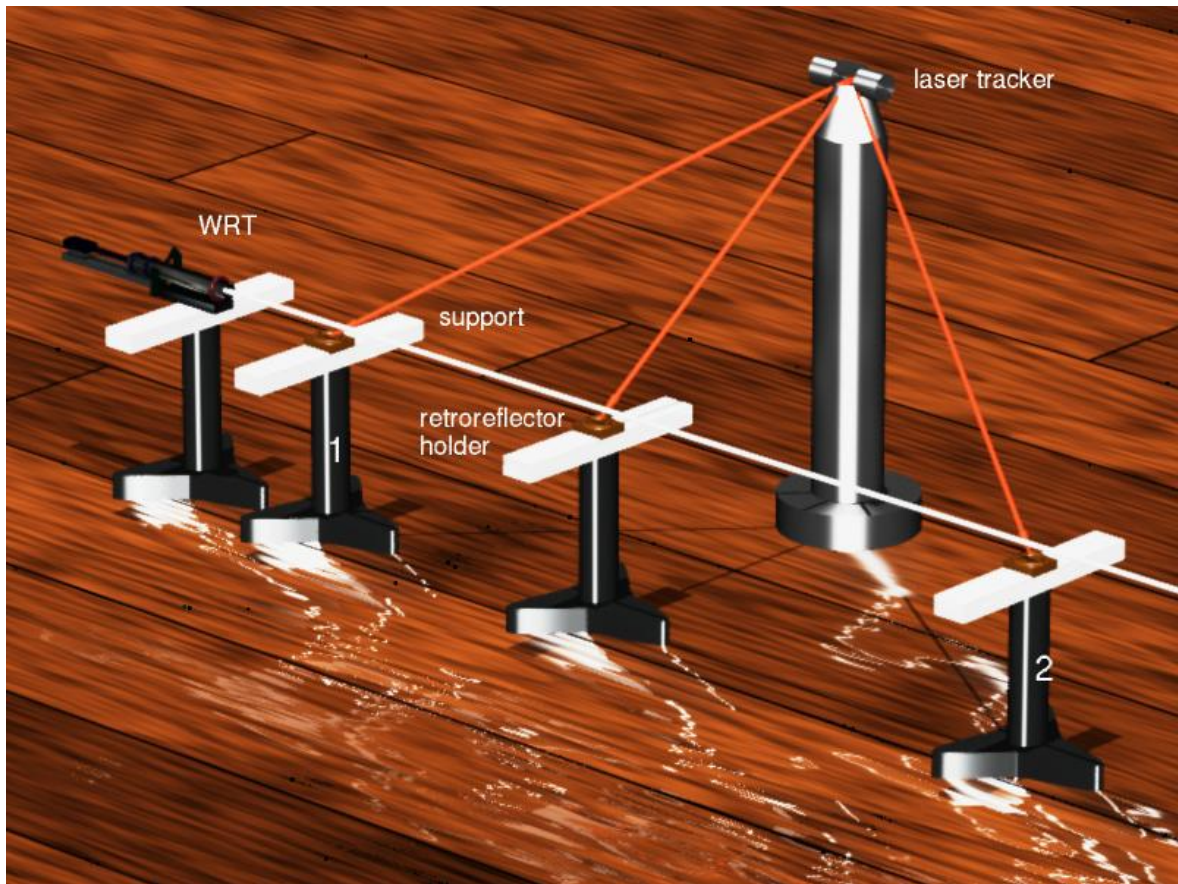


Figure 5.6: Setup of the measurement of the axis. On the left the camera is shown mounted on its support. 3 other camera supports were used to hold the support for the retroreflectors. The one next to the camera and the one on the far right were kept stable to be used as reference points. The support in the middle was moved. “1” marks the first reference support, “2” the second one.

During the whole measurement the reference points showed a standard deviation of $< 15 \mu m$ for reference point 1 and $< 60 \mu m$ for reference point 2. As the WRT only needs to provide a precision of $100 \mu m$ this result is acceptable. The difference between the telescope measurement and the tracker measurement is shown in Figure 5.7(a). The axis established by the laser tracker and by the telescope is within specifications except for the point at $\approx 12.5 m$. From the measurement of the reference point 2 one can conclude that there was a drift of the telescope, as the position measured by the WRT changed with time, but was stable for the laser tracker measurement (see Figure 5.7(b)).

The SRT needs to provide a higher precision ($30 \mu m$), thus the above precision is not acceptable. From Figure 5.7(a) one can see that a conformity of $20 \mu m$ was reached for the y component of the measurement. So this goal is reachable taking all

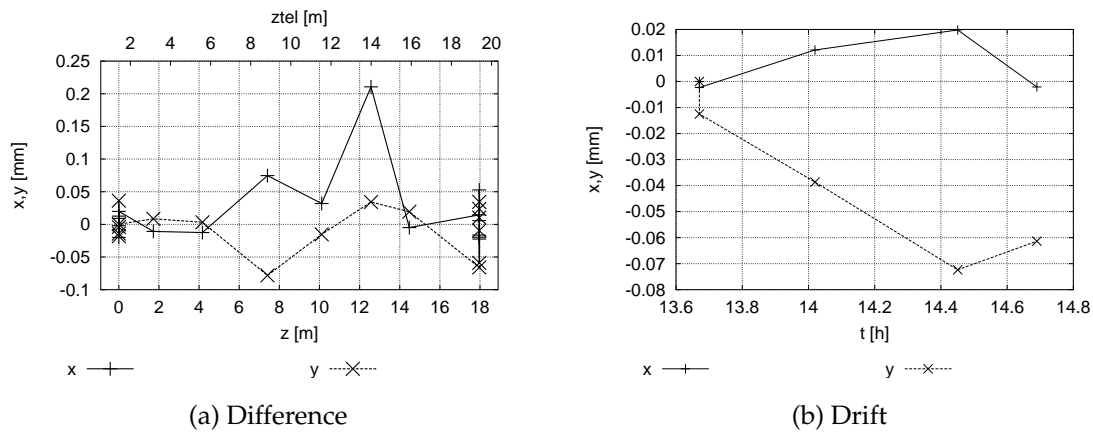


Figure 5.7: Result of the straightness check of the axis tracker. On the left the difference between the laser tracker and the telescope measurement are shown. This distance is plotted for x (horizontal) and y vertical (in millimetre) versus the distance of the point in the laser tracker coordinate frame at the bottom z (in metre) and the telescope frame z_{tel} (in meter) at the top. The spread of the points at the extremities shows the precision of the reference measurements. On the right the drift of the second reference point versus time t (in hours) is shown as seen by the telescope. The laser tracker measurement however remained stable. As the telescope tracker measures the spot from a larger distance, it is more sensitive to air gradients than the laser tracker. This explains why the differences between telescope and laser tracker get bigger when moving to the right.

precautions to ensure that no thermal gradients affect the measurement e.g. working during off peak hours (weekend or evenings). The available precision can be monitored carefully inspecting the reference points and taking appropriate actions.

5.2.5 Reference quadrupoles

Beside providing an angular reference the reference quadrupoles establish the link of the telescope frame to the survey frame. This measurement is performed on a separate bench [51], which is also based on the rotating coil technique. This coil is similar to the axis searching coil, except that instead of the LED a target for the laser tracker is mounted in the middle of that coil. As the laser tracker permits three-dimensional absolute measurements, the rotation axis of the coil can be measured with respect to the magnets fiducials. Adding the feed down to this value the magnetic axis can be calculated in the fiducials frame. As aforementioned a precision of $10\ \mu m$ is feasible for the feed down. The laser tracker is specified to $50\ \mu m$ [52]. A careful error estimation showed, that the axis can be measured with a total precision of $20\ \mu m$ [51].

Table 5.2: Total System Performance. The random accuracy of each device is listed. The total accuracy is calculated using Equation 5.8.

Device	Accuracy [μm]
telescope	30
reference quadrupole	20
laser tracker	50
magnetic measurement	10
total	70

5.3 Total System Random Error

In the axis measurement a few systems are working together to obtain one field datum: the axis. Here the precision of each device is summed up and the total random error of the system is indicated. A precision of 10 μm can be obtained from the magnetic measurement. The reference quadrupole axis provides an accuracy of 20 μm . The laser tracker is specified to 50 μm precision (see also Table 5.2). As the systems are independent and should not be correlated by some external parameter (e.g. the ambient air temperature), the square root of all squared errors seems acceptable as an estimate of the total error. The error for the telescope and magnetic measurement have to be taken twice, as these measurements are performed in the SSS and in the reference quadrupoles. So one calculates the total error of the axis measurement Δ_{axis} :

$$\begin{aligned}\Delta_{axis} &= \sqrt{\Delta_q^2 + \Delta_{Lt}^2 + 2(\Delta_{SRT}^2 + \Delta_{mag}^2)} \\ &= \sqrt{(20^2 + 50^2 + 2 \cdot (10^2 + 30^2))} \mu m = 70 \mu m,\end{aligned}\tag{5.8}$$

at one sigma, with Δ_q the error of the quadrupole measurement, Δ_{Lt} the error of the laser tracker, Δ_{mag} the error of the magnetic measurement and Δ_{SRT} the error of the short range tracker.

During the SSS4 measurement campaign four axis scans were performed. After two scans with the Antbear, a laser tracker measurement was conducted, the reference quadrupoles were moved, put into place again and the SRT was moved and realigned. In Figure 5.8 the results of these measurements are shown. It is a random error estimate based on 4 axis scans and 2 laser tracker measurements. The end points indicate the quality of the survey measurement. During the axis calculation

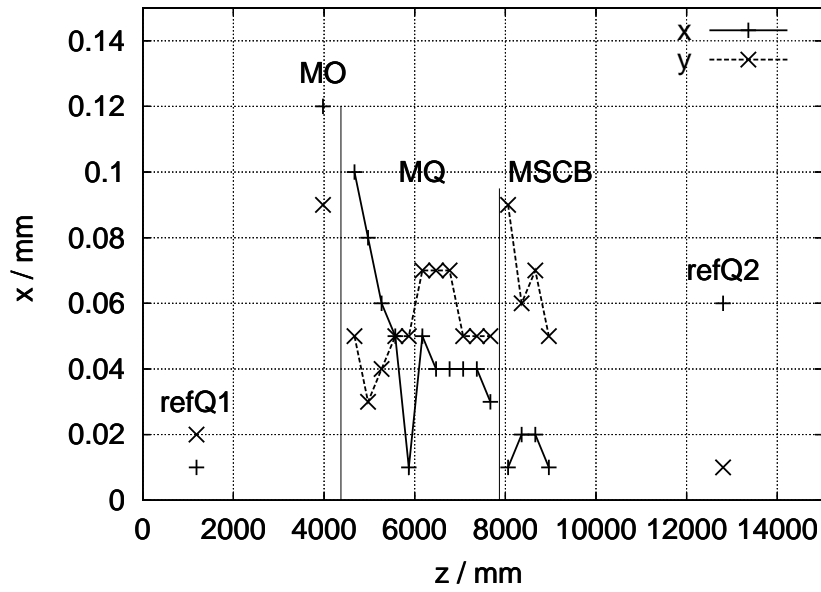


Figure 5.8: Total axis system performance. The standard deviation of each measurement is plotted versus the position z . The first and the last point (reference quadrupole measurements) show the quality of two survey measurements. The others, which show the total performance, are mostly below $60 \mu m$. MQ denotes the main quadrupole, MO the octupole corrector, MSCB the combined dipole sextupole dipole corrector (see also Figure 1.8 Page 13). refQ1 denotes the first reference quadrupole and refQ2 the second one.

the telescope frame is attached to the SSS's fiducials frame. Therefore the magnetic and SRT measurements are set to zero in these points and, thus, they do not contribute to the random error in these points. The other points show the total system performance. In average it is well below $70 \mu m$ at 1σ .

5.4 Necessary Environmental Constraints for the measurement area

All measurements are conducted in the hall dedicated for the magnetic measurement. More than one thousand magnets have to be measured within four years. Thus, heavy masses are frequently shipped to this hall. Like any static structure, this building does and must react to load changes. Therefore the installation of a support for an experiment, located near to the scanner, was used to investigate that effect. The installation procedure started with the delivery of concrete plates with a weight of 50 metric tons to SM 18, which were to be used as the experiment's

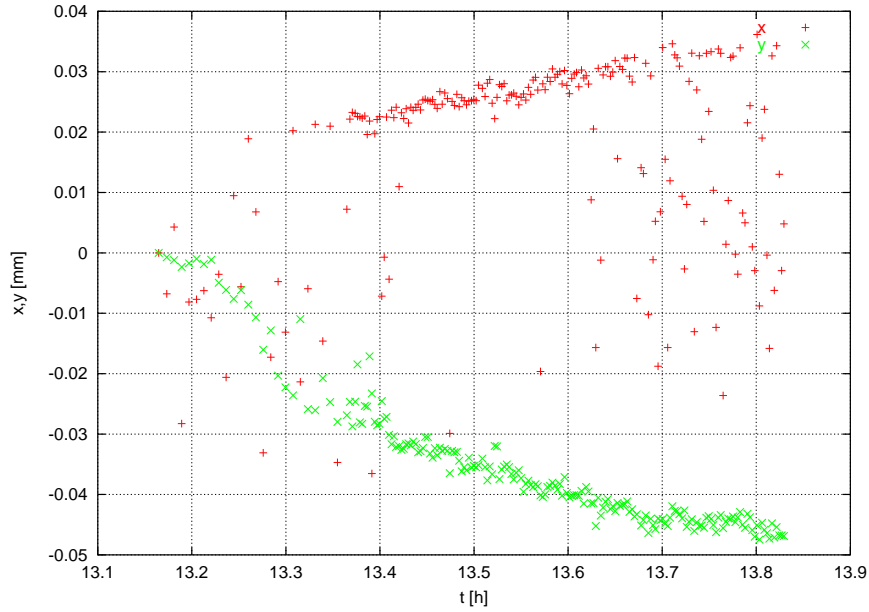


Figure 5.9: Effect of loading. The measured position of the axis searching coil x, y (in millimetre) is plotted versus the time t (in hours). The position of the axis searching coil was observed for roughly one hour, after a load of 50 metric tons was installed next to the Antbear. One can see that the coil moved $30 \mu m$ in x and $40 \mu m$ in y with respect to the telescope.

support. When these blocks arrived, the axis searching coil was placed inside the reference quadrupole next to the Antbear. The tracker was continuously measuring the position of the coil over a period of roughly one hour. The result is given in Figure 5.9. One can see movements of up to $50 \mu m$. Further on the axis measurement conducted right after this loading showed large deviations with respect to the outer axis measurements (see Figure 5.10).

As buildings are complex objects, their reactions to such loadings are not simply predictable, therefore one has to demand:

No heavy load relocation (more than one metric ton) should be scheduled in the measurement area, when an axis measurement is foreseen.

5.5 Comparison to a stretched wire measurement

The SSS5 was measured in warm condition using the single stretched wire [17] and the Antbear. The single stretched wire can also measure the axis in the fiducials frame (see Figure 5.11). The stretched wire measures the centre, the pitch and the

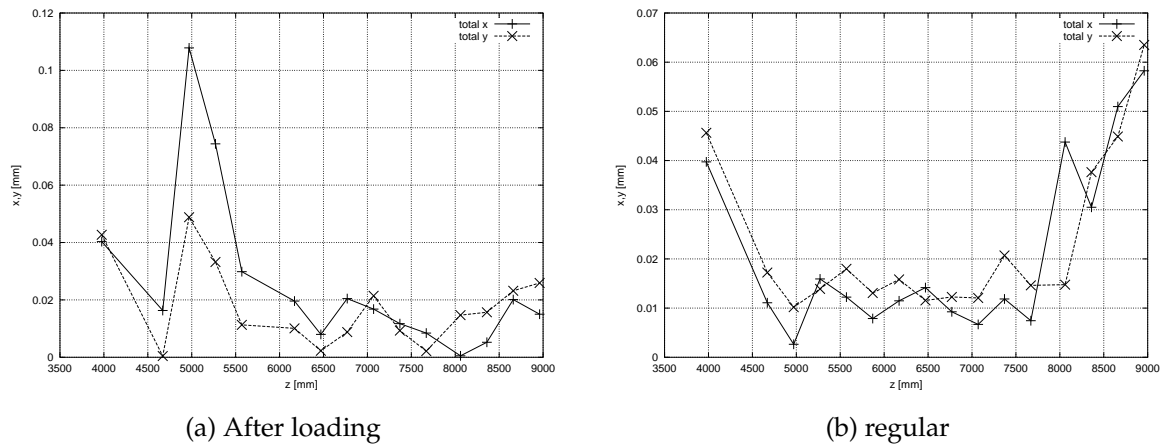


Figure 5.10: Influence of the loading on the quality of the axis measurement. The standard deviation for the measurement of the coordinates x, y (in millimetre) is plotted versus the z position (in millimetre). On the right the standard deviation taken from good measurements is shown. On the left the standard deviation for good measurements and the measurement made after the loading is shown. The errors are twice larger than for the good scans and bigger than the limit of $40\mu m$ (magnetic measurement and telescope tracker).

yaw of the axis [53]. The Antbear measures the axis position integrated over the coil length. To compare the two measurements the following calculations were necessary:

1. A line was fitted through the measurement points of the Antbear.
2. The data of the field quality measurement was used to calculate the magnetic centre of the magnets.
3. The reference quadrupoles were scanned using the axis searching coil. From these data the centre of the reference quadrupoles was calculated.
4. It was assumed that the magnetic centre coincides with the geometric centre of the reference quadrupoles.
5. Using the above steps the centre of the magnet was calculated in the survey frame (see also Section 3.8).

In Table 5.3 the results of the two measurements are given. For aperture #2 the data show a difference of $\approx 0.1\text{ mm}$ in x and y . For z the difference is 0.5 mm . In aperture #1 the difference is $\approx 0.25\text{ mm}$ in x and y , an accuracy worse than required (see Table 1.1). During the survey measurement the measurement of the control

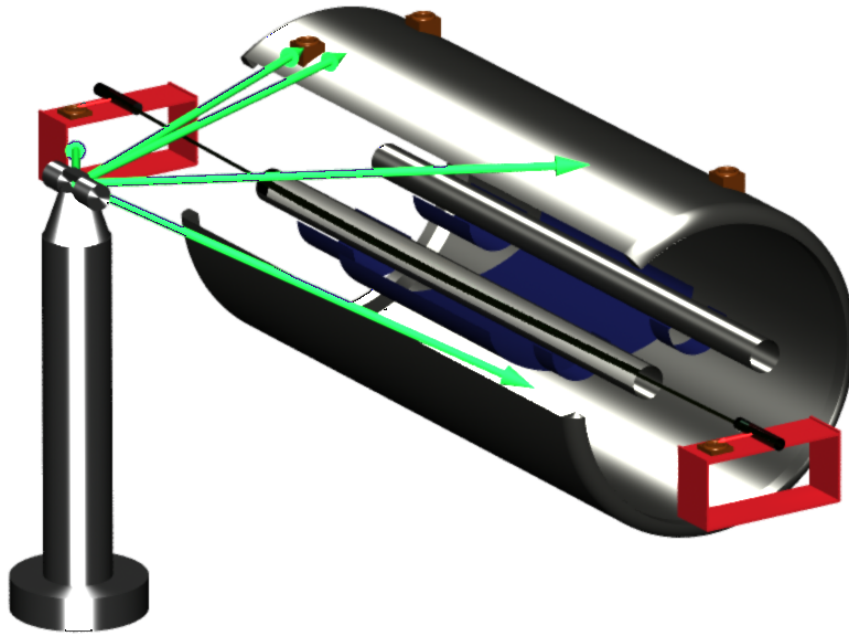


Figure 5.11: Setup of the stretched wire measurement. For a cross check a stretched wire was used. The stretched wire supports are placed at both ends. These move the wire, which is stretched through the bore of the magnet. The distance between the wire support and its fiducials (indicated by the red arrows) was measured on a dedicated bench. The laser tracker measurement (indicated by the green arrows) closes the vector chain to attach the measurement to the fiducials.

Table 5.3: Comparison of the single stretched wire (SSW) measurement to the Antbear measurement. All data are presented in the fiducials frame. The magnetic centre is described by the coordinates x, y, z (in millimetre). The pitch α_p and the yaw α_y are given in milliradians. Ap1 denotes aperture #1, which is the one on the left side in Figure 3.13. Ap2 denotes aperture #2.

Instrument		magnetic centre			magnetic inclination	
		z [mm]	x [mm]	y [mm]	α_y [mrad]	α_p [mrad]
Antbear	Ap1	1419.4	-479.93	-337.94	-0.894	-1.300
	Ap2	1417.9	-285.25	-338.19	-0.912	-1.292
SSW	Ap1	1422.3	-479.67	-337.70	-0.886	-1.321
	Ap2	1418.0	-285.25	-338.10	-0.877	-1.273
Difference	Ap1	-3.0	-0.26	-0.24	-0.008	0.021
	Ap2	-0.1	0.00	-0.09	-0.035	-0.019

points indicated a maximum precision of 0.3 mm . Since the reference quadrupoles were only scanned during the measurement of aperture #2, the intrinsic frame of the Antbear had to be attached to the survey frame using this datum for both aperture. During switching the apertures a movement of the Antbear of 3 mm with respect to the survey frame seems possible taking the aperture distance of $\approx 194\text{ mm}$ into account. When the survey measurement of aperture #1 for the Ant bear was conducted, mechanical work was ongoing on a nearby measurement bench disturbing the measurement quality of the survey. Therefore the larger error of aperture #1 can be explained by the disturbance of the survey measurement and the total Antbear axis measurement accuracy is stated to be 0.1 mm .

Conclusion

The axis measurement system was described here and the different equipment needed was listed. The optical systems limit the total precision as they are more affected by the environment than the magnetic system. The telescope tracker was specially manufactured for the axis measurements of the LHC magnets. A calibration bench was set up to warrant its performance during the whole measurement period. Further its axis can be checked using the laser tracker. The total random error of the axis system was measured to $70\text{ }\mu\text{m}$. Comparing the Antbear axis measurement to a single stretched wire the total system performance was shown to be better than 0.1 mm .

Chapter 6

Conclusions

6.1 Measurement Requirements

The quadrupole forms a vital component of an accelerator providing the focusing. Misplacement of a quadrupole effects the closed orbit. Uncertainty in the strength of the field results in improper focusing of the beam similar of using a lens of incorrect focal length in an optical system. This thesis focuses on the “Antbear measuring system” being the most flexible of all systems able to deliver all field parameters. To fulfil the requirements listed in Table 1.1, Page 12, the following demands were established in this thesis:

1. Lateral vibrations amplitudes of the field coil array must be less than $10\ \mu m$.
2. Torsional vibrations amplitudes of the mechanical system must be less than $0,1\ mrad$.
3. Spikes of the electrical noise induced into the signal cables must be less than $3\ mV$.
4. The magnet’s power supply ripple must be less than $35ppm$ at $300\ Hz$.
5. During axis measurements heavy loads (i.e. more than a metric ton) must not be moved nearby the measurement area.

All limits prescribed for the field quality measurement are shown in Table 4.2, Page 88. The axis measurement was found to be precise to $0.1\ mm$.

6.2 Assessment procedure

6.2.1 Field quality measurement

The system described in this thesis fulfils the aforementioned requirements. This was shown by the following steps.

1. A computational tool called “Truffaldino” was developed, which allows to simulate all components of the system together with their artefacts.
2. In a special experiment the radial coil array was shaken in a well defined manner. The measurements were compared to the tool’s calculations. Thus, it was proven that it is possible to measure the transversal and torsional vibrations of a radial coil array. They were found to be at least a quarter smaller than acceptable.
3. Using an oscilloscope low and middle range electrical noise was measured and its effect on the magnetic measurement was calculated.
4. Using the tool it was shown that motor vibrations and integrator offsets do not deteriorate the measurement if the standard analysis procedure is used.

6.2.2 Axis measurement

As the axis measurement qualification focuses on other equipment than the measurement of the remaining field parameters it was treated separately from those. The pure magnetic part of the axis measurement needs less precision than the magnetic measurement of the other field parameters. To prove the axis measurement precision the following steps were carried out:

1. During the SSS4 campaign one aperture was scanned four times. Using these data the total reproducibility was calculated to $75\mu m$ at 1σ .
2. During the SSS5 warm measurement campaign the axis was measured with the Antbear and the single stretched wire system (SSW). The difference between these measurements were 0.1 mm for aperture #2 and 0.2 mm for aperture #1. Mechanical works were conducted during the survey of aperture #1 and thus degraded the survey measurement precision. Therefore the 0.1 mm are considered as the accuracy of the measurement. The difference between the

results of the two measurement systems include the long term stability of the cold mass in the cryostat – there were a few months between the two measurements – and the effect of alternating current versus direct current powering of the magnet. (In the Antbear setup the magnet is powered with direct current, and in the SSW the magnet is powered with alternate current.)

Two calibration systems will guarantee the axis measurement precision: A telescope tracker calibration bench was set up to calibrate the lateral parameters and a procedure to verify the straightness of the telescope axis was established.

Bibliography

- [1] Christopher Quigg. *The third Bernard Gregory lectures*. CERN, 1989.
- [2] Arnaud Devred. Magnet systems for large particle accelerators. Internal note, CERN, February 2001.
- [3] D I Kazakov. Beyond the standard model (in search of supersymmetry). In N Ellis and J March-Russell, editors, *2000 European School of High-Energy Physics, Caramulo, Portugal*, pages 125–198. CERN, 2000.
- [4] C Rubbia. Experimental observation of the intermediate vector bosons W^+ , W^- , and Z^0 . In Almqvist and Wiksell, editors, *Les prix Nobel, 1984.*, pages 51–101, 1985.
- [5] Simon van der Meer. Stochastic cooling and the accumulation of antiprotons. In Almqvist and Wiksell, editors, *Les prix Nobel, 1984*, pages 103–122, 1985.
- [6] J. Roosbach and P. Schmüser. Basic course on accelerator optics. In S. Turner, editor, *CAS, 5. General Accelerator Physics course*, number CERN 94-01 I in CERN Accelerator School, pages 17–88, CH-1211 Geneva 23, 1992. CERN, CERN.
- [7] O. Brüning. Field quality requirements. Technical report, CERN, Geneva 23, CH, July 2000.
- [8] Stéphane Fartoukh and Oliver Brüning. Field quality specification for the LHC main dipole magnets. Technical Report LHC Project Report 501, CERN/LHC, CH 1211 - Geneva23, October 2001.
- [9] L. Bottura. private communication, August 2002.
- [10] Lars Nielsen. *Short Straight Section (SSS) types in the arcs from Q13 to Q12*. CERN, 09 1999. EDMS No 103939.

- [11] J Billan and et al. Twin rotating coils for cold magnetic measurements of 15 m long lhc dipoles. *IEEE Trans. Appl. Superconduct.*, pages 1422–6, 2000.
- [12] Reinhard Meinke, Paul Schmüser, and Y. Zaho. Methods of harmonic measurements in the superconducting hera magnets and analysis of systematic errors. Technical report, DESY, September 1991.
- [13] G. Ganetis, J. Herrera, R. Hogue, J. Skarita, P. Wanderer, and E. Willen. Field measuring probe for the SSC magnets. In *Proceedings of the 1987 IEEE Particle Accelerator Conference: Accelerator Engineering and Technology (Cat. No.87CH2387-9), Washington, DC, USA,,* volume 3, pages –2017. IEEE, New York, NY, USA, 1987.
- [14] G. Knies and J. Krzywinski. The DESY Stretched Wire System for magnetic measurements. to be published.
- [15] Zachary Wolf and Pierre Pellissier. Moving wire technique for SSC quadrupole alignment. Technical report, SSC Laboratory, December 1991.
- [16] Nikolay Leonid Smirnov. Private Communication.
- [17] J. DiMarco and Krzywinski J. MTF single stretched wire system. Technical report, Fermi National Accelerator Laboratory, P.O. Box 500, Batavia, Illinois 60510, March 1996.
- [18] N. L. Smirnov. On using the stretched wires method for UNK dipole field direction measurement. Technical report, Protvino Inst. High Energy Phys., 1992.
- [19] J. J. Rabi, J. R. Zacharias, Millman S., and Kusch P. A new method of measuring nuclear magnetic moment. *Phys. Rev.*, page 318, 1938.
- [20] J. J. Rabi, J. R. Zacharias, Millman S., and Kusch P. The molecular beam resonance method for measuring nuclear magnetic moments. *Phys. Rev.*, pages 526–535, 1939.
- [21] F. Bloch, W.W. Hansen, and Packard M. "nuclear induction". *Phys. Rev.*, page 127, 1946.
- [22] F. Bloch, W.W. Hansen, and Packard M. "the nuclear induction experiment". *Phys. Rev.*, pages 474–485, 1946.

- [23] E. M. Purcell, H. C. Torrey, and R. V. Pound. Resonance absorption by nuclear magnetic moments in a solid. *Phys. Rev.*, pages 37–38, 1946.
- [24] E. H. Hall. On a new action of the magnet on electric currents. *Amer. J. Math.*, 2:287–292, 1879.
- [25] J. B. Bergot, Ph. Dambre, L. Nielson, V. Parma, M. Peyrot, T. Renaglia, J. M. Rifflet, P. Rohmig, E. Roy, F. Simon, T. Tortschanoff, and D. Vincent. A modular design for the 56 variants of the short straight section in the arcs of the large hadron collider(LHC). In *7th European Particle Accelerator Conference, Vienna, Austria, 26 - 30 Jun 2000*, pages 2157–2163. European Phys. Soc., Geneva, 2000.
- [26] A. Devred and M. Traveria. Magnetic field and flux of particle accelerator magnets in complex formalism. *not published*, 1994.
- [27] Animesh K. Jain. Harmonic coils. In S. Turner, editor, *CAS Magnetic Measurement and Alignment*, pages 175–217. CERN, August 1998.
- [28] R. A. Beth. Complex representation and computation of two-dimensional magnetic fields. *Applied Physics*, 37:2568–71, 1966.
- [29] M. Genet. Measuring shaft - standard segment ball bearing flanch. LHC DRAWING, december 2000.
- [30] G. Turcato. Description du module electronique "integrateur 32 bits binaires programmable" compatible au bus G64. Note interne, CERN, january 1983.
- [31] P. Galbraith. Portable digital integrator. Technical report, CERN, january 1993.
- [32] P. Zimmerschitt and Christian Glöckner. Abschlußbericht, laserbeam detection system. Technical report, Fraunhofer-Institut für Produktionstechnologie, November 1999. Project-Nr 112 160.
- [33] P. Zimmerschitt and Christian Glöckner. *Laserbeam Detection System*. Fraunhofer-Institut für Produktionstechnologie, Steinbachstraße 17, D-52074 Aachen, November 1999. Project-Nr 112 160.
- [34] Christian Glöckner. private communication, may 2001.
- [35] Elisabetta Ainardi. Magnetic axis measurement in the superconducting quadrupoles in the LHC. Master's thesis, Politecnico di Torino, 1999.

- [36] Luca Bottura. Standard analysis procedures for field quality measurements of the lhc magnets. Technical report, LHC/MTA, July 1997.
- [37] Carlo Goldoni. *Il Servitore di due Padroni*. 1749.
- [38] W. C. Li and M. W. Coles. Systematic error analysis of rotating coil using computer simulation. In P. Hale, editor, *5th International Industrial Symposium on the Super Collider - IISSC, San Francisco, CA, USA, 6 - 8 May 1993*, 1994.
- [39] J. DiMarco and et al. Influence of mechanical vibrations on the field quality measurements of LHC interaction region quadrupole magnets. In *16th International Conference on Magnet Technology (MT-16 1999), Tallahassee, FL, 26 Sept.-2 Oct. 1999*.
- [40] Luca Bottura, Marco Buzio, Pierre Schnizer, and Nikolay Leonid Smirnov. A tool to simulate rotating coil magnetometers. In *17th International Magnet Technology Conference*, Geneva, September 2001.
- [41] Sanjit K. Mitra. *Digital Signal Processing, A computer based approach*. Mc Graw Hill, 1998.
- [42] Joseph DiMarco, H. Glass, J. Krzywinski, P. Schlabach, C. Sylvester, and J.C. Tompkins. Influence of mechanical vibrations on the field quality measurements of lhc interaction region quadrupole magnets. *IEEE-Transactions-on-Applied-Superconductivity (USA)*, 10(1):1458–61, March 2000.
- [43] J. Krzywinski. private communication, February 2002.
- [44] Jean-Pierre Quesnel. LHC global alignment. LHC Seminar on Alignment; HyperText Document at <http://vrd.home.cern.ch/vrd/aplaw/page.html> and <http://vrd.home.cern.ch/vrd/aplaw/talkfiles/quesnel.pdf>, Decembre 2000.
- [45] Michel MAYOUD. Comparative surveys and successive re-alignments : Useful tools and significant estimates. The 22nd Advanced ICFA Beam Dynamics Workshop, November 6-9, 2000, Stanford; HyperText Document at <http://www-project.slac.stanford.edu/lc/wkshp/GM2000/> and http://www-project.slac.stanford.edu/lc/wkshp/GM2000/webtalks/Mayoud_new/, November 2000.

- [46] Michel MAYOUD. LEP/ LHC tunnel (un) stability : LEP/ LHC tunnel (un) stability. LHC Seminar on Alignment, December 5, 2000; HyperText Document at <http://vrd.home.cern.ch/vrd/aplaw/page.html> and <http://vrd.home.cern.ch/vrd/aplaw/talkfiles/mayoud.pdf>, Decembre 2000.
- [47] O. Dunkel. private communication, September 2002.
- [48] Max Born and Emil Wolf. *Principles of Optics*. Pergamon Press, 2 edition, 1964.
- [49] Robert Wichard Pohl. *Optik und Atomphysik*, volume 3. Springer, 10 edition, 1958.
- [50] Sebastien Gonzalve. Calibration of the axis tracker. Technical report, ISIMA, September 2001.
- [51] N. Smirnov. private communication, September 2002.
- [52] Pail Rivoire. *Axyz Training Manual for Trackers*. Leica Geosystems AG, Unterentfelden, Switzerland, October 2000.
- [53] N. L. Smirnov. Results of SSS5 warm magnetic measurements performed with SSW system. Technical report, CERN/LHC-MTA, April 2002.
- [54] Animesh K. Jain. Basic theory of magnets. In S. Turner, editor, *CAS Magnetic Measurement and Alignment*, pages 1–21. CERN, August 1998.
- [55] Alan C. Hindmarsh. ODEPACK, a systematized collection of ode solvers. *scientific computing*, pages 55–64, 1983. r. s. stepleman et al. (eds.), north-holland, amsterdam,.
- [56] Burton S. Garbow, Kenneth E. Hillstrom, and J. Jorge. Minpack. Hypertext document at <http://netlib.org/minpack>.
- [57] Guido van Rossum. Python. Hypertext Document at <http://www.python.org>.
- [58] Mark Lutz. *Programming Python*. O' Reilly and Associates, Sebastopol, october 1996.
- [59] Numerical Python. Hypertext Document at <http://www.pfdubois.com/numpy/>.

- [60] SciPy, scientific tools for Python. Hypertext Document at <http://www.scipy.org/>.
- [61] The Visualisation Toolkit. Hypertext Document at <http://www.kitware.com/>.
- [62] Will Schroeder, Ken Martin, and Bill Lorensen. *The Visualisation Toolkit*. Prentice Hall PTR, 2 edition, 1998.
- [63] Linda R. Petzold. automatic selection of methods for solving stiff and nonstiff systems of ordinary differential equations. *siam j. sci. stat. comput*, 4:136–148, 1983.
- [64] W. Scandale. private communication, December 2001.

Appendix A

Derivation of formulas

A.1 Effect of mechanical coil imperfections on the measurement

Accelerator magnets can be described as axial fields. Their magnetic field \mathbf{B} can be expanded in a series as follows

$$\mathbf{B}(\mathbf{z}) = B_y + iB_x = \sum_{n=1}^{\infty} [B_n + iA_n] \left(\frac{\mathbf{z}}{R_{Ref}} \right)^{(n-1)} \quad (\text{A.1})$$

where $B_n + iA_n = C_n$ [54] are the multipole components, and \mathbf{z} the transverse position. As the European convention is used here, C_1 is the strength of the dipole. The flux Φ seen by a rotating coil is given as [27]

$$\Phi(t) = \sum_{n=1}^M \mathbf{K}'_n(\mathbf{t}) C_n(\mathbf{t}) \exp[in\theta(t)]. \quad (\text{A.2})$$

M is the last harmonic taken into account, θ is the angular position. The sensitivity of a coil is given by

$$\mathbf{K}_n = \underbrace{\left(\frac{N_w L R_{Ref}}{n} \right)}_{\mathbf{K}_{const}} \underbrace{\left[\left(\frac{\mathbf{z}_2}{R_{Ref}} \right)^n - \left(\frac{\mathbf{z}_1}{R_{Ref}} \right)^n \right]}_{\mathbf{K}_t}, \quad (\text{A.3})$$

In the following the first factor of Equation (A.3) is set to

$$\mathbf{K}_{const} = \frac{N_w L R_{Ref}}{n}$$

and the second factor to \mathbf{K}_t .

A.1.1 Lateral displacements in a quadrupole field.

To allow a correct measurement of the harmonics the axis of rotation must be stable. In the following formulas are derived describing the spurious harmonics generated by an unstable revolution. A formalism is developed which describes the effect of an unstable motion $D(\theta')$. The sensitivity K_t is given as

$$K_t = [z_2 \exp(i\theta') + D(\theta')]^n - [z_1 \exp(i\theta') + D(\theta')]^n, \quad (A.4)$$

and the flux $\Phi(\theta')$ is given as

$$\Phi(\theta') = Re \left\{ \sum_{n=1}^{\infty} \frac{N_w L}{n R_{Ref}^{n-1}} [z_2 \exp(i\theta') + D(\theta')]^n - [z_1 \exp(i\theta') + D(\theta')]^n \right\}. \quad (A.5)$$

In a pure quadrupole field the flux is given as

$$\Phi(\theta') = Re \left[\frac{NL}{2R_{Ref}} (z_2^2 - z_1^2) C_2 e^{i2\theta'} \right] + \left[(z_2 - z_1) \frac{D(\theta')}{R_{Ref}} C_2 e^{i\theta'} \right]. \quad (A.6)$$

Introducing the coil sensitivities as given in (2.16) one gets

$$\Phi(\theta') = Re \left[K_2 C_2 e^{i2\theta'} + K_1 \frac{D(\theta')}{R_{Ref}} C_2 e^{i\theta'} \right]. \quad (A.7)$$

Equation A.7 shows that in a pure quadrupole field, the flux picked up by a rotating coil is distorted by transverse displacements of the rotation axis, and the distortion is proportional to the sensitivity of the factor of K_1 .

Case of a periodic displacement of the axis

For periodic displacements one can describe $D(\theta')$ as

$$D(\theta') = \sum_{q=-\infty}^{\infty} D_q e^{iq\theta'}. \quad (A.8)$$

Then $D(\theta') \exp(i\theta')$ can be written as

$$D(\theta') e^{i\theta'} = \sum_{q=0}^{\infty} D_q e^{i(q+1)\theta'} + D_{-1} + \sum_{q=2}^{\infty} D_{-q} e^{-i(q-1)\theta'}. \quad (A.9)$$

Using Equation (A.7) and (A.8) one can write the flux as

$$\begin{aligned} \Phi(\theta') &= Re[K_2 C_2 e^{i2\theta'}] + Re \left\{ \sum_{q=0}^{\infty} \frac{D_q}{R_{Ref}} C_2 e^{i(q+1)\theta'} \right\} \\ &+ Re \left[K_1 \frac{D_{-1}}{R_{Ref}} C_2 \right] + Re \left\{ \sum_{q=2}^{\infty} \frac{D_{-q}}{R_{Ref}} C_2 e^{-i(q-1)\theta'} \right\}. \end{aligned} \quad (A.10)$$

Defining a constant

$$const = Re \left[\mathbf{K}_1 \frac{\mathbf{D}_{-1}}{R_{Ref}} \mathbf{C}_2 \right] \quad (\text{A.11})$$

and using

$$Re \left\{ \mathbf{K}_1 \frac{\mathbf{D}_{-q}}{R_{Ref}} \mathbf{C}_2 e^{-i(q-1)\theta'} \right\} = Re \left\{ \overline{\mathbf{K}_1} \frac{\overline{\mathbf{D}_{-q}}}{R_{Ref}} \overline{\mathbf{C}_2} e^{-i(q-1)\theta'} \right\}, \quad (\text{A.12})$$

one can rewrite (A.10) as

$$\Phi(\theta') = Re[\mathbf{K}_2 \mathbf{C}_2 e^{i2\theta'}] + Re \left[\sum_{q=1}^{\infty} \mathbf{K}_q \mathbf{C}_q^s e^{iq\theta'} \right] + const, \quad (\text{A.13})$$

with \mathbf{C}_q^s

$$\mathbf{C}_q^s = \frac{\mathbf{K}_1}{\mathbf{K}_q} \frac{\mathbf{D}_{q-1}}{R_{Ref}} \mathbf{C}_2 + \frac{\overline{\mathbf{K}_1}}{\mathbf{K}_q} \frac{\overline{\mathbf{D}_{-q-1}}}{R_{Ref}} \overline{\mathbf{C}_2}. \quad (\text{A.14})$$

In Equation (A.13) the first term resembles the ideal flux induced by a quadrupole as in Equation (2.15). The second term can be seen as the influence of the spurious harmonic (A.14). It is proportional to the dipole sensitivity.

A.1.2 Lateral Displacements in a pure n-pole field

In a pure n-pole field only the terms of order n are non-zero in Equation (A.5). The flux is then given as

$$\Phi(\theta') = Re \left\{ \mathbf{K}_n \mathbf{C}_n e^{in\theta'} + \sum_{p=1}^{n-1} \binom{n-1}{p} \mathbf{K}_{n-p} \left[\frac{\mathbf{D}(\theta')}{R_{Ref}} \right]^p \mathbf{C}_n e^{i(n-p)\theta'} \right\}. \quad (\text{A.15})$$

From the above equation one can see that for a n-pole field (with $n \geq 2$) the spurious harmonics induced by a lateral coil displacement of the rotation axis are proportional to the sensitivity factors of the orders lower than $n - 1$.

A.1.3 Shaft torsional vibrations / angular encoder incorrect triggering

The angular encoder is supposed to measure the angle of the magnetic coil versus time. For considering a vibration of type $\theta' = \theta_a + T(\theta_a)$ between the coil and the angular encoder, where θ_a is the reading of the angular encoder, one sets \mathbf{K}_t to [26]

$$\mathbf{K}_t = \mathbf{z}_2 \exp[inT(\theta_a)] \exp(i\theta_a) - \mathbf{z}_1 \exp[inT(\theta_a)] \exp(i\theta_a). \quad (\text{A.16})$$

One can develop $\exp [inT(\theta_a)]$ into

$$1 + \sum_{p=1}^{\infty} \frac{[inT(\theta_a)]^p}{p}. \quad (\text{A.17})$$

Putting this into Equation (2.33) one can rewrite it to

$$\Phi(t) = Re \left[\mathbf{K}_n \mathbf{C}_n e^{\theta_a} \right] + Re \left\{ n \mathbf{K}_n \left(\sum_{p=1}^{\infty} \frac{[inT(\theta_a)]^p}{p} \right) \mathbf{C}_n e^{\theta_a} \right\}. \quad (\text{A.18})$$

The first term is the ideal signal whereas the second describes the signal due to this torsional vibration. For small angles one can approximate

$$1 + \sum_{p=1}^{\infty} \frac{[inT(\theta_a)]^p}{p} \approx 1 + inT(\theta_a). \quad (\text{A.19})$$

One can then rewrite the second term of the flux (A.18) to

$$n \mathbf{K}_n T(\theta_a) i \mathbf{C}_n \exp(in\theta_a). \quad (\text{A.20})$$

If $T(\theta_a)$ is a periodic function it can be written as a Fourier series

$$T(\theta_a) = \sum_{q=-\infty}^{\infty} \mathbf{T}_q \exp(iq\theta_a). \quad (\text{A.21})$$

$T(\theta_a) \exp(in\theta_a)$ can then be written as

$$\begin{aligned} T(\theta_a) \exp(in\theta_a) = & \sum_{q=-(n-1)}^{\infty} \mathbf{T}_q \exp[i(q+n)\theta_a] \\ & + T_{-n} + \sum_{q=-(n-1)}^{\infty} \mathbf{T}_{-q} \exp[-i(q-n)\theta_a]. \end{aligned} \quad (\text{A.22})$$

Combining Equation (A.18) and Equation (A.20) with Equation (A.22) one gets for the flux $\Phi(\theta_a)$

$$\begin{aligned} \Phi(\theta_a) \approx & Re \left[\mathbf{K}_n \mathbf{C}_n e^{in\theta_a} \right] + Re \left\{ \sum_{q=-(n-1)}^{\infty} \mathbf{K}_n \mathbf{T}_q i \mathbf{C}_n e^{i(q+n)\theta_a} \right\} \\ & + Re[n \mathbf{K}_n \mathbf{T}_{-n} i \mathbf{C}_n] + Re \left\{ \sum_{q=n+1}^{\infty} \mathbf{K}_n \mathbf{T}_{-q} i \mathbf{C}_n e^{-i(q-n)\theta_a} \right\} \end{aligned} \quad (\text{A.23})$$

Defining *const* as

$$const = Re[n \mathbf{K}_n \mathbf{T}_{-n} i \mathbf{C}_n] \quad (\text{A.24})$$

and using

$$Re \left\{ \sum_{q=n+1}^{\infty} \mathbf{K}_n \mathbf{T}_{-q} \mathbf{i} \mathbf{C}_n \cdot e^{-\mathbf{i}(q-n)\theta_a} \right\} = -Re \left\{ \sum_{q=n+1}^{\infty} n \overline{\mathbf{K}_n} \overline{\mathbf{T}_{-q}} \mathbf{i} \mathbf{C}_n \cdot e^{-\mathbf{i}(q-n)\theta_a} \right\} \quad (\text{A.25})$$

one can rewrite Equation (A.24) as

$$\Phi(\theta_a) \approx Re \left[\mathbf{K}_n \mathbf{C}_n e^{\mathbf{i}n\theta_a} \right] + Re \left\{ \sum_{q=1}^{\infty} \mathbf{K}_q \mathbf{T}_q \mathbf{i} \mathbf{C}_q^s \cdot e^{\mathbf{i}q\theta_a} \right\} + const, \quad (\text{A.26})$$

with C_q^s :

$$\mathbf{C}_q^s = \frac{n\mathbf{K}_n}{\mathbf{K}_q} \mathbf{T}_{q-n} \mathbf{i} \mathbf{C}_n - \frac{n\overline{\mathbf{K}_n}}{\overline{\mathbf{K}_q}} \overline{\mathbf{T}_{-q-n}} \mathbf{i} \overline{\mathbf{C}_n}. \quad (\text{A.27})$$

C_q^s can be interpreted as a spurious harmonic due to angular shifts between the angle measured by the angular encoder and the angle of the magnetic probe in a pure $2n$ field. It is proportional to the sensitivity \mathbf{K}_n to the n^{th} harmonic.

A.1.4 Summary

The formulae for spurious harmonics generated by mechanical imperfections were derived. Transversal vibrations of the coil generate spurious harmonics proportional to the dipole sensitivity of the coil array \mathbf{K}_1 . Torsional vibrations of the coil generate spurious harmonics proportional to the quadrupole sensitivity \mathbf{K}_2 .

Appendix B

Truffaldino - A tool for simulating rotating coil systems

A simulation tool (see Chapter 4) was created for the field measurement qualification, which allows to calculate the physical value of each parameter of the system. It is based on first principles. Due to its object oriented hierarchy, a simple system set up is possible tailored to the individual needs of the application. Each object resembles to one real device. The characteristic can be adjusted using its methods so that it characterises a device without any imperfections or it exhibits some artefact. The simulation includes the analysis, so one can conclude how a given artefact effects the multipole measurement.

In this chapter first the target of the simulation is discussed. Then the possible mathematical approaches will be shown followed by a discussion of the system layout and the internal communication and calculation.

B.1 Motivation - Targets

While searching for the source of errors (e.g. electrical noise, imperfection of the rotation of the coils, spurious marks in the angular encoder) in rotating coil magnetometers one can see that different malfunctioning components can produce similar effects. An analytical treatment of nearly any effect is available and only perfect magnets are considered. Considering more than one effect renders the analysis nearly impracticable. So the effort was started to implement a tool to simulate the described measurement system in here.

B.2 Implementation details

In Chapter 2 the flux through a coil was derived and its multipole representation was given and in Section 3.7 the analytic procedure was described. The whole measurement task can be put together in one formula

$$\Phi'(t) = \underbrace{\int_{f^{-1}(\theta'_0)}^{f^{-1}(\theta'_0+2\pi)} g \left(\underbrace{\underbrace{\operatorname{Re} \left[-\frac{d}{dt'} \sum_{n=1}^{\infty} \underbrace{\{ \mathbf{K}_n(t') \mathbf{C}_n(t') e^{in\theta(t')} \}}_{\text{coil's flux}} \right]}_{\text{coil's signal}}, t \right)}_{\text{amplifier}} dt'}_{\text{integrator}}, \quad (\text{B.1})$$

with $\Phi'(t)$ the output of the integrator, $f(t)$ the function describing the angular encoder measurement at the instant t (and $f^{-1}(\theta') = t$), K_n the sensitivities of the coil, C_n the multipoles of the magnet, $\theta(t)$ the angle of the coil, $\dot{\theta}(t)$, its rotations speed, and $g()$ the function describing the preamplifier. (For compensated system one has to add an additional sum over all involved coils: So instead of $\mathbf{K}_n(t') \mathbf{C}_n(t') e^{in\theta(t')}$ one has to use $\sum_m \mathbf{K}_n(t') \mathbf{C}_n(t') e^{in\theta(t')}$, with m the number of coils.) The above formula is shown not to explain the measurement system (which was outlined in Chapter 3), but to aid the following discussion. Equation (B.1) illustrates two different view points of the signal flow:

- *The time domain:* The coil angle and speed depends on time, the integrator integrates the signal versus time, the angular encoder sends the trigger impulses at a certain instant. So the normal measurement system operation is time dependent.
- *The frequency domain:* The field calculation yields the magnet data versus its multipoles. The flux seen by the coil is described as a sum of multipoles, which can be seen as a function of n . Electrical noise and imperfections of the power supply are related to frequencies. So one could try to calculate everything in frequency space.

But practical details have to be considered:

- In the time domain the voltage of every component is summed up. As the higher order harmonics are typically $10^{-4} - 10^{-5}$ smaller than the main harmonics, one loses 5 digits of precision for the higher order harmonics.
- In frequency domain each device would act on the frequency spectrum computed by the previous device. However a lot of frequencies are needed to calculate the effect of any discontinuity, e.g. a missing mark of the angular encoder. Further, the representation of each device is not straightforward.

The precision issue of the time space is solvable using 8 bytes real numbers. As the components are simpler to implement in their time dependence, the time space was favoured over the frequency space.

Analytical treatment of any problem yields deeper understanding of its nature. An analytic approach would be preferable considering the availability of powerful packages allowing symbolic calculations. But Equation (B.1) includes two pitfalls for an analytical approach:

- The integral: Integrands can need elaborate means: There are no rules how products of integrands can be solved, even if each part can be treated.
- The angular encoder treatment: Normally the angular encoder and its implementation give a certain angle depending on its position. In Equation (B.1) one can see that the angular encoder is used to determine a certain angle at the instant t . For that reason the function describing the angular encoder's behaviour must be inverted. This function has to describe missing marks or periodic shifted marks, which can be difficult to invert.

Therefore numerical solutions were chosen using numerical solvers for the above problem.

The aforementioned formula showed the flux through the coil in its multipole presentation. One could describe the flux as a two dimensional property $\Phi(\mathbf{z} = x + iy)$. For accelerator magnets the multipole scheme was adopted, as they typically possess one dominant multipole; the other multipoles are used to describe the magnet errors. Further, the coil's calibration yield multipoles. Choosing the multipole representation in the internal calculations allows simple data exchange between the simulation and the measurement.

All issues of Equation (B.1) have been settled except the derivative $\frac{d}{dt} \{ \dots \}$. Previous codes [42, 38] used a numeric differentiation scheme. Here the favour was given to analytic expressions for the derivative of the coil, though this approach is more complex to implement, as this simulation has to integrate the signal. Therefore the computational load is reduced compared to that of a pure numerical approach.

To summarise the following approach was taken:

- The calculation will be performed in the time domain.
- The integration and function inversion will be done numerically.
- All other items should be implemented analytically.

B.2.1 Computational aspects

As stated above numerical accuracy better than a few ppm is required in the simulation for the integrator. Therefore the different available methods of integration were tested:

- Simple summing of the signal
- Romberg's method
- Ordinary Differential Equation solvers (ODEPACK [55]).

It was found that ODEPACK provided reliable routines using an acceptable number of function evaluations, whereas the other two methods needed more evaluations for the same precision. Therefore “lsoda” from ODEPACK was used as an integrator and the root finding routine “hybrid” from the MINPACK [56] for inverting the angular encoder function.

As already shown in Section 4.1 the system is based on an object oriented hierarchy. All input is described by objects. Each object presents the output signal on one common standard method. Calling it with a value for t it will evaluate itself and all its inputs, which resemble the right hand side of Equation (B.1). The language “Python” was chosen [57, 58] as it allows rapid development while offering many scientific oriented capabilities e.g. arrays or numerical packages [59, 60]. Even in this byte compiled language run times of a few seconds for one typical run are feasible on a modestly modern PC Hardware (Pentium III 600 Mhz).

B.3 The user's interface

The key architecture is an object oriented hierarchy organised as a pipeline. Similar implementations are found for graphics processing [61, 62]. Each device is described by an object. To perform calculations all objects have to be set up and have to be connected accordingly. A real and an ideal implementation exist for every device. The ideal one is implemented as simple as possible and therefore often faster in the calculation. The real one allows to treat artefacts. They are interchangeable in the calculation pipeline (See Figure B.1 and Figure B.6) as their interfaces are interchangeable. Typically one starts to set up one system up using only the ideal components. After a check that the system calculates correctly, one replaces the ideal with the real implementation for those devices, whose artefacts should be treated. In the following an example is described how to study the effect of a transversally vibrating coil array. The object relation will be illustrated next to the corresponding code. Even if one is not familiar with the Python programming language one will be able to catch the main concept.

The first step is to set up the objects: First the power supply is set up. Here an idealised power supply is used delivering constant current (see also Figure B.3):

```
powersupply = Powersupply.IdealPowerSupply(5000)
```

The magnet setup needs a few steps (See also Figure B.4). To hide the implementation details of the harmonics first an object taking the normalised harmonics and the quadrupole transfer function (assuming a strength of 223 T/m at a current of 13000 A) and all non main harmonics equal to zero is set up:

```
q = 223. / 13000. * Config.ReferenceRadius
nharmonic=Magnet.NormalizedHarmonics(q, [0, 1, 0] + [0] * 2 + [0] +
                                         [0] * 8 + [0])
```

This data is fed to the magnet:

```
magnet = Magnet.IdealMagnet(nharmonic)
```

Similarly the motor, angular encoder and shaft are set up (see Figure B.5):

```
motor = Motor.IdealMotor(Numeric.pi)
shaft = Shaft.IdealShaft()
angularencoder = Angularencoder.IdealAngularencoder()
```

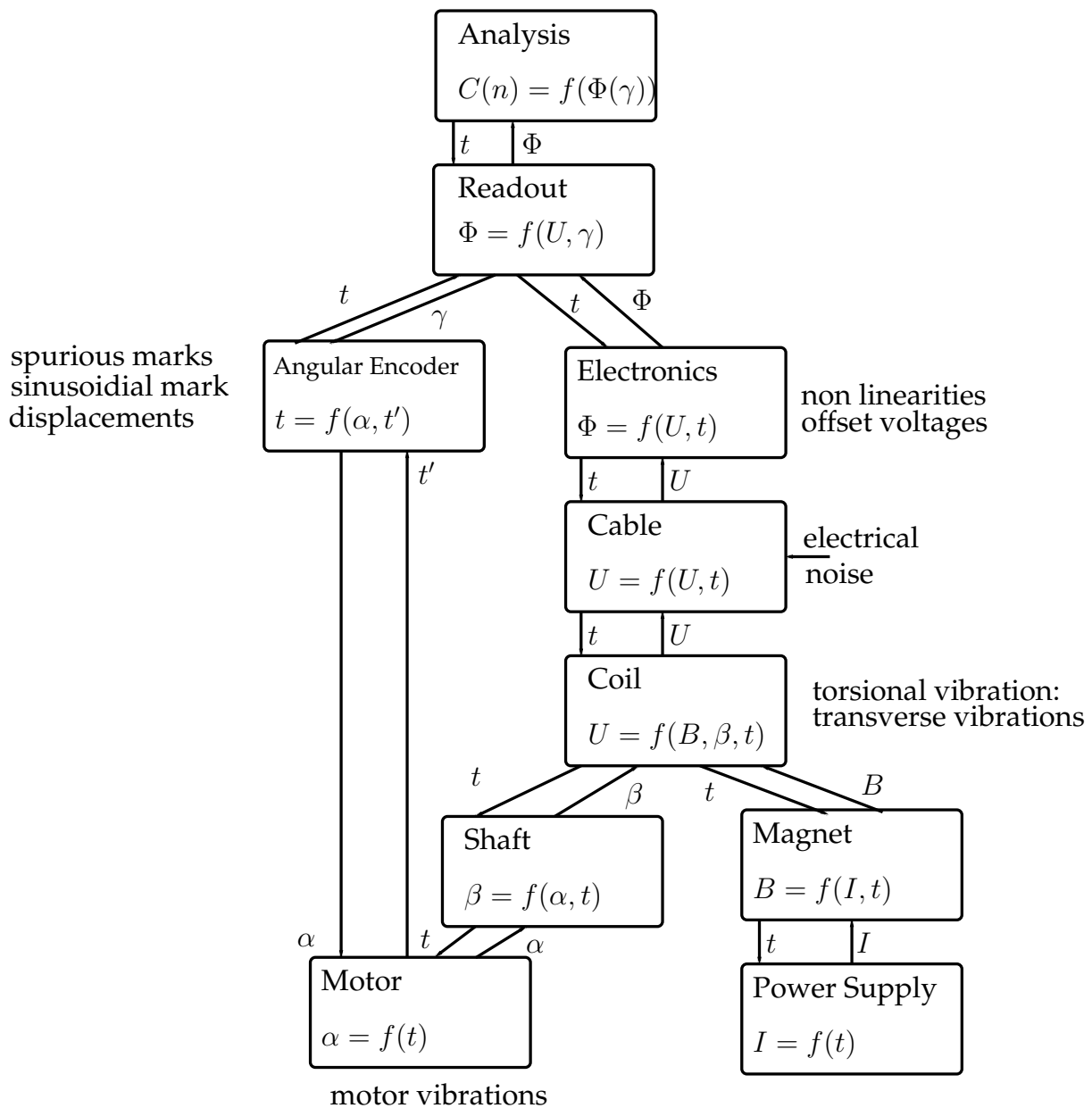



Figure B.1: Sketch of the code. The lines indicate the communication between the modules and the parameters - the communicated variables. All components treat t as the independent variable. Each component has one or more settings. During the calculation the request is passed from the top to the bottom. Each component computes the status at that instant.

For the coil the slang which is in use at LHC is accepted, “coil” describes one coil, and “sector” denotes a coil array. As the voltage induced in the coils is implemented in the “sector” one always needs a sector. So for one single coil a sector with only one coil is used.

The coil needs information about its sensitivities (here it is the sensitivity of coil


```

2.541814e-12 + 8.634142e-15j ,
3.940512e-14 + 1.459656e-16j ,
6.162054e-16 + 2.487606e-18j ,
9.710818e-18 + 4.262143e-20j ,
1.540864e-19 + 7.327539e-22j ,
2.45982e-21 + 1.262409e-23j ,
3.94784e-23 + 2.177539e-25j ,
6.365803e-25 + 3.758321e-27j ,
1.030711e-26 + 6.487964e-29j
), Numeric.Complex)
coil.SetSensitivity(sensitivity)
coil.SetNumberOfFactors(15)
sector = Sector.SectorWithUnregularPath.FlatterSector((coil,))
amplitude = Numeric.array((1e-6 + 2e-6j,))
freq = Numeric.array((2.0,))
phase = Numeric.array((0.0,))
mo = Utils.FourierSeries.FourierSeries(freq, amplitude, phase)
sector.SetMotionObject(mo)

```

Here not the ideal sector but a “Flatter Sector” is used, the movement of the sector versus its angle has to be specified. The movement is described as a Fourier series of $z(\theta)$ with $z = x + iy$. With the above parameter the axis of the “sector” object moves vertically with $y = 2 \cdot 10^{-6} \cdot \sin(2 \cdot \theta(t))$ and horizontally with $x = 1 \cdot 10^{-6} \cdot \sin(2 \cdot \theta(t))$. The “SetMotionObject” method accepts any object providing an “eval” and a “diff” method with the same signature as the Fourier series objects.

Cable objects are provided to allow the input of electrical noise. The amplifier uses the routine “lsodar” from ODEPACK [55, 63]. The setup is straightforward:

```

cable = Cable.IdealCable()
integrator = Integrator.IdealIntegrator()
electronics = Electronics.IdealElectronics(integrator)
readout = ReadOut.IdealReadOut()

```

The electronics object handles the conversion from analogue to digital data. The last object to be set up is the readout, which calculates the time for the trigger impulses and the evaluation of the magnetic measurement system. In the real system this object is part of the integrator, which receives triggers from the angular encoder and passes its status to the external controller. Now a set of objects were generated

which need to be connected to get the flow diagram shown in Figure B.1:

```
angularenco d e r . S e t M o t o r ( m o t o r )
readout . S e t A n g u l a r e n c o d e r ( a n g u l a r e n c o d e r )

magnet . S e t P o w e r S u p p l y ( p o w e r s u p p l y )
shaft . S e t M o t o r ( m o t o r )
sector . S e t T u r n e r ( s h a f t )
sector . S e t M a g n e t ( m a g n e t )
cable . S e t I n p u t ( s e c t o r )
electronics . S e t I n p u t ( c a b l e )
readout . S e t E l e c t r o n i c s ( e l e c t r o n i c s )
```

The final setup and the setup methods are given in Figure B.6.

Now the calculation can start:

```
length = 256
dataangle = Numeric.arange(length + 1) * 2 * Numeric.pi / length
time , angle , signal = readout.CalculateWithAngle(dataangle)
```

In the first line the number of requested readouts is set. This is followed by the generation of the appropriate angles. Please note that one more angle than requested readouts has to be generated. Typically the first and the last angle will be the same modulo 2π which corresponds to one exact revolution. (But one may want to simulate an inexact revolution.) The readout will evaluate the whole structure and respond with three vectors of length “length” (256 in this case). They correspond to the status of the system at $angle_2$ to $angle_{length}$. These vectors are:

- the time: The points in time at which a certain data angle was reached.
- the angle: The angle the angular encoder showed for each moment.
- the signal: The output of the coil and the electronics chain.

The standard analysis follows the following steps:

```
fluxanalysis = Analysis.FluxAnalysis()
harmonicanalysis = Analysis.HarmonicAnalysisAtReferenceRadius(
    readout)
```

The harmonics analysis needs to scale the flux spectrum by the sensitivities of the coil. Therefore the readout object has to be passed to the harmonic analysis. The

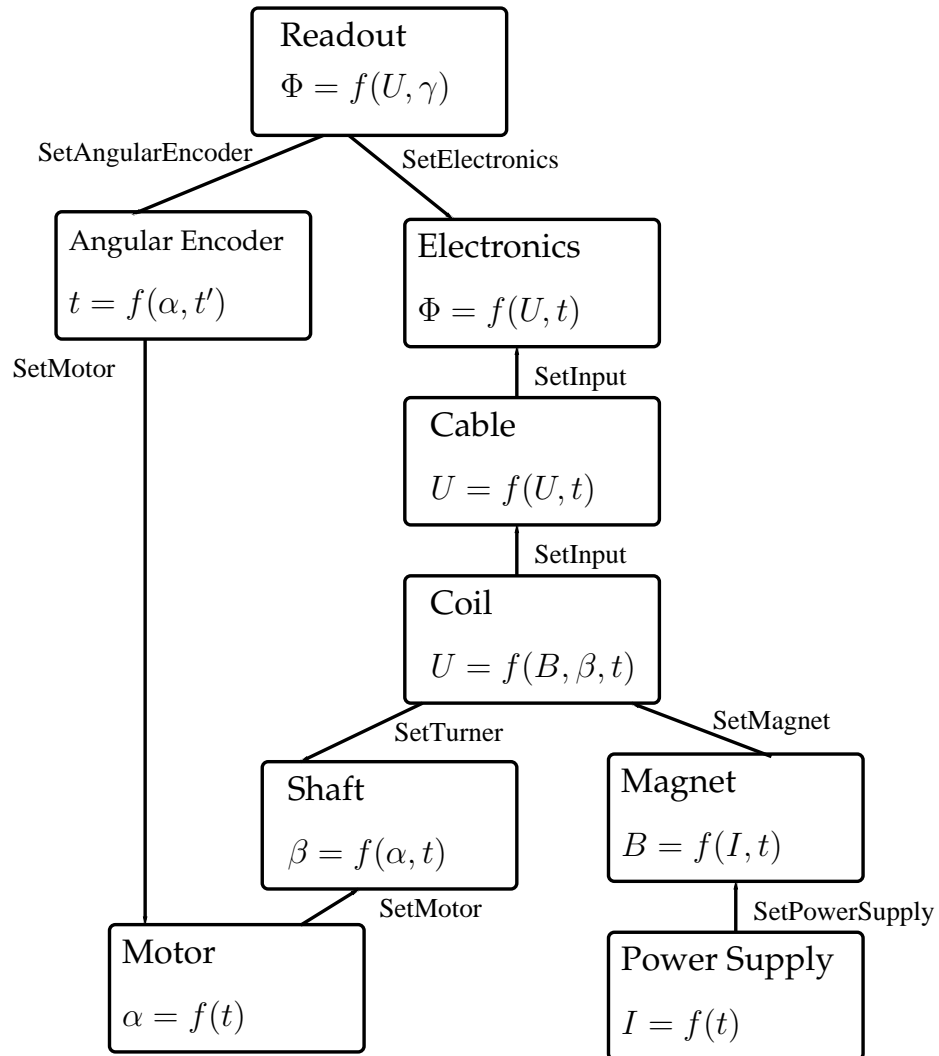


Figure B.6: Sketch of the Code. At each line the methods to register the dependent object are noted.

object “HarmonicAnalysisAtReferenceRadius” returns the harmonics value in units of Tesla at reference radius. After connecting the objects any object can be evaluated to get its status at a moment t . I illustrate it here for three objects:

```

offset = mo.eval(angle)
timev , voltage = sector(time1)
timecounts , fluxcounts = electronics(time1)

```

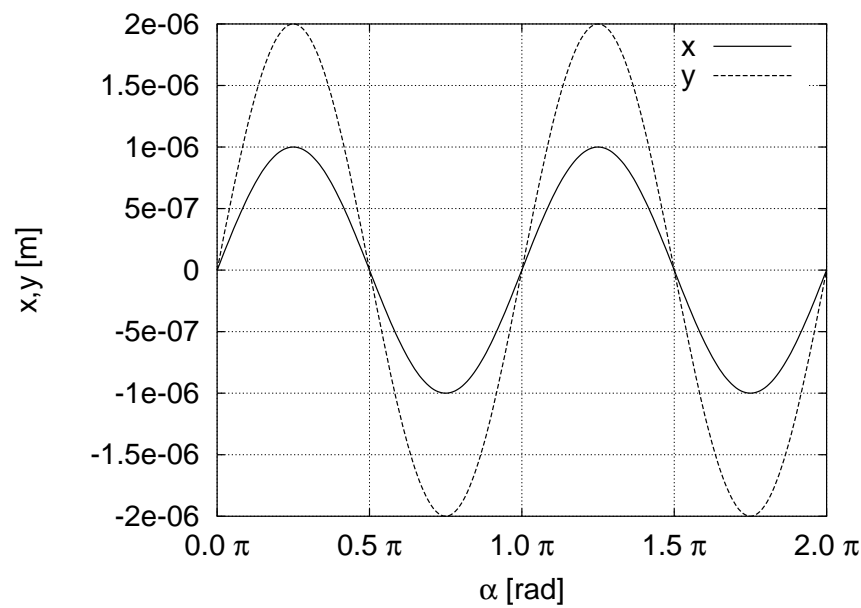


Figure B.7: The Motion Object: The elongation x, y (in Millimetre) versus is plotted the angular position of the coil α (in radians).

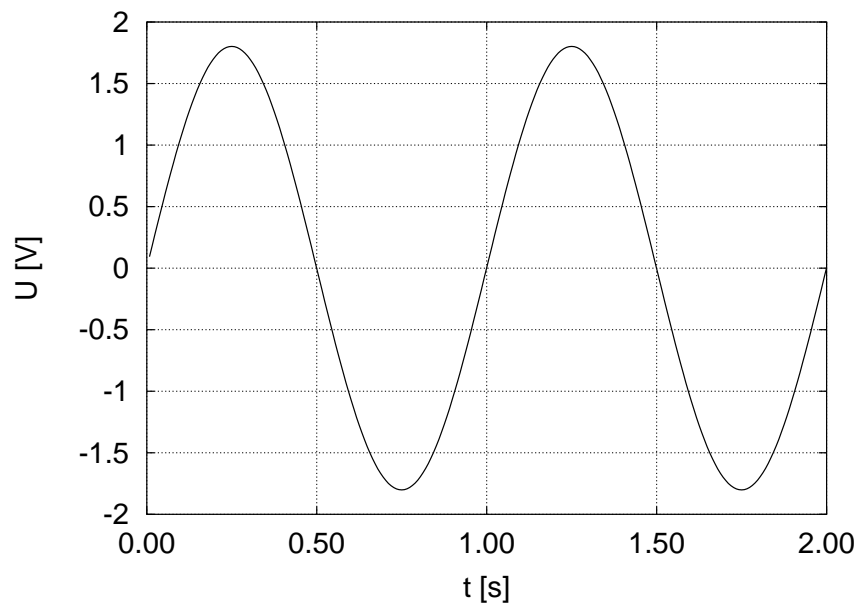


Figure B.8: The Sector Object: The voltage U (in Volts) induced in the sector versus time t (in Seconds) is indicated by the solid line.

For the offset a complex notation is used with $z = x + iy$. The output of the calculation is shown in Figure B.7. In Figure B.8 the output of the sector is visible. One can see the sinusoidal shape. The double period is due to the quadrupole. For the eye the influence of the vibration is not visible. The electronics object reassemble

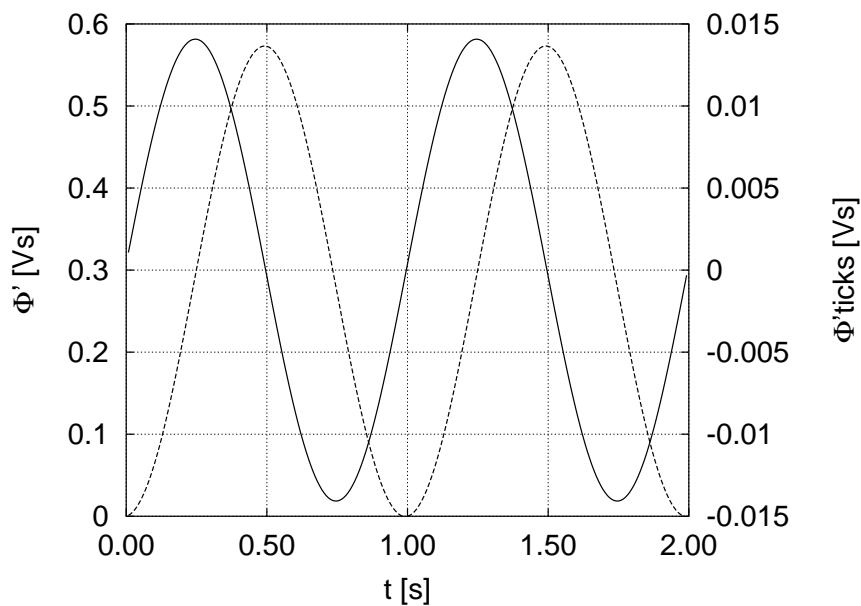


Figure B.9: The Electronics Object: The integrated flux Φ' (in Volt Seconds) is plotted versus time t (in Seconds). The integrator generates ticks from one step to the next. These values are shown by the dashed line on the right hand scale.

the electronics used at the LHC site. They integrate from $angle_i$ to $angle_{i+1}$ and then start from zero again. In Figure B.9 these so called counts are shown by the dashed curve and the scale on the right. The solid line shows these summation on the left curve. From these data the multipoles can be calculated.

In this section I have shown how to use the tool. First one has to set up the individual components. These components are connected to each other. After that each component can be evaluated by itself to get its output. To simulate the result of the total measurement system the “readout” object has to be evaluated.

B.3.1 The total code of the example

```

1 #!/usr/bin/env python
2
3 import Numeric
4 import MLab
5 import Gnuplot
6
7 import MTALib
8 from Truffaldino import *
9

```

```

10 g = Gnuplot.Gnuplot()
11 g("set grid")
12 g("set data style line")
13
14 #-----
15 #Setup of individual Components:
16 powersupply = Powersupply.IdealPowerSupply(5000)
17
18 q = 223. / 13000. * Config.ReferenceRadius
19 nharmonic=Magnet.NormalizedHarmonics(q, [0, 1, 0] + [0] *2 + [0] +
20                                     [0] * 8 + [0])
21 magnet = Magnet.IdealMagnet(nharmonic)
22 motor = Motor.IdealMotor(Numeric.pi)
23 shaft = Shaft.IdealShaft()
24 angularencoeder = Angularencoeder.IdealAngularencoeder()
25 coil = Sector.GenericCoil.GenericCoil()
26 sensitivity = Numeric.array((0.2315893 + 0.0005789744j ,
27                               0.003343223 + 8.358074e-06j ,
28                               4.893152e-05 + 1.256729e-07j ,
29                               7.256837e-07 + 1.959029e-09j ,
30                               1.08973e-08 + 3.145675e-11j ,
31                               1.655476e-10 + 5.167999e-13j ,
32                               2.541814e-12 + 8.634142e-15j ,
33                               3.940512e-14 + 1.459656e-16j ,
34                               6.162054e-16 + 2.487606e-18j ,
35                               9.710818e-18 + 4.262143e-20j ,
36                               1.540864e-19 + 7.327539e-22j ,
37                               2.45982e-21 + 1.262409e-23j ,
38                               3.94784e-23 + 2.177539e-25j ,
39                               6.365803e-25 + 3.758321e-27j ,
40                               1.030711e-26 + 6.487964e-29j
41                               ),Numeric.Complex)
42 coil.SetSensitivity(sensitivity)
43 coil.SetNumberOfFactors(15)
44 sector = Sector.SectorWithUnregularPath.FlatterSector((coil,))
45 amplitude = Numeric.array((1e-6 + 2e-6j,))
46 freq = Numeric.array((2.0,))
47 phase = Numeric.array((0.0,))
48 mo = Utils.FourierSeries.FourierSeries(freq, amplitude, phase)
49 sector.SetMotionObject(mo)
50 cable = Cable.IdealCable()
51 integrator = Integrator.IdealIntegrator()

```



```

52 electronics = Electronics.IdealElectronics(integrator)
53 readout      = ReadOut.IdealReadOut()
54
55 #-----
56 #Connection of the components
57 angularenCoder.SetMotor(motor)
58 readout.SetAngularenCoder(angularenCoder)
59
60 magnet.SetPowerSupply(powersupply)
61 shaft.SetMotor(motor)
62 sector.SetTurner(shaft)
63 sector.SetMagnet(magnet)
64 cable.SetInput(sector)
65 electronics.SetInput(cable)
66 readout.SetElectronics(electronics)
67
68 #-----
69 #Calculation of the signals
70 length = 256
71 dataangle = Numeric.arange(length + 1) * 2 * Numeric.pi / length
72 time, angle, signal = readout.CalculateWithAngle(dataangle)
73
74 #Setup of the analysis
75 fluxanalysis = Analysis.FluxAnalysis()
76 harmonicanalysis = Analysis.HarmonicAnalysisAtReferenceRadius(readout)
77 notused, flux1 = fluxanalysis(time, signal)
78 harmonics = harmonicanalysis(flux1)
79
80 #Print the harmonics:
81 print "# Harmonics at Reference Radius"
82 print "# N      B      + A j "
83 Analysis.PrintHarmonics(harmonics)
84
85 # Plot the output of the different components:
86 # The readout gives us the integrator counts and time counts,
87 # so I add the time counts to get the seconds:
88 time1 = Numeric.add.accumulate(time)
89 # The motion object
90
91
92 command = ""
93 set_xlabel '{/Symbol a} [rad]'

```

```

94 set ylabel 'x,y [m]'
95 set xtics 0.5*pi
96 set xrange [0:2*pi]
97 set format x '%2.1P {/Symbol p}'
98 ""
99 g(command)
100 g.plot(Gnuplot.Data(angle, mo.eval(angle).real, title='x',
101                    with='line lw 2'),
102        Gnuplot.Data(angle, mo.eval(angle).imag, title='y',
103                    with='line lw 2')
104    )
105 g.hardcopy('FlatterSectorMotion.eps', mode='eps', fontsize=24)
106
107 command = ""
108 set format x '%3.2f'
109 set xlabel 't [s]'
110 set xtics auto
111 set xrange[0:2]
112 set ylabel 'U [V]'
113 ""
114 g(command)
115 # The sector:
116 timev, voltage= sector(time1)
117 g.plot(Gnuplot.Data(timev, voltage, with='line lw 2')
118    )
119 g.hardcopy('FlatterSectorVoltage.eps', mode='eps', fontsize=24)
120
121 # The electronics / integrator
122 command = ""
123 set ylabel "{/Symbol F}' [Vs]"
124 set ytics nomirror
125 set y2tics
126 set y2label "{/Symbol F}' ticks [Vs]"
127 set y2range [-0.015:0.015]
128 set yrange [0:.6]
129 ""
130 g(command)
131
132 timecounts, fluxcounts = electronics(time1)
133 g.plot(Gnuplot.Data(Numeric.add.accumulate(timecounts),
134                    fluxcounts, with='line lw 2', axes='x1y2'),
135    Gnuplot.Data(Numeric.add.accumulate(timecounts),

```

```

136         Numeric.add.accumulate(fluxcounts),
137         with='line lw 2', axes='x1y1')
138     )
139 g.hardcopy('FlatterSectorElectronics.eps', mode='eps', enhanced='1',
140           fontsize='24')

```

B.4 A glimpse under the hood

Up to here only the user's side was shown. Now a short discussion is given how the work is done under the hoods. All objects implement the “`__call__`” method. This method expects exactly one parameter (except for the magnet module): An array of time values. The object acquires all other necessary information by evaluating the objects which were registered to it. (The “Angularencoder” and the “Readout” object implement a method which uses angular values to calculate the output. The “Angularencoder” implements a “GetTime” method to search the value in time corresponding to the angular value.) All objects must behave deterministically during one run because

- the integrator uses an advanced multi step method and evaluates its integrand at arbitrary points and
- the devices simulating the mechanics are typically evaluated twice, first for searching the time at which a certain angle was reached, and for calculating the signal of the electronics.

Listing B.1: The “`__call__`” method of the sector class

```

1  harmonics from the Magnet. Read the angle from the Turner. Calculate
   the
2  speed of the coil in that frame. Calculate the harmonics based on the
3  induction principle
4
5  Returns the voltage.
6
7  """
8
9  zpos = self._Calculatezpos(time) time, harmonics = self.Magnet(time,
   zpos)
10 time1, speed = self.GetSpeed(time) time1, angle = self.Turner(time)

```

```

11
12 harmonics = self._RecalculateHarmonics(time , angle , speed , harmonics)
13 Sensitivity = self._RecalculateSensitivity(time , angle , speed ,
14 self.Sensitivity)
15
16 return self._CalculateVoltage(time , angle , speed , harmonics ,
    Sensitivity)

```

For each component one module exists, in which the different implementations are gathered, e.g. the “Angularencoeder” module offers an ideal and a real implementation. As aforementioned, an ideal and a real implementation exist for all components. The real implementation can yield the same results as the ideal one by using appropriate input parameters as setting all mark deviations of the angular encoder to 0, the ideal implementation however is added for convenience. To calculate its output, the object needs information about its input. I will explain it by means of the sector (See also Listing B.1). When python executes “sector(time1)”, it evaluates the “__call__” method of the sector. In this method the sector first evaluates its z-position. The magnet is evaluated to get the harmonics. The angle is evaluated by calling the turner object (typically a motor or a shaft). With this information, it can calculate the output voltage of the sector versus the time.

B.4.1 The sector and coil classes

The main part of this code focuses on the coils and the sectors (coil arrays). These are the main devices in the setup. The coil class just wraps the sensitivity. The sector class handles the communication with the attached devices to calculate the voltage induced in its coils. Further the real implementation of the sector class allows to simulate transversal vibrations or it can calculate the voltage induced in the coils in a time varying field. If one executes the following code:

```

coil_a = Sector.GenericCoil.GenericCoil()
coil_a.Setsensitivity( grail)
coil_c = Sector.GenericCoil.GenericCoil()
coil_c.Setsensitivity( coconut)
sector = Sector.GenericSector.GenericSector(( coil_a , coil_c))

```

the sector will add the sensitivity of the coils during initialisation. To set different gains the compensator object can be used:

```

coil_a = Sector.GenericCoil.GenericCoil()
coil_a.SetSensitivity(grail)
coil_c = Sector.GenericCoil.GenericCoil()
coil_c.SetSensitivity(coconut)
sector_a = Sector.GenericSector.GenericSector((coil_a,))
sector_c = Sector.GenericSector.GenericSector((coil_c,))
compensator = Compensator.IdealCompensator()
compensator.SetChannel(self, 'A',
                       Compensator.IdealChannel(sector_a, 1))
compensator.SetChannel(self, 'B',
                       Compensator.IdealChannel(sector_c, -1))

```

The evaluation distinguishes between the two approaches. The first adds the sensitivities to one new sensitivity and forms one sector, which then calculates with one sensitivity. The second approach uses different sectors, which are evaluated separately and their output is added afterwards. The first approach is faster, but the second approach allows to simulate more effects: e.g. movement of the different coils against each other, by linking different motion objects to sector_a and sector_c.

B.5 Calculating the sensitivity

It was shown in Section B, that one must register the readout object to the harmonic analysis. In Figure B.1 one can see that the whole electronic channel changes the coil's signal. In the analysis these changes have to be taken into account. For that purpose all the electronic equipment objects provide the "GetSensitivity" method. Each electronic device requests this information from its input and changes the sensitivity according to its own behaviour: e.g. a preamplifier with gain 10 will multiply the sensitivities with 10. When the harmonic analysis needs to scale the flux, it uses the "GetSensitivity" method of the "Readout" object to get the sensitivity of the coil "scaled" to the used electronics.

B.6 Calculating the differential

The derivative of the term $\{ \}$ of Equation (B.1) is calculated using analytical formulae. All classes of the magnet, power supply, motor and shaft implement meth-

ods which calculate the derivative of the function of the “`__call__`” method. Sometimes more than one object needs to compute derivatives in the calculation: e.g. a shaft object needs the motor derivative and the motor function to calculate its own derivative. In this case the object applies the function derivative formula. As many artefacts are described using a “Fourierseries” instance, this object implements an “eval” method for the normal function, and a “diff” method for its derivative.

Conclusion

A short tutorial how to use the tool called Truffaldino was given here. The user has to set up the system to his needs. Then only one object has to be called to give the result of the measurement system. In the last section a short glance was given, how the tool works inside. New effects can be added by deriving from the ideal implementation of the according device.

Appendix C

Axis calculation procedures

C.1 A procedure to calculate the rst values.

The rst values are needed by the MAD program to assist the survey group aligning the magnetic elements of an accelerator. Each magnet has reference points called fiducials. As input the MAD program needs to know the location of the fiducials in the RST frame.

The rst frame defines the position of the fiducials to the magnetic properties: the centre of the field and the direction of the field. For the LHC the rst coordinate system has been defined by the Alignment Working Group [64] in the following way (See also figure C.1):

1. The origin of the coordinate system is the middle between the two magnetic centres.
2. Two lines are drawn at $r = -apd/2.0, t = 0, s = 0$ and $r = +apd/2.0, t = 0, s = 0$. $apd = 194\text{ mm}$ is the distance between the apertures. These lines describe the ideal axes of the quadrupole.
3. The coordinate system is turned to minimise the distance between the data points and the axis describing the aperture for the data points d_i :

$$\sum_i |\vec{d}_i - ap(\vec{d}_i)| \equiv \min \quad (\text{C.1})$$

with $ap()$ the function describing the two ideal apertures. It is given as:

$$\begin{aligned} -\frac{apd}{2} \cdot \vec{r} + (\vec{d}_i \cdot \vec{s}) \vec{s} & \quad \vec{d}_i \cdot \vec{r} < 0 \\ +\frac{apd}{2} \cdot \vec{r} + (\vec{d}_i \cdot \vec{s}) \vec{s} & \quad \vec{d}_i \cdot \vec{r} > 0 \end{aligned} \quad (\text{C.2})$$

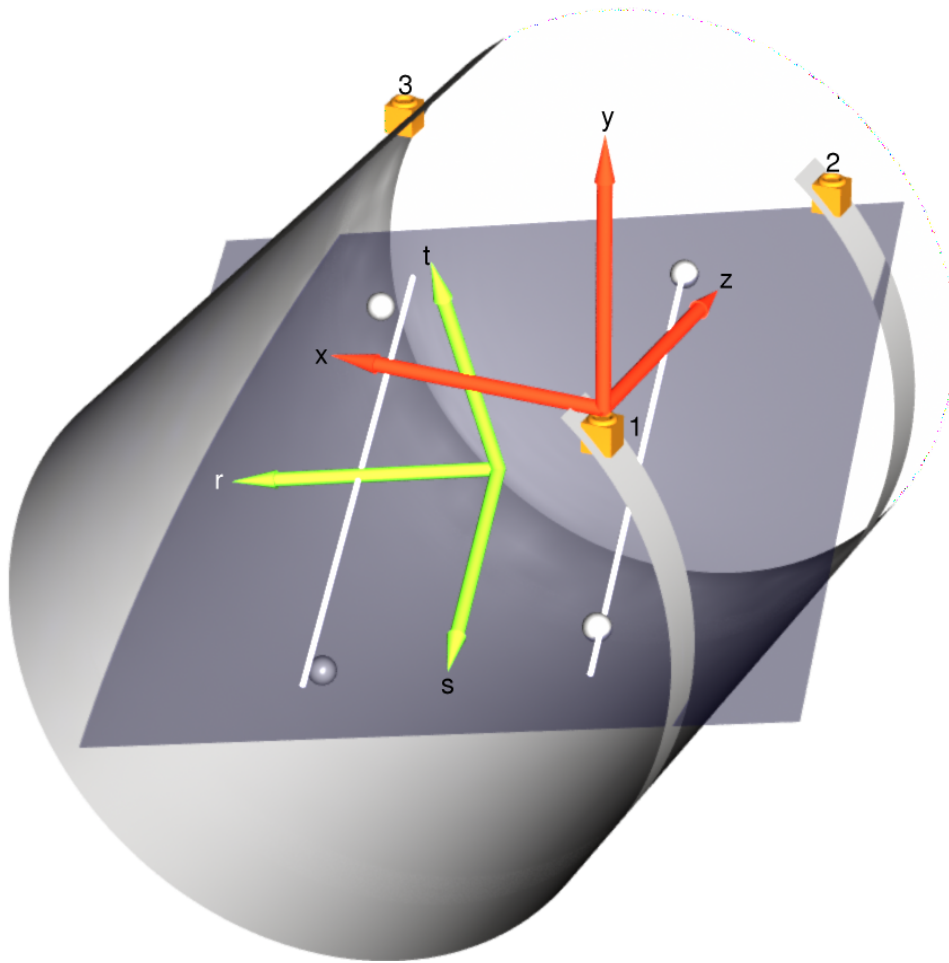


Figure C.1: An illustration of the survey and the rst coordinate systems. The red one is the survey system used for measuring the SSS and the reference points (quadrupoles.) The green one represents the rst system. The spheres represent the data points and the lines the ideal quadrupole axes.

The SSS's survey coordinate system is defined by:

1. The centre of the coordinate system is the fiducial 1.
2. The y coordinate is parallel to gravity.
3. The z coordinate points to the projection of the fiducial 2 on the plane $y = 0$.
4. The x coordinate is chosen so that the whole system forms a x, y, z right hand coordinate system.

The calculation of the rst system fits the simplified magnet model to the measured data. The procedure is:

1. The points are calculated in the survey reference frame. This has its origin in one of the fiducials. Its x - axis points towards the second fiducial normal to the cryostat axis. Its z axis points towards the last fiducial. The y axis is chosen, so that the system forms a right handed $x y z$ frame.
2. The new coordinate system is shifted (in r and t) and turned around all angles to minimise the distance between the measured points and the ideal axes.
3. The same translation and rotation is also performed with the fiducials data.
4. The magnetic centre of both quadrupoles are calculated in s . The mean value is then taken as the start of the s coordinate.

Appendix D

Symbols and Abbreviations

D.1 Used Symbols

F_L	...	Lorentz force
e	...	electric charge
E, \mathbf{E}	...	electrical field
B, \mathbf{B}	...	magnetic field
Φ	...	magnetic flux
Ψ	...	flux spectrum
v	...	speed
ω	...	rotation speed
θ	...	angular position of the magnetic probe
C_n	...	n^{th} multipole of the magnet
K_n	...	Sensitivity of the magnetic probe to the n^{th} multipole of the magnet
z	...	$= x + iy$ point in the complex plane
z_m	...	coordinate axis parallel to the magnet axis
z_1, z_2	...	positions of coil wires
R_c	...	distance between coil and rotation center of a tangential coil
N_w	...	number of windings of the coil
L	...	length of the coil
A_m	...	magnetic surface of a coil
R_{Ref}	...	reference radius. For LHC it is 17 mm.
δ	...	opening angle of the tangential coil

r, t, s	...	coordinate system used by the survey group and the MAD program
apd	...	The nominal distance between the apertures. It is 194 mm for the quadrupoles at operating condition (1.9 Kelvin)
i	...	$\sqrt{-1}$
b	...	bucking factor
ϕ	...	phase of a multipole
α	...	angle of the field
	...	

D.2 Abbreviations

MQ	...	Main Quadrupole
SSS	...	Short Straight Section